Compressed air energy storage in porous geological formations

–

Investigation of storage characteristics and induced impacts

Dissertation
in fulfilment of the requirements for the degree “Dr. rer. nat.”
of the Faculty of Mathematics and Natural Sciences
at Kiel University

submitted by
Bo Wang
Kiel, November 2018

First referee:	Prof. Dr. rer. nat. Sebastian Bauer
Second referee:	Prof. Dr.-Ing. Olaf Kolditz
Date of the oral examination:	01.03.2019
Approval for printing:	01.03.2019

gez. Prof. Dr. Frank Kempken, Dekan

AFFIDAVIT

Here I declare that apart from the supervisor's guidance the content and design of the thesis is all my own work. Furthermore, the thesis has not been submitted either partially or wholly as part of a doctoral degree to another examining body and it has not been published or submitted for publication. Moreover, the thesis has been prepared subject to the Rules of Good Scientific Practice of the German Research Foundation. At last, no academic degree based on this thesis has been revoked.

Kiel, 11.2018 Bo Wang

Abstract

With the rapid growth of energy production from intermittent renewable sources like wind and solar power plants, large-scale energy storage options are required to compensate for fluctuating power generation on different time scales. Compressed air energy storage (CAES) in porous geological formations is seen as a promising underground storage option for balancing short-term diurnal fluctuations. CAES is a power-to-power energy storage, which converts electricity to mechanical energy, i.e. highly pressurized air, and stores it in the subsurface. This thesis aims at investigating the feasibility, dimensioning the storage capacity, and assessing the induced hydraulic, thermal and geochemical impacts of a large-scale CAES operation in porous formations. For this, scenario based numerical simulations are used.

A realistic and representative CAES scenario using a typical anticline structure from the North German Basin is developed. The top of the storage formation is assumed to be at 700 m depth, and the porosity and permeability are assumed to have a homogenous distribution with a value of 0.35 and 500 mD, respectively. The chosen mineral assemblage is consistent with the typical Rhaetian sandstones and shows the presence of pyrite. In accordance with the specifications of the Huntorf CAES power plant, a gas turbine producing 321 MW power with a minimum inlet pressure of 43 bars at an air mass flowrate of 417 kg/s is assumed. Pressure loss within the gas wells is accounted for using an analytical solution, which results in a minimum bottom hole pressure of 47 bars. Two daily extraction cycles of 6 hours each are set to the early morning and the late afternoon in order to store and shift potential solar energy production around noon to the morning and evening.

Using twelve vertical wells the storage formation can provide a continuous power output of 312 MW for 6 hours, which corresponds to an energy output of 3852 MWh per day. At the design capacity, this power supply can be sustained for a maximum of 9.6 hours without any additional air refill. For the first 30 minutes, maximum power output is higher at 484 MW. A sensitivity analysis shows that the number of wells required does not linearly decrease with increasing permeability of the storage formation due to well inference. For low-permeability reservoirs, using horizontal wells can increase the storage capacity and the storage rates of this CAES facility.

In the storage formation, the initial filling results in a maximum pressure build-up of about 31 bar near the storage wells and 3 bar at a distance of 10 km throughout the storage formation. During the cyclic storage operation, pressure fluctuations of more than one bar can only be observed within the gas phase. Assuming the injected air temperature being close to the average reservoir temperature, the induced temperature increase by air injection is found to be minimal at 5.3 °C very close to the wells. During the cyclic operation, a cumulative decrease in temperature is observed due to the Joule-Thomson effect with a maximal temperature decrease of about 5.8 °C at roughly 25 m from the storage wells.

The injection of air into this geological formation leads to pyrite oxidation, changes in stored air composition, air pressure and formation properties. Only a very small change up to 0.29 % in the oxygen mole fraction is found within one storage cycle, which does not affect flammability of the gas mixture of natural gas with the stored air. Considering a longer residence time, the oxygen concentration in the stored air may drop below the minimum oxygen concentration for flame propagation and thus cannot be used for burning natural gas as required for a diabatic CAES. The pH of the formation fluid can drop significantly below one near the gas wells increasing the risk of well corrosion. Mineral dissolution and precipitation in the storage formation results only in minor increases of porosity and permeability with relative changes of up to 5.0 %. The uncertainties in mineral reactive surface area and pyrite oxidation kinetic strongly affect the rate of oxygen reduction and fluid acidification. Analysis of these parameters at the target location, especially for pyrite, are therefore required for a reliable estimate of possible induced geochemical reactions and impacts.

Investigating CAES operation in porous formations requires static geological models representing complex geological systems and dynamic models for the assessment of occurring subsurface processes. In this thesis a workflow for converting heterogeneous geological models to consistent finite element models is developed. The individual degeneration situation of regular and irregular hexahedral blocks in a corner point grid is accounted for by converting to a set of hexahedra, prism, pyramid and tetrahedral elements. Heterogeneous geological data such as permeability or porosity can be transferred. Additionally, well trajectories can be accurately mapped to the converted Finite Element mesh, to place the corresponding source terms.

Kurzfassung

Im Zuge des rasanten Ausbaus der Energieproduktion aus erneuerbaren aber fluktuierenden Quellen wie Wind und Solarenergie, werden Energiespeicheroptionen als Puffer in großem Umfang und für verschiedene Zeitskalen benötigt. Druckluftspeicher (CAES - *compressed air energy storage*) in porösen geologischen Formationen stellen eine aussichtsreiche untertägige Speicheroption zur Überbrückung kurzfristiger, täglicher Fluktuationen dar. CAES ist ein *power-to-power* Energiespeicher, der elektrische in mechanische Energie, d.h. Druckluft, umwandelt und im Untergrund speichert. Ziel dieser Doktorarbeit ist die Untersuchung der Realisierbarkeit, die Dimensionierung von Speicherkapazitäten und die Bewertung der induzierten hydraulischen, thermischen und geochemischen Auswirkungen eines großskaligen CAES-Betriebs in porösen Formationen mit Hilfe von szenariobasierten numerischen Simulationen.

Das hier entwickelte realistische und repräsentative CAES-Szenario verwendet eine typische Antiklinal-struktur des Norddeutschen Beckens als Fallenstruktur für die Druckluftspeicherung, als Speicherformation dienen die Sandsteine des Rhäts. Die Oberkante der Speicherformation befindet sich in 700 m Tiefe. Porosität und Permeabilität betragen 0,35 bzw. 500 mD und werden als homogen verteilt angenommen. In der Mineralzusammensetzung der Rhätsandsteine befindet sich Pyrit. Entsprechend der Spezifikationen des Huntorf CAES-Kraftwerks wird die Ausspeicherleistung mit 321 MW angenommen, wobei ein minimaler Turbineneingangsdruck von 43 bar bei einem Luftmassenstrom von 417 kg/s notwendig ist. Der Druckverlust entlang des Bohrloches wird mit Hilfe einer analytischen Lösung berücksichtigt, woraus sich ein minimaler Bohrlochdruck von 47 bar ergibt. Der Speicherbetrieb besteht aus zwei Extraktionszyklen von je 6 Stunden jeweils am Morgen und am Abend, um potentziale Solarenergieproduktion während der Mittagszeit zeitlich zu verschieben.

Bei der Verwendung von zwölf Brunnen ist die Speicherformation in der Lage eine Leistung von 321 MW über einen Zeitraum von 6 Stunden kontinuierlich zu erbringen, was einer ausgespeicherte Energiemenge von 3852 MWh pro Tag entspricht. Maximal kann das CAES-Kraftwerk diese Leistung über einen Zeitraum von bis zu 9,6 Stunden ohne erneute Druckluftzufuhr aufrechterhalten. Während der ersten 30 Minuten ist kann eine maximale Leistung von bis zu 484 MW abgerufen werden. Die Anzahl der für diesen Speicherbetrieb benötigten Brunnen steigt aufgrund gegenseitiger Druckbeeinflussung nicht linear in Abhängigkeit von geringeren Speicherpermeabilitäten. In gering permeablen Reservoiren kann die Verwendung horizontaler Brunnen die Speicherkapazität sowie die kurzfristig erreichbare Leistung dieses CAES-Systems erhöhen.

Die durch die initiale Gasinjektion induzierte Druckerhöhung betragen im direkten Umfeld der Speicherbrunnen 31 bar und rund 3 bar in 10 km Abstand, d.h. in der ganzen Speicherformation. Während des zyklischen Betriebs treten Druckschwankungen von mehr als 1 bar nur innerhalb der Gasphase auf. Unter der Annahme, dass die Temperatur der injizierten Druckluft annähernd der Reservoirtemperatur entspricht, ist die Temperaturerhöhung durch Druckluftinjektion mit 5,3 °C in Brunnennähe gering. Während des zyklischen Speicherbetriebs wird eine kumulative Temperaturabnahme aufgrund des Joule-Thomson-Effekts beobachtet, welche maximal 5,8 °C in einem Abstand von etwa 25 m von den Brunnen beträgt.

Die Injektion von Luft in eine geologische Formation führt zur Pyritoxidation, Veränderungen in der Luft-zusammensetzung, Luftdruck, und Speicherformationseigenschaften. Der Stoffmengengehalt von Sauerstoff verändert sich während eines Speicherzyklus nur sehr geringfügig um bis zu 0,29 %, was keine Auswirkung auf die Entflammbarkeit des Erdgas-Druckluftgemisches im Kraftwerk hat. Im Falle von längeren Verweilzeit kann die Sauerstoffkonzentration jedoch unterhalb der Mindestkonzentration zur Entflammbarkeit fallen und daher nicht für die Verbrennung von Gas verwendet werden. Der pH-Wert der Formations-wässer kann in Brunnennähe unter 1 fallen und somit das Korrosionsrisiko der technischen Anlagen erhöhen. Die Lösung und Ausfällung von Mineralen in der Speicherformation führt nur zu geringen Porositäts- und Permeabilitätserhöhungen von maximal 5,0 %. Die Unsicherheiten in der Bestimmung der reaktiven Oberfläche von Mineralen und der Pyritoxidations-kinetik beeinflussen die Rate der Sauerstoffoxidation und die Fluidsäuerung in hohem Maße. Für eine zuverlässige Abschätzung möglicher induzierter geochemischer Reaktionen und Auswirkungen ist aus diesem Grund eine Analyse dieser Reservoirmineralphasen-parameter aus der Zielformation, insbesondere für Pyrit, erforderlich.

Die Untersuchung von CAES-Systemen in porösen Formationen erfordert statische geologische Modelle für die Darstellung komplexer geologischer Systeme, sowie dynamische Modelle für die Beurteilung der Prozesse im Untergrund. In dieser Doktorarbeit wird ein Workflow für die Konvertierung heterogener geologischer Modelle in konsistente Finite-Elemente-Modelle entwickelt. Reguläre und irreguläre Hexaeder eines *corner point grids* werden entsprechend der individuellen Degenerationssituation in Hexaeder, Prismen, Pyramiden und Tetraeder konvertiert. Heterogene geologische Daten, wie Permeabilität oder Porosität, können Schichten- oder Blockweise transferiert werden. Zusätzlich können Brunnenpfade präzise im konvertierten Finite-Elemente-Netz abgebildet werden.

Acknowledgements

I would like to take this opportunity to express my sincere gratitudes to all who helped me or supported me during my PhD research.

First of all, I want to thank my supervisor, Prof. Dr. Sebastian Bauer, for giving me the chance to come to Kiel and work in the field of underground energy storage. I also want to thank him for patiently guiding me through all the long and "painful" discussions and providing valuable insights for my research. What I am really grateful is his mentoring way of showing me how to think as a modeler when facing unknown factors in research. I will definitely benefit from that in my scientific career.

Secondly, I would like to thank all my colleges at Kiel University, especially Dr. Christof Beyer for his kind patience of helping me with all my stupid questions whenever I show up at his office. I also want to thank Dr. Wolf Tilmann Pfeiffer for his great support and all fruitful discussion during many coffee breaks. Besides, I want to thank Dr. Dedong Li and Dr. Jens-Olaf Delfs for offering me always fast and sufficient solutions to all technical problems. Furthermore, I would like to thank Dr. Markus Ebert and Dr. Márton Berta for their highly valuable scientific input to my research on geochemistry. Many thanks are also given to Dr. Alina Kabuth for her help in project coordination, to Steffi Popp, Katharina Benisch and Anke Boockmeyer for their helpful discussion, as wells as to Johannes Nordbeck, Janine Struß, and Kerstin Meier zu Beerentrup for all pleasant and relaxing lunch breaks.

At last, I would like to thank my parents who have supported me so many years during my studying although I am always far away from them in another country. I am genuinely grateful for my wife Yushu's company during these years in Germany. I couldn't have reached this far without her support, care, and understanding, especially during her pregnancy.

Contents

List of Figures

List of Tables

1 Introduction

1.1 Motivation

1.1.1 Energy transition and energy storage

Since 1950s, changes in the climate systems, such as the warming of the atmosphere and ocean, the diminishing of the snow and ice, and the rising of the sea level have been observed. The largest contribution to these changes is found to be the increase of the CO_2 concentration in the atmosphere (Stocker 2014). To fight global climate change by means of reducing CO_2 emission, the transition of the energy supply from carbon rich fossil fuels to renewable energy sources is pursued by many countries in the world (IPCC 2014). For example, in Germany the "Energiewende" is targeting a 100 % share of renewables in energy supply by 2050 (UBA 2010). In the European Union (EU), the final target of 20 % in renewable sources is very promising to be accomplished by 2020 (European Commission 2015). In China, the 13th Five-Year-Plan of renewable energy development aims to reach a 15 % share by 2020 and 20 % in 2030 (China's National Development and Reform Commission 2016).

Electric power generation by wind or solar power plants are major energy sources in renewable energy production. Using such renewable sources in energy production can reduce the CO_2 emission, but can result in challenges in power generation because of strong diurnal or seasonal fluctuations of wind and solar power due to changing weather conditions. Improvements of cross-border grid connectivity, electrical demand-side management and grid-scale energy storage systems are possible solutions to compensate the induced offsets between demand and supply by these fluctuations (Sterner and Stadler 2014). However, improving the current cross-border grid connectivity in Germany means a large amount of construction work and high associated costs since the existing power transmission lines are insufficient (Bundesnetzagentur 2015; MELUR 2015). Even with enough power transmission lines, managing fluctuating renewable energy production to match instantaneous energy demand at different time scales can be very difficult (Weiß and Schulz 2013), or impossible for an extreme condition of insufficient wind and solar energy production in the whole of Europe. Grid-scale stand-by storage systems, instead, can offer large potential storage capacities, high achievable input and output rates, and they are much more flexible in terms of different time scales varying from less than hourly over daily up to seasonally. The larger the share of renewable energy sources in energy production is, the more energy storage systems are required to allow for a stable and flexible power grid (Morris and Pehnt 2016). For example, an annual energy storage demand of up to 50 TWh is estimated for Germany (Bräutigam et al. 2017) and 600 GWh for Denmark assuming

a 80 % renewable energy share (Sorknæs et al. 2013).

Common large-scale energy storage systems used in electric grids can be categorized as Power-to-Power storage, such as pumped hydroelectric energy storage (PHES) and compressed air energy storage (CAES), Power-to-Heat storage, such as aquifer thermal energy storage, and Power-to-Gas storages, such as synthetic methane and hydrogen storages (Sternberg and Bardow 2015). PHES is one of the above-ground storage options using water reservoirs and provides a high storage capacity worldwide. However, the expansion potential of PHES is limited by the number of suitable geographic sites at the surface (Budt et al. 2016). Alternatively, the geological subsurface can be used for large-scale energy storage systems to compensate the fluctuations in energy production by intermittent renewable energy sources, and even for different time scales varying from daily, weekly to seasonally (Bauer et al. 2013). Subsurface storage options include underground storage of natural gas (Buschbach and Bond 1974), underground storage of hydrogen (Carden and Paterson 1979), underground CAES (ANR Storage Company 1990) or subsurface storage of heat (Ball et al. 1983; Molz et al. 1983).

1.1.2 Underground compressed air energy storage

Compressed air energy storage (CAES) in the geological subsurface is a Power-to-Power energy storage option (Sternberg and Bardow 2015). CAES converts electricity to mechanical energy and stores it in the form of pressurized air. A schematic sketch of a hypothetical CAES facility is shown in Fig. 1.1. It consists of a surface turbomachinery, air injection and extraction wells, and an underground anticline storing air. When there is surplus power available in the electric grid during off-peak times, the motor (see ② in Fig. 1.1) in the turbomachinery drives the compressor (see ① in Fig. 1.1) to convert electricity to highly pressurized air, which is afterwards transported into the storage reservoir through pipelines and gas wells. During times of peak electricity demand, the stored pressurized air is retrieved from the storage reservoir and expanded in the gas turbine (see ③ in Fig. 1.1), driving the generator (see ② in Fig. 1.1) to produce electric power.

The CAES facility shown in Fig.1.1 is one example of a diabatic type because the heat resulting from air compression is not stored in any form but dissipates through intercoolers between compressors. During discharging, the air expands and cools. An external heat source is required therefore during discharging, so that the condensation in and icing of the expanders can be prevented. For this, natural gas is typically burned with the compressed air in the combustion chamber of the gas turbine resulting in the hot exhaust gases being expanded (Budt et al. 2016). A recuperator can be installed to preheat the compressed air entering the combustion chamber using the heat from turbine exhaust gases, which can enhance the round-trip efficiency (Luo et al. 2014). In comparison, in an adiabatic setup the heat from the compression of the air is stored in a thermal energy storage system and later used to heat up the discharging air before entering expanders (Hartmann et al. 2012; Luo et al. 2016).

The application of CAES in the geological subsurface has started in 1970s

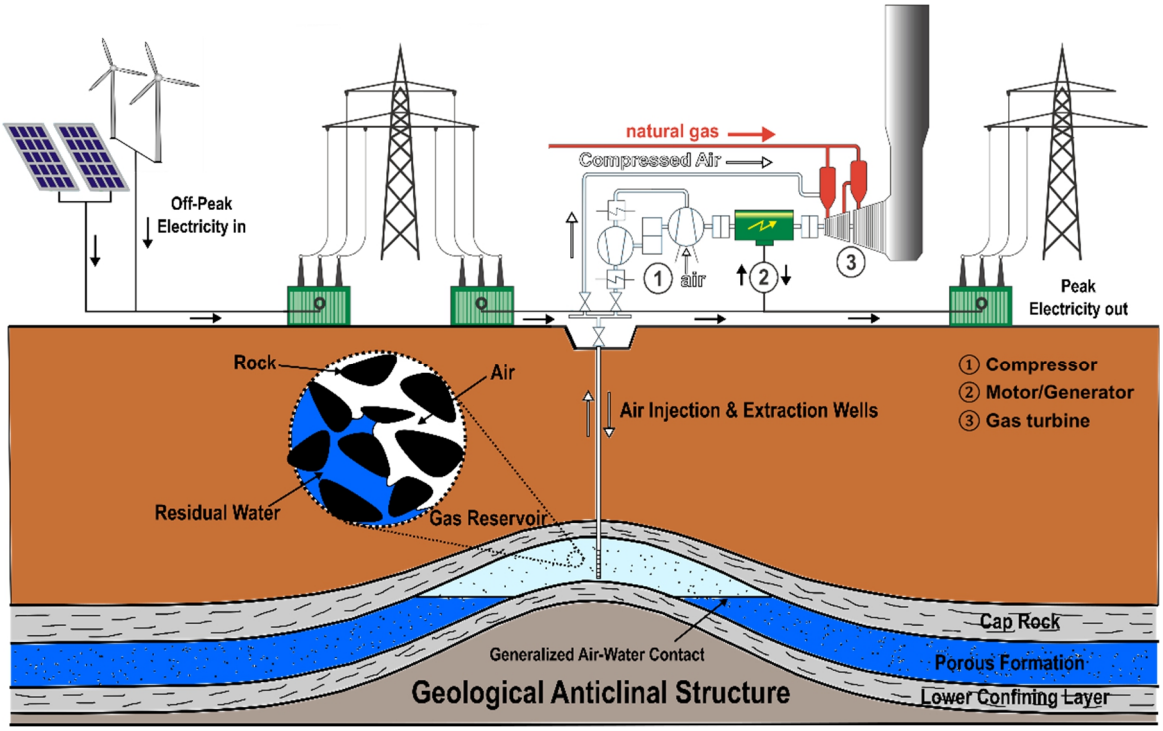

Figure 1.1 A schematic sketch of a hypothetical diabatic CAES facility using a porous formation as the storage reservoir (modified from (Crotogino et al. 2001)).

resulting in the construction of two CAES facilities, Huntorf in Germany and McIntosh in the US. Currently, only these two power plants are in operation worldwide with both being of the diabatic type. The purpose of building the Huntorf power plant was to transfer off-peak energy produced by nuclear or coal fired power plants to the high demand periods, and to stabilize the electric grid when some of these plants have failures during operation. This designed double-duty is possible because CAES power plants are able to ramp up quickly between load levels within a few minutes and operate effectively at partial loads. This is also why CAES power plants nowadays draw attention again for balancing short-term diurnal fluctuations in energy production in electric grids with a high share of renewable energy sources. Shifting the overproduced off-peak energy from renewables to be used during peak demands on a daily basis can also make CAES power plants to be operated as base load power plants (Succar and Williams 2008).

Typical geological formations for underground CAES are salt caverns and porous formations. Salt caverns are created by solution mining within suitable salt domes as an artificial void compartment. The two currently operating CAES facilities, Huntorf and McIntosh, both are using salt caverns for storing the compressed air. Using salt caverns for storing compressed air allows for a very high deliverability since there is no inherent limitation originating from the rock salt formation unlike the hydraulic permeability in porous formations (Kushnir et al. 2012b). However, the availability of suitable rock salt formations in the world is very limited. In Europe only in the northern parts and in the US only in the southern coastal areas suitable salt formations are available (Succar and Williams 2008). Compared to salt caverns, geological porous formations have a wider range of geological availability

in the world for gas storages (Evans and Chadwick 2009; LBEG 2015). These porous formations can be found at different depths allowing for different operational pressures and also provide much larger storage capacities, e.g. from millions of cubic meters to hundreds of millions of cubic meters in Germany (IGU/WOC 2006). Available geological porous formations for CAES are depleted gas reservoirs and saline aquifers, given they are highly permeable for achieving sufficient gas flow rates and have tight cap rocks at the top to prevent buoyant rise of the stored air. Besides, structural traps for the injected air, such as anticlines (see in Fig. 1.1) or impermeable faults should be present to ensure the air to remain near the storage wells. Furthermore, a suitable porous formation needs to be deep enough to store air at high pressure.

Since geological porous formations are more frequently available in the world compared to salt caverns, using porous formations for CAES therefore has become a very promising option. The concept of CAES in porous formations has been studied in the 1980s through an experimental field site in Pittsfield, Illinois, USA (ANR Storage Company 1990). This field experiment demonstrated that, for the given site cyclic air storage operations were feasible. The observed airflow deliverability and storage pressure responses were predictable using techniques developed for natural gas storage sites. Another attempt of a large-scale field application is the Iowa Stored Energy Park project with a power rating of 270 MW. However, this project was stopped due to geological limitations (Schulte et al. 2012), as unexpected low permeabilities in the storage formation caused an insufficient air extraction rate and thus the target power output could not be achieved. Therefore, a feasibility study of the storage operation in terms of reservoir behavior, e.g. airflow deliverability and storage pressure responses, is required for any potential field sites. Referring to the uncertainty in reservoir properties, a dimensioning of storage capacity, such as possible deliverable rates and their duration, is helpful for planning large-scale CAES applications in porous formations.

1.1.3 Processes and induced impacts

Saline aquifers in the deep subsurface are one of the suitable geological porous formations for CAES. Since the pore space in the storage formation is initially saturated with saline water, an initial air injection is required to create a gas reservoir and allow a cyclic storage operation. Injecting air into the water saturated storage formation will result in water displacement away from the wells towards the formation boundaries, which is a multiphase flow process. Since air and water are two non-miscible phases with large differences in density and viscosity, the injected air initially forms fingering patterns and eventually becomes a coalesced gas bubble, i.e. thus a developed gas reservoir. An irreducible water saturation, i.e. residual water, persists due to capillary and hysteresis effects. In the developed gas reservoir during CAES operation, therefore, a multiphase-multicomponent system is established consisting of a gas phase, i.e. stored air, a liquid phase, i.e. residual formation water, and the solid phase, i.e. the rock (see Fig. 1.1).

Operating CAES in a porous formation having such a multiphase-multicomponent

system is governed by thermal (T), hydraulic (H), geomechanical (M) and geochemical (C) processes and also induces secondary impacts (Bauer et al. 2013, 2015). Since the geomechanical process is beyond the scope of this thesis, a short overview of THC processes and their secondary impacts is given as follows.

Hydraulic process and impact

CAES is comparable to natural gas storage or carbon dioxide capture and storage, which are well studied for their hydraulic processes, partially based on decades of experience in the oil and gas industry. During the initial fill with air, the pressure of the injected air needs to be higher than the pressure in the storage formation allowing for the displacement of water. This can thus lead to pressure build-up in gas wells and the storage formation. Over time, the elevated pressure propagates away from gas wells towards the formation boundaries resulting in a pressure increase throughout the whole storage formation. The described hydraulic processes happening during the initial fill are similar to those in CO_2 storage (e.g. see Leetaru et al. (2009), Zhou and Birkholzer (2011)) and natural gas storage (e.g. see Tek (2012)). The pressure build-up to be expected during such gas injections is proportional to the injected air flow rate, and highest at gas wells but dampened in the storage formation away from gas wells (Benisch and Bauer 2013; Cihan et al. 2013; Baghooee et al. 2014).

During the storage operation, the compressed air is cycled within the developed gas reservoir. The air injection can lead to the compression of air in the storage reservoir resulting in further pressure build-up, but the extraction of air causes expansion resulting in pressure decrease. Since CAES is considered for balancing short diurnal fluctuations in energy production, the cyclic amount of air can be much smaller compared to the air in the storage reservoir injected by initial fill. Because of this, the induced pressure responses during cyclic operation is found to be within the gas reservoir by Oldenburg and Pan (2013a), who investigated a diabatic CAES using a single well to produce half of the power as the Huntorf power plant. Considering CAES in porous formations for large storage capacities, e.g. producing the same or even larger power than the Huntorf site, multiple wells are required. A stronger pressure response at gas wells and in the storage formation may be expected during cyclic operation due to the effects of well interference.

Thermal process and impact

Along with the induced pressure responses, the injected air may have a different temperature compared to the temperature in the storage formation and thus induce temperature changes due to the propagation of thermal fronts by advection (Oldenburg and Pruess 1999). The operational experiences of Huntorf power plant (Hoffeins 1994) showed that the air temperature after the compressor was actually cooled down close to the average temperature of the salt cavern. If the same assumption is made for CAES in porous formations, the induced thermal impacts due to the injection temperature will be minor. This is shown in the studies by Oldenburg and Pan (2013a) and Guo et al. (2016), who found that the induced temperature change in the storage formation is only a few Kelvin, and spatially limited to regions in and very near to the well.

However, in these studies, the air is assumed to be ideal gas and thus the Joule-Thomson effect is not considered. The Joule-Thomson effect, or the Joule-Thomson process, quantifies the temperature change of real gas due to the change in pressure driving flow assuming that no heat is exchanged with the environment (Joule and Thomson 1854). During a CAES operation, the injected air expands and flows from a high pressure region, i.e. near the gas wells, towards a low pressure region such as the edge of the reservoir. During the air extraction, the stored air is also expanded but in an opposite direction, e.g. with the gas flowing from the reservoir edge towards the gas wells. Both expansion processes are driven by pressure changes, which are pressure decreases along flow directions. Since the Joule-Thomson coefficient of air is positive, a decrease of air pressure results in a decrease of air temperature, which can also lead to a decrease in the recovered energy, because for a diabatic CAES more natural gas is needed to heat up the extracted air with a lower temperature.

Geochemical process and impact

The geochemical process and induced secondary impacts by a CAES operation in a geological porous formation may differ significantly from other gas storages, because oxygen in air is introduced into the geological formation, which is long-free of oxygen and may have a redox-sensitive environment. Therefore, oxidation reactions can be induced, which have been observed in carbon dioxide storage considering oxygen as an impurity (Jung et al. 2013; Wei et al. 2015; André et al. 2015; Pearce et al. 2016a, b). However, this is not quantitatively assessed for large-scale CAES operations, in which oxygen is no longer an impurity but one of the major components.

Once the air is injected into the storage formation during the initial fill, gas components in air start to dissolve in the formation water. The dissolved components will react with the chemical species in the formation water from mineral dissolution. If redox-sensitive or ferrous-containing minerals such as pyrite (FeS_2, iron disulfide) are present, oxidation processes will be induced in the formation water due to the dissolved oxygen. With the ongoing chemical reactions, oxygen is constantly dissolved, reacts and can be depleted, which has been observed in the Pittsfield test (ANR Storage Company 1990). Without a refill of the storage reservoir with air, the low fraction of oxygen in the stored air may potentially cause an operational failure of a diabatic CAES facility as a minimum concentration of O_2 is required for the gas combustion process. The induced geochemical reactions also break the equilibrium between the formation water and the reservoir rock resulting in mineral dissolution and precipitation. This may clog the pore space, which can potentially reduce porosity and permeability of the storage formation, lowering well deliverability and thus power output (Pei et al. 2015). Besides, studies on acid mine drainage indicate that pyrite oxidation with ongoing supply of oxygen, e.g. near gas wells during CAES operation, can lower the pH to very acidic conditions (INAP 2012; Nordstrom et al. 2015), which increases the risk of wellbore corrosion.

For CAES in porous formations, individual processes and impacts highly depend on the specific usage scenario. The dimensions and magnitudes in space and time can only be assessed in a scenario-specific way. This

requires the definition of target air flow rates and injection temperature as well as site or location specific properties, such as permeability, porosity and mineral compositions. Since the storage operation can be affected by the induced impacts, e.g. the stored energy can be lowered by induced geochemical reactions due to the consumption of oxygen in the stored air, a reliable quantification of induced secondary impacts is required when the feasibility of CAES in porous formations is discussed. This is also required for the risk assessment in terms of the environmental impacts on protected entities, e.g. the study of pressure responses in the storage formation is useful to identify the potential risks of brine uprising by pressure build-up (Oldenburg and Rinaldi 2011) or the possible leakage paths for gas uprising (al Hagrey et al. 2016). Last but not least, suitable porous formation for CAES can be also used for other underground usages, such as brine disposal and deep geothermal exploration. To plan this competitive usage of the same porous formation, the study of induced impacts is necessary because it helps to delineate the affected space of a single usage and account for mutual impacts of different usages (Kabuth et al. 2017).

1.1.4 Methods and tools

Multiphase flow processes in porous media, such as those occurring during CAES in porous formations, have been well investigated and predicted by mathematical formulations (Helmig 1997). Analytical solutions of these mathematical models also used in oil and gas industry (e.g. see Katz (1959)) may be applied to quantify the reservoir behaviors of CAES operation, e.g. pressure changes in gas wells and in storage reservoirs for a given air mass flow rate. However, since these analytical solutions are often derived for particular initial and boundary conditions, their applicability is strongly restricted and thus may not be sufficient for large-scale applications in real geological settings. Furthermore, the assessment of induced impacts relies on the specific usage scenario including storage operating parameters, geological site and governing processes, numerical models are therefore the only way to integrate and represent all these information, and thus make a quantitative analysis.

Numerical models in general consisting of two kinds of models, i.e. static models and dynamic models. Static geological models are used for correctly representing the geological nature of the studied storage formation and its environment in the subsurface, which is a prerequisite in order to achieve a reliable evaluation and assessment through numerical simulations. Dynamic models are used for representing the governing processes, simulating reservoir behaviors during storage operation and dimensioning of the individual operation as wells as for the assessment of induced impacts. To build static and dynamic models, a large amount of data is required to construct the geological model of storage site, parameterize these models and define initial and boundary conditions. Since these data highly depend on the specific usage scenario, the scenario development is an essential step when performing such numerical studies.

The available tools for building static and dynamic models, are numerical software based on benchmarked numerical codes. For static geological models, the petroleum industry has developed powerful geological reservoir modeling software, such as GOCAD (Paradigm 2016) or Petrel

(Schlumberger 2014). For dynamic models, to simulate reservoir behaviors of a CAES operation, reservoir simulators ECLIPSE (Schlumberger 2016) and GeM (Cheviakov 2007), or other multiphase flow simulators, such as TOUGH2 (Pruess 1991), DuMu^x (Flemisch et al. 2011) and OpenGeoSys (OGS) (Kolditz and Bauer 2004; Kolditz et al. 2012) can be applied. The software packages PHREEQC (Parkhurst and Appelo 2013) and ChemApp (Petersen and Hack 2007), besides other options, are available for setting up geochemical systems and quantifying chemical reactions.

For CAES operations, individual processes are generally coupled via parameters depending on the current state of the system, e.g. the concentration of dissolved air components in formation water depends on the current pressure in the storage reservoir. A reliable quantification of these processes and impacts thus requires numerical simulators to be able to solve the governing equations of these processes in a coupled manner. However, this is often not possible with one single simulator due to their specific limitations. Instead, different simulators need to be coupled together, especially for investigating geochemical processes. For example, reservoir simulator ECLIPSE is coupled with OGS, which is further coupled with PHREEQC, allowing for investigating induced geochemical reactions of a reservoir operation (Graupner et al. 2011; Pfeiffer et al. 2016b). The coupling between different numerical simulators may not be straightforward mainly due to different numerical algorithms applied (Benisch 2018), e.g. reservoir simulator ECLIPSE is on the basis of finite volume method, but OGS uses finite element method. This is not only the problem of coupling numerical tools for dynamic models, but also between static and dynamic models. For example, software like Petrel or GOCAD produces numerical grids based on finite volume methods and thus these grids cannot be used by finite element based simulators such as OGS. Due to the high complexity of these geological models in geometry and hydraulic connectivity, a workflow to make a consistent transfer between numerical tools including numerical grids and parameterized properties is necessary. Together with the available coupling scheme, this can allow for an investigation of induced secondary impacts by CAES operation in porous formations.

1.2 Objectives of this thesis

With the rapid growth of renewable energy sources in energy production, CAES is seen as a promising option to balance foreseeable diurnal fluctuations in electrical grids. Porous formations in the subsurface are considered as storage reservoirs for CAES operations because of their wide availability and large potential in storage capacity. However, to apply large-scale CAES in porous formations, investigations of the following relevant aspects are required.

The prerequisite of all investigations is the development of a suitable CAES operational scenario, which needs to be realistic and representative. The geological storage formation needs to be suitable for air trapping and also highly permeable for, in order to support the high required gas flow rates. The operational schedule should account for the possible occurrence and duration of energy overproduction and energy demand in electrical grids. Besides, the scenario development is also needed for defining boundary conditions in storage

operations, such as air flow rate and air pressure required at gas turbine inlet.

Based on the developed scenario, an investigation of reservoir behavior during the CAES operation is required as the first step in a feasibility study. The deliverability of the selected storage formation should be able to provide the required air mass flow rate while maintaining the minimum inlet pressure at the gas turbine in order to achieve the target power output. The pressure at the bottom hole of gas wells should be lower than the maximum safety pressure to prevent formation damages. Considering highly fluctuating energy demand in electrical grids, an analysis of other possible deliverable rates and times, i.e. storage capacity, should be also considered. Since the deliverability of a porous formation highly depends on the reservoir permeability and the number of gas wells used, the dimensioning of storage capacity and storage rate should be investigated for different reservoir permeabilities and well configurations.

Operating CAES in porous formations involves THMC processes, and also induces secondary impacts. A study of these induced impacts is necessary when discussing the feasibility of CAES because these impacts affect the storage operation as well. Furthermore, these induced impacts are potential risks to protected entities in subsurface, such as groundwater resources. A quantification of these impacts in space and time is thus required prior to any field applications providing information on the monitoring setup. Moreover, considering competitive uses of the storage formation, the study of induced impacts can help to delineate the affected space of CAES and allow for assessing potential mutual impacts from different usages.

Investigating the feasibility, dimensioning the storage capacity and assessing the induced impacts of CAES in porous formations require knowledge from different disciplines, such as geologic modeling, reservoir engineering and geochemical modeling. The working tools are available for individual disciplines based on different numerical schemes, and thus often needs to be coupled for interdisciplinary studies. To allow for that, approaches of consistently transferring models between different modeling tools, including numerical grids, parameters and source terms, are required.

In respect of the abovementioned aspects, the following objectives are going to be addressed in this thesis for a large-scale CAES operation in porous formations:

- Developing and quantifying a realistic and representative large-scale CAES operation scenario in terms of required storage rates, capacity and times using a typical porous formation as the storage reservoir.
- Assessing the feasibility of this large-scale CAES operation by quantifying the achievable storage rates and the storage capacity depending on the geological conditions and the required well configurations.
- Quantifying the induced thermal, hydraulic and geochemical impacts from this realistic CAES operation in space and time
- Development of adequate methods and a workflow to combine realistic static geological models of the subsurface with numerical dynamic process models for fluid flow and transport as a model basis for determining storage characterization and assessing induced impacts for real conditions.

1.3 Methodology and structure of this thesis

The feasibility of large-scale CAES operation in porous formation and the induced impacts can only be assessed based on a specific usage scenario including storage operation parameters and geological site. The usage scenario is also required for defining the numerical grid of geological site, parameters of storage operation and storage formation as well as initial and boundary conditions. Therefore, scenario based numerical simulations are applied in this thesis to study large-scale CAES operations in geological porous formations. A virtual synthetic anticline structure in the North German Basin is generated to be used as the storage reservoir for this CAES operation scenario. Although the storage reservoir is not real, it is representative in terms of geometry and properties of suitable structures for gas storages. To allow for the use of geological models in numerical simulations, a workflow is developed to consistently transfer these models to numerical simulators including numerical grids and parameters. On the basis of this developed scenario and with the help of the developed workflow, numerical simulations are performed to investigate the reservoir behaviors in the storage formation, dimension the storage capacity, and quantify the induced THC impacts during the storage operation.

Following the objectives proposed in chapter 1, chapter 2 presents the developed realistic and representative CAES operation scenario using a porous formation as the storage reservoir. The characteristics of the used gas turbine are described, such as the required air mass flow rate and air pressure at the turbine inlet. Using the concept of exergy, an estimation of the gas turbine power output is given and later applied in chapter 3 for quantifying potential power outputs of the hypothetical CAES facility. A typical anticlinal structure in the Rhaetian formation is generated for the following numerical simulations of CAES operation. Two cycles of six-hour air injection and six-hour air extraction on a daily basis are designed for operating this hypothetical CAES facility after a two-year initial fill. A plan of gas well configuration is also given based on the estimated well numbers. The fundamental mathematical equations of THC processes are also presented as the theoretical basis for the numerical models.

Based on the developed scenario, numerical simulations are performed in chapter 3 to study the reservoir behaviors of this CAES operation. The profile of pressure response at the bottom hole of gas wells for the initial fill and cyclic operation are presented for a feasibility study in terms of reservoir behaviors. A dimensioning of the storage rates and the storage capacity is given as an estimation of other variations in power outputs, i.e. the continuous time of the designed power output and the instantaneous power output for a short extraction time. Following that, a sensitivity analysis is also performed for estimating power outputs at different permeabilities of the storage formation and different well configurations.

In chapter 4, a quantitative assessment of the induced THC impacts in the storage formation from the CAES operation is given. The hydraulic and thermal impacts of the storage operation are presented as the pressure and the temperature responses in the storage formation. With a prior developed consistent geochemical system for the storage formation, the induced geochemical reactions are assessed and the

impacts on the stored air, the storage formation and the storage operation are investigated.

Chapter 5 presents the developed workflow of transferring heterogeneous complex static geological models to consistent dynamic finite element based numerical models. The technical details of implemented methods are described, including the conversion of numerical grids, the transfer of parameterized properties, and the projection of well trajectories. To test the applicability of the developed tool, a scenario of a deep geothermal exploration in a real geological setting is presented using numerical simulations.

In chapter 6, the general findings based on the results in each chapter are concluded as contributions to large-scale CAES applications in geological porous formations.

2 A scenario of large-scale CAES operation in porous formations

The compressed air energy storage (CAES) operation scenario presented in this chapter includes the definition of four essential parts in such a facility: gas turbine, storage formation, operating schedule and well configurations. Section 2.1 describes the characteristics of gas turbine, which is according to the one used in Huntorf power plant. The quantification of the corresponding power output is given using the concept of exergy. Section 2.2 presents the storage site, which is a typical anticlinal structure in the Rhaetian formation from the North German Basin. The operation of this large-scale CAES is scheduled on a daily basis with a two-year initial fill (see section 2.3). Section 2.4 describes the gas well configuration, based on the well number required and pressure loss in gas wells. Additionally, the fundamental mathematical equations relevant to subsurface thermal, hydraulic, geochemical processes are presented in section 2.5 as the theoretical basis for numerical models.

The scenario described in this chapter has been used in the following published papers:
Wang, B., & Bauer, S. (2017). Compressed air energy storage in porous formations: a feasibility and deliverability study. Petroleum Geoscience, petgeo2016-049. doi:10.1144/petgeo2016-049.
Wang, B., & Bauer, S. (2017). Pressure response of large-scale compressed air energy storage in porous formations. Energy Procedia, 125 doi:10.1016/j.egypro.2017.08.205.

2.1 Gas turbine

The compressed air energy storage (CAES) investigated in this thesis is assumed to be a diabatic CAES which requires additional heat sources to warm up the compressed air during expansion in gas turbine. The Huntorf power plant in Germany is the first commercial diabatic CAES facility in the world having almost 40-year successful operating experience. The gas turbine used in the Huntorf power plant is thus a representative one for the diabatic CAES and is used in this scenario as well. A short description of the Huntorf power plant and the power estimation of its gas turbine is given below.

2.1.1 Huntorf power plant

In 1978, the Huntorf power plant was built in Lower Saxony in northwestern Germany and became the first commercial CAES facility worldwide. The Huntorf power plant was designed to transfer off-peak energy produced by the nuclear power station Unterweser to the high demand periods, and also to stabilize the power grid when some baseload power stations have failures during operation. What makes it possible to have this double-duty is that the gas turbine power station combined with the CAES can reach the intended power output within a few minutes. Because of this fast ramp-up ability, it is considered nowadays

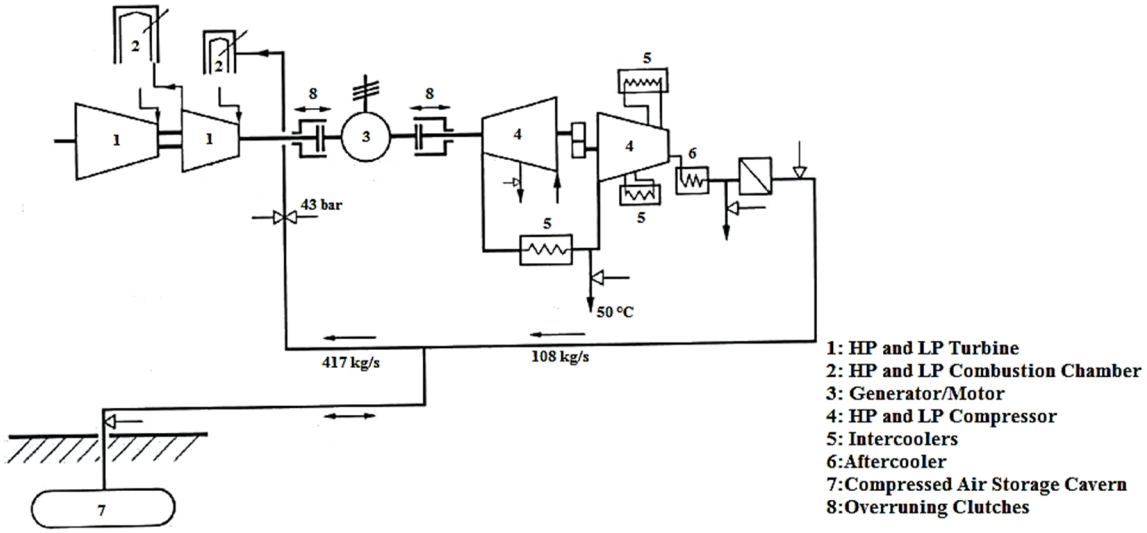

Figure 2.1 Schematic diagram of the Huntorf CAES gas turbine power station (Hoffeins and Mohmeyer 1986)

as a storage option for balancing fluctuations in renewable energy production.

Hoffeins and Mohmeyer (1986) presented a schematic layout of the Huntorf power plant (see Fig. 2.1). It mainly consists of four parts: a compressor set, a gas turbine set, a generator/motor, and subsurface salt caverns to store compressed air. During off-peak load periods with a lower cost, the motor uses overproduced electric power to compress air and store it in the salt caverns in the subsurface. During peak demand periods, the compressed air is withdrawn to the surface and used to burn natural gas in the combustion chambers. The hot gas is then expanded in the gas turbines, spin the generator and produce electric power. In this uncoupled process, a pair of clutches installed in the motor generator enables it to be a motor compressing air during charging phase and a generator producing electricity during air discharging. The corresponding technical data of this operating process are given in Table 2.1 referring to Hoffeins (1994), Crotogino et al. (2001) and Kushnir et al. (2012).

The compressor set installed in the Huntorf power plant includes a low pressure (LP) axial compressor, a high pressure (HP) centrifugal compressor and intermediate coolers. These devices can achieve the smallest possible power requirement in the compression process, which is 60 MW in this case. Before the compressed air is transported to the storage salt caverns, it is cooled again down to 50 °C by an aftercooler. This temperature is set according to the temperature of the salt caverns' wall at an average depth of roughly 650 m. After going through the compressor set, the air mass flow rate is having a constant rate of 108 kg/s with a pressure of maximal 72 bar at the HP compressor outlet.

The gas turbine set in the Huntorf power plant consists of an LP and an HP gas turbine with corresponding combustion chambers. In order to produce constant power, the Huntorf power plant is designed to have a sliding pressure storage meaning that the compressed air leaving the salt

Table 2.1 Technical data of Huntorf power plant (Hoffeins 1994, Crotogino et al. 2001, Kushnir et al. 2012).

Turbomachinery		**Compressor**	**Turbine**
Total power [MW]		60	321 (since 2006)
Air mass flow rate [kg/s]		108	417
Operation (daily) [h]		≤ 12	≤ 3
Inlet conditions			
Pressure [bar]	LP	1	11
	HP	5.6	43
Temperature [°C]	LP	10 (Surface)	825
	HP	223	550
Outlet conditions			
Pressure [bar]	LP	5.7	1
	HP	72 (max)	11
Temperature [°C]	LP	223	400
	HP	50	-
Salt caverns			
Number		2	
Total volume [m^3]		310000	
Operational pressure [bar]	Max	70	
	Min	43	

caverns with variable pressures is throttled down to have a constant pressure. This ensures that the air pressure at the gas turbine set inlet is always constant before entering the combustion chamber. Thus, the compressed air with a pressure of 43 bar flows into the HP combustion chamber of the two-stage gas turbine at a mass flow rate of 417 kg/s. The pressurized air is heated up to 550 °C due to the combustion of natural gas, flows into the first gas turbine and spins the generator to produce power during its expansion. The combustion gases with a lower pressure of 11 bar are further heated up to 825 °C in the LP combustion chamber and expand down to the atmospheric pressure after leaving the second gas turbine.

With the above described processes, the Huntorf power plant can produce 321 MW electric power maximally for 3 hours since an upgrade in 2006 (E.ON SE 2016). To generate this power, it requires an air mass flow rate of 417 kg/s with a pressure of 43 bar at the inlet of the gas turbine set, and an additional input of natural gas at a mass flow rate of 11 kg/s (Hoffeins and Mohmeyer 1986). The cycle efficiency of Huntorf power plant is about 42 %. In 2018, to achieve zero CO_2 emission from operating Huntorf power plant, a research project Huntorf2020 starts and aims to use hydrogen instead of natural gas for the combustion process (Weber et al. 2018). This will bring the conventional Huntorf CAES power plant one step closer towards advancing renewable energy production.

2.1.2 Power output estimation

As one of the Power-to-Power energy storages, CAES stores energy as mechanical energy in the form of pressurized air but of the chemical energy of air. To produce power in CAES, a gas turbine must be used to transfer the mechanical energy to electric power. Thus, the potential power output of CAES can only be estimated based on a specific gas turbine. In this scenario, the

specific gas turbine is the one used in the Huntorf power plant.

To quantify the power output of a gas turbine, a simple exergetic approach can be applied to analyze the useful work potential, i.e. power output, of a gas turbine referring to the two specified states at the inlet and the outlet (Çengel and Boles 2011). Assuming a perfect gas flow in the gas turbine, and neglecting kinetic, potential energy and the energy resulting from combustion, the power output of the gas turbine can be formulated as Eq.(2-1) through its exergy flow (Kim et al. 2012):

$$\dot{E}_a = \dot{M}_a R T_{out} \ln(P_{in}/P_{out}) + \dot{M}_a c_p \left(T_{in} - T_{out} - T_{out} \ln(T_{in}/T_{out})\right) \quad (2\text{-}1)$$

where $\dot{E}_a$ [W] is the total exergy, $\dot{M}_a$ [kg/s] the mass flow rate of the compressed air, R [J/kg/K] the gas constant, T [K] the temperature and P [Pa] the pressure at the turbine inlet and outlet, respectively, and c_p [J/kg/K] the heat capacity of air. The first term of Eq. (2-1) represents the mechanical exergy depending on pressures at the turbine inlet and outlet, and the second term is for the thermal exergy depending on temperatures.

Referring to the technical data of the two-stage gas turbine in the Huntorf power plant (see Table 2.1), air pressures at the inlet and the outlet are 43 bar and 1 bar, respectively. The air temperature at the gas turbine inlet is assumed to be 50 °C, which is the same temperature as the stored air temperature in salt caverns. At the gas turbine outlet, the air temperature is assumed to be 20 °C representing the ambient air temperature in atmosphere. The assumption made for air temperatures for the calculation neglects the additional energy input by burning natural gas (Kim et al. 2012).

For the gas turbine in the Huntorf power plant, mechanical exergy is thus estimated at 134.2 MW and thermal exergy of 0.4 MW for the given air mass flow rate of 417 kg/s. The thermal exergy is much smaller compared to the mechanical exergy because the stored air temperature is low, and thus is omitted here. The power output of the gas turbine in Huntorf power plant is 321 MW, which is larger by a factor of 2.39 compared to the exergy flow estimated here because the energy gained from gas combustion is not included. To account for that, the power output of this gas turbine thus can be estimated by multiplying the factor 2.39 to the exergy flow calculated at a given air mass flow rate (see also Kim et al. (2011)). The estimation method presented here allows for quantifying the storage capacity as potential power outputs based on achievable air flow rates.

2.2 Storage formation

Porous formations in the subsurface are one of the suitable geological formations which can be used for storing compressed air. Compared to salt caverns, underground porous formations have a much wider geological availability in the world. These formations can provide ample storage capacities and exist at different depths underground allowing for different operating pressure for gas turbines. In this scenario, instead of salt caverns used in the Huntorf power plant, a typical geological porous formation in the North German Basin is considered as the storage reservoir for a large-scale CAES operation.

Potentially suitable porous media storage formations are present in the North German Basin, e.g. the middle Bunter sandstone and

the Rhaetian sandstone, which stretches over parts of Germany, Poland, Denmark, the Netherlands and Great Britain (Doornenbal and Stevenson 2010). Among these formations, the Rhaetian sandstone is the youngest part of the Triassic belonging to the Upper Keuper Subgroup (Exter Formation), and is a highly permeable sandstone, which has already been investigated as a potential storage formation for hydrogen storage (Pfeiffer and Bauer 2015; Pfeiffer et al. 2016a, 2017) or CO_2 storage (Mitiku et al. 2013). Therefore, the Rhaetian sandstone is also considered in this scenario as the potential storage formation for the CAES operation.

A suitable geological site for compressed air energy storage must have a highly permeable porous formation and a tight cap rock to prevent a buoyant rise of the air, which ensures the injectivity and confinement of such gas storage. A structural trap for the injected air, such as the anticlinal structure, should be present for the air to be stored near gas wells. A large closure radius is also required for providing a large capacity for the injected air volume. The geological site also needs to be deep enough to fit the operating pressure required at the gas turbine. In the Rhaetian sandstone, anticline structures suitable for CAES can be found in a variety of settings according to the tectonic atlas of Northwest Germany and the German North Sea Sector from Baldschuhn et al. (2001). Anticlines top varies from a depth of about 500 m to 1500 m, the dip angle from about 8 degrees to 34 degrees, the anticline drop from about 480 m to 1400 m and the closure radius from about 1200 m to 8000 m.

Instead of using a specific geological anticlinal site in the Rhaetian formation, a synthetic anticline is generated based on the set of geological data found in the tectonic atlas in order to represent a typical geometrical dimension of these anticlines. The top of this synthetic anticline is assumed at 670 m depth, the drop is 900 m, the closure radius is roughly 3 km and thus the dip angle is approximately 16 degree. The extension of the anticline covers an area of 16 km × 16 km, and the storage formation is formed by a 20 m thick saline formation (i.e. storage formation top is at 700 m depth), bounded by two 30 m thick water saturated but impermeable layers at the top (cap rock) and bottom (see Fig. 2.2). Open hydraulic conditions are assumed at the lateral boundary of the storage formation,

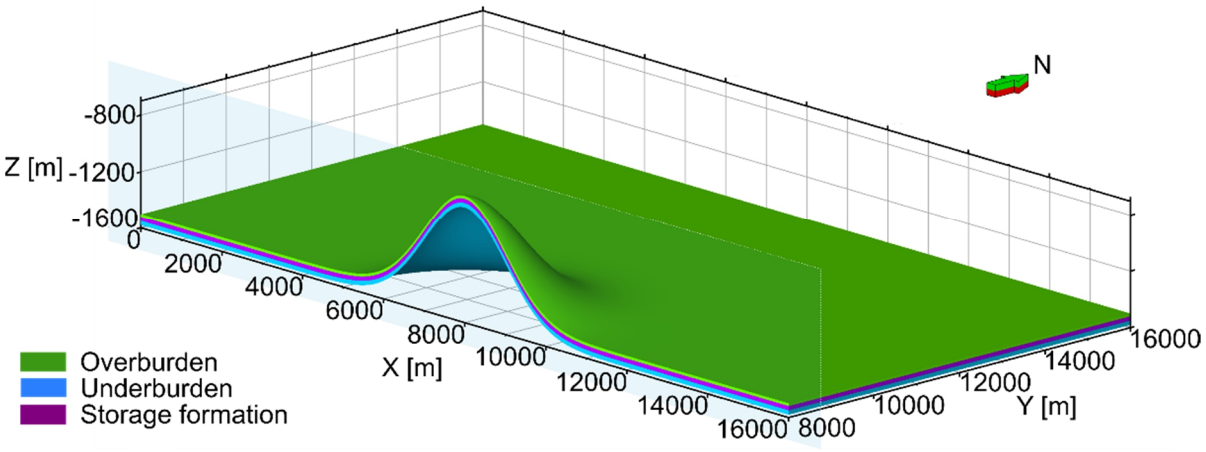

Figure 2.2 A synthetic but typical anticline structure used as a storage site (side view). The overburden forms the tight cap rock.

Table 2.2 The parameters of the synthetic anticline (Hese 2011, 2012; Dethlefsen et al. 2014).

Parameter	Storage formation	Overburden/Underburden
Permeability [mD]	500	1.0×10^{-5}
Porosity [-]	0.35	0.05
Residual gas saturation [-]	0.10	0.30
Residual water saturation [-]	0.20	0.50
Maximum gas phase permeability [-]	0.5	0.1
Brooks & Corey (1964) λ [-], P_d [bar]	2.5, 0.1	2.5, 20
Specific heat capacity [J/kg/K]	475	356
Thermal conductivity [W/m/K]	2.2	2.0
Geothermal gradient [K/km]	25	
Water density [kg/m^3]	1050	
Rock density [kg/m^3]	2650	
Water compressibility [1/bar]	4.50×10^{-5}	
Rock compressibility [1/bar]	4.50×10^{-5}	

which allows for brine outflow and pressure relief.

According to on-site data and statistical studies from the Rhaetian formation (Hese 2011, 2012; Dethlefsen et al. 2014), the synthetic anticlinal storage site is parameterized as the data shown in Table 2.2 representing typical values for the reservoir properties. The storage formation is assumed to be a highly permeable sandstone with an average permeability of 500 mD and a porosity of 0.35. The cap rock and the subjacent formation are impermeable with a permeability of 1.0×10^{-5} mD, a porosity of 0.05 and a high entry pressure of 20 bar. The water density in the storage formation is 1050 kg/m^3 corresponding to a salinity of 2.69 mol/kg at a depth of 700 m.

The mineral compositions of the Rhaetian sandstone at different depths have been collected by Dethlefsen et al. (2014). In the Rhaetian sandstone, quartz is the significantly dominant mineral reaching 85 % in most mineral assemblages or even more, and pyrite can reach up to 6 %. One possible mineral assemblage (see Table 2.3) is considered here to represent the mineral composition of the storage formation in the synthetic anticline, which is also reported by Mitiku et al. (2013) for investigating the induced geochemical reactions by CO_2 storage. In this mineral assemblage, primary minerals are carbonates, silicates, clay mineral K-mica, anhydrite and pyrite. The corresponding fluid chemistry of the formation fluid is shown in Table 2.4. Because the presence of pyrite in the mineral assemblage, the ferrous ion species with a concentration of 0.3 mol/m^3 is found in the formation fluid indicating a redox-sensitive chemical environment. Injecting air into the pore space of the storage formation will lead to oxidation reactions.

Although the anticlinal structure described above is synthetically generated, it is representative for typical anticlinal structures in their geometrical dimensions and parameters. Thus this synthetic anticline is considered as a typical and representative storage site in the Rhaetian formation from the North German Basin which can be used for investigating the large-scale CAES operation in this scenario.

Table 2.3 One possible mineral assemblage of the Rhaetian sandstone formation (see also Mitiku et al. (2013)).

Minerals	Chemical formula	Concentration [mol/m^3_{rock}]	Mass [%]
Albite	$NaAlSi_3O_8$	2.03×10^2	1.7
Anhydrite	$CaSO_4$	5.37×10^2	2.4
Calcite	$CaCO_3$	1.03×10^2	0.3
Dolomite	$CaMg(CO_3)_2$	2.05×10^2	1.2
K-feldspar	$KAlSi_3O_8$	3.47×10^2	3.1
K-mica	$KAl_3Si_3O_{10}(OH)_2$	1.53×10^2	2.0
Pyrite	FeS_2	1.47×10^3	5.7
Quartz	SiO_2	4.27×10^4	83.5

Table 2.4 The fluid chemistry of the Rhaetian sandstone formation (Mitiku et al. 2013).

Species	Reference Concentration [mol/m^3_{liquid}]
Al^{3+}	Not measured
CO_3^{2-}	Not measured
Ca^{2+}	6.83×10^1
Cl-	2.69×10^3
Fe^{2+}	3.00×10^{-1}
K^+	6.80
Mg^{2+}	3.21×10^1
Na^+	2.51×10^3
SO_4^{2-}	9.40
Si^{4+}	Not measured
pH [-]	Not measured

2.3 Operating schedule

The storage formation is initially saturated with saline water, and thus an initial fill with air is required to create a gas reservoir for the cyclic storage operation. Based on the results from preliminary numerical simulations, the operating schedule of the initial fill is designed and described as follows in section 2.3.1. The duty of the CAES facility in this scenario is designed to mitigate diurnal fluctuations expected in energy production from renewable sources, i.e. shift off-peak energy to peak demands on a daily basis. The cyclic operation is thus scheduled as a daily operation with two periods of six-hour energy production in the early morning and the late afternoon (see section 2.3.2).

2.3.1 Initial fill

For gas storages in porous formations, the initial fill of gas is required to create a gas reservoir in water-saturated porous medium ensuring the deliverability of gas flow during the storage operation. The initially filled gas is often termed as cushion gas (Katz 1959), which usually stays in the gas reservoir and is not withdrawn. Allowing for CAES operation in the deep saline aquifer described in section 2.2, an initial fill is also required, and the air is used as the cushion gas in this scenario.

Injecting air into the storage formation fully saturated with the saline water, a pressure build-up is expected at gas wells which is proportional to the injected air flow rate. The pressure increase at gas wells in the storage reservoir is a potential risk of inducing fractures in cap rock and reservoir

rock. To avoid that, a maximum pressure of 150 % of the initial hydrostatic pressure in the storage formation at the bottom holes of gas wells is applied to find suitable air injection mass flow rates for the initial fill (e.g. see also Benisch and Bauer 2013; Mitiku and Bauer 2013).

Since air and saline water are two non-miscible fluids with a significant difference in their densities and viscosities, the air injected into the storage formation will rise up due to the buoyancy effect till the cap rock and travel further instead of accumulating at the top of the anticline due to the pressure gradient. Besides, fingering can also happen in the heterogeneous storage formation leading to entrapped air. Both phenomena are bad for obtaining a well-mixed gas phase of the cushion gas in the storage reservoir. Therefore, lessons learned from natural gas storage show that the initial fill of cushion gas can be operated with shut-in periods in between to minimize the buoyancy effect and obtain a well-mixed cushion gas required to support the high injection and extraction rates in CAES operation (The HYDROdynamics Group LCC 2005, 2011).

CAES stores the energy in the form of pressurized air, and thus any pressure loss during cyclic operation in the storage reservoir should be avoided. One possible pressure loss is the movement of the gas-water contact caused by air injection during the storage operation. To ensure a stable gas-water contact at the edge of the gas reservoir, a large amount of cushion gas is required, which should be at least ten times larger compared to the cyclic amount of air recommended by The HYDROdynamics Group LCC (2011). Besides, the spatial extension of the created gas reservoir needs to be large enough to place the gas wells.

In this scenario, with preliminary numerical simulations, an initial fill with air is thus scheduled with five cycles in 2 years, which are 100 days of injection using a rate of 9.62 kg/s, 100 days of shut-in, 4 times 35 days of injection using a rate of 16.98 kg/s, 3 times 70 days shut-in in between and 181 days shut-in after the 5th injection. After the initial fill, an air reservoir is created with a mass of 2.88×10^8 kg and a radius of roughly 500 m. The air in place as the cushion gas is much larger compared with the cyclic air mass, which is approximately 9.0×10^6 kg (see section 2.3.2).

2.3.2 Daily operation

With a continuous increase of renewable energy production in electric power grids, Morris and Pehnt (2016) estimated that in the year of 2020 in Germany, power demands may be covered by the combination of renewable energy production with pumped hydro storages without any baseload power plants (see Fig. 2.3), e.g. nuclear power plant or coal and gas power plant. The high share of solar energy sources makes the daily power production look like a “dental chart” indicating very strong fluctuations, and the gray area represents the peak demand. Clearly, in such an electric power grid, a fleet of dispatchable or peaking power plants is required. These power plants can have high flexibility, and also ramp up and down quickly to compensate this fluctuation. The CAES power plant in this scenario fit precisely for this purpose, which can shift off-peak energy potentially overproduced around noon to peak demands on a daily basis.

An estimate given by Morris and Pehnt (2016) shows that on a typical working day

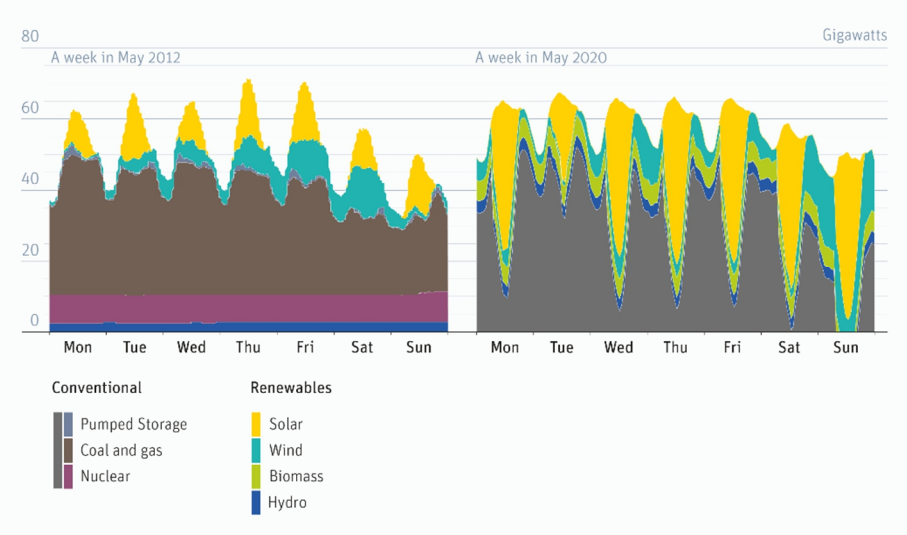

Figure 2.3 Estimated power demand over a week in 2012 and 2020, Germany (Morris and Pehnt 2016).

in Germany, the power demand picks up around 3 a.m. and falls around 9 p.m. (see Fig. 2.4). Around the middle of the day from 9 a.m. to 3 p.m., the energy produced by solar power plants can cover more than a third of peak demand around noon based on the data in May 2017. With the estimation shown in Fig. 2.3, the peak demand around noon may be eventually all covered by the energy produced by solar power plants, which also possibly results in an overproduction. This lead to lower profits for the conventional baseload power plant owners, but a perfect time slot for recharging the storage of peaking power plants.

The above estimations on power demand and energy production are typical scenarios expected in Germany with the on-going transition of the energy supply from carbon-rich fossil fuels to renewable energy sources. Therefore, the daily operating schedule of the hypothetical CAES power plant in this scenario is correspondingly designed as shown in Fig. 2.5. The CAES power plant is assumed to produce electric power for six hours in the morning from 3 o'clock to 9 o'clock and again in the

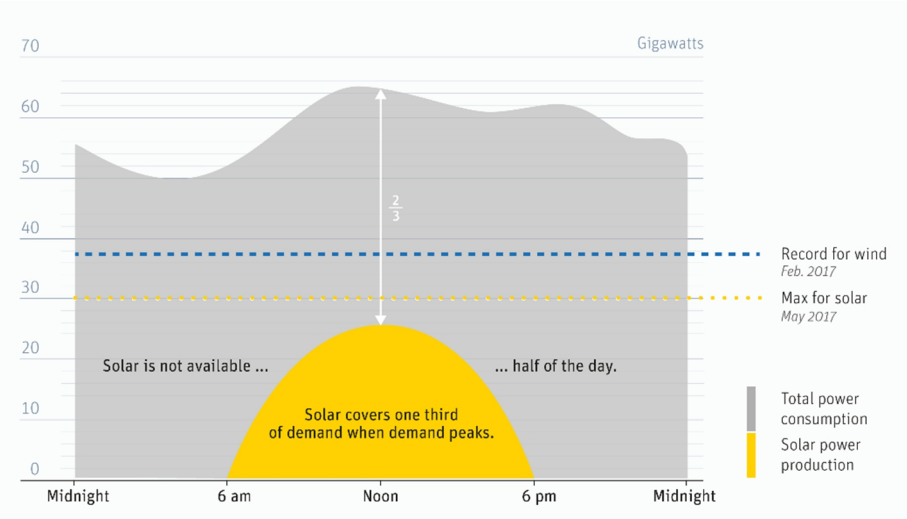

Figure 2.4 Power demand and solar power production in Germany, estimate based on actual data from February 2017 (Morris and Pehnt 2016).

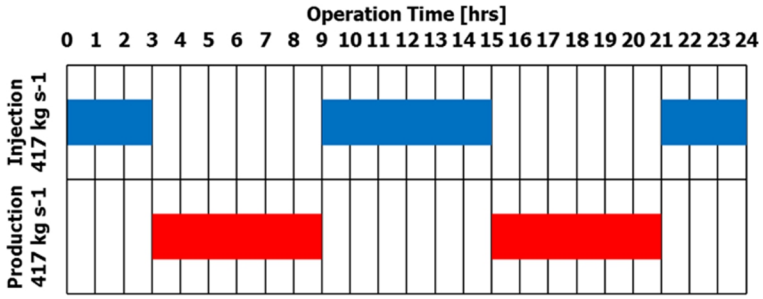

Figure 2.5 The daily operating cycle of the hypothetical CAES facility.

afternoon from 15 o'clock to 21 o'clock. Times of no production around noon and late around midnight are used to inject air and thus recharge the storage. The air mass flow rate during power production is 417 kg/s referring to the requirement of the gas turbine, and during recharging, the injection air mass flow rate is assumed to be the same as the extraction air mass flow rate.

2.4 Well configuration

CAES using porous formations as a storage reservoir requires gas wells for air injection and extraction. In this scenario, gas wells are placed vertically, which has a production string at a diameter of 20 inches and uses fiberglass reinforced plastic as inner material referring to gas wells used in the Huntorf power plant (Crotogino et al. 2001). To plan a well configuration, the number of gas wells must be given, which depends on the reservoir properties and the bottom hole pressure (BHP) required. The BHP is determined by the pressure required at the well head and the pressure loss in the wellbore. The well head pressure in this scenario is assumed to 43 bar according to the pressure required at the gas turbine inlet, and the pressure loss is estimated accordingly using an analytical solution from Hagoort (1988) for gas flow in the wellbore (see section 2.4.1). Based on the required BHP, twelve vertical gas wells are determined for this CAES operation, and a plan of well placement is given in section 2.4.2.

2.4.1 BHP required at gas wells

Due to the frictional and gravity forces, pressure loss happens in the discharging air through gas wells. Accounting for pressure loss in the wellbore, an analytical solution from Hagoort (1988) can be applied to evaluate the BHP at gas wells based on a pressure defined at the well head (see Eq. (2-2)). This solution is derived assuming no water phase is present in the discharged air.

$$P_{wh} = P_{bh} \times \left\{ exp(-2N_{gp}) + \frac{N_{fp}}{2N_{gp}} \left[exp(-2N_{gp}) - 1 \right] \right\}^{1/2} \quad (2\text{-}2)$$

where, P_{wh} [Pa] is the pressure of the compressed air at the well head, P_{bh} [Pa] the air pressure at the well bottom hole, N_{gp}[-] and N_{fp} [-] dimensionless numbers defined as

$$N_{gp} = \frac{gL\cos\alpha}{Z_{av}RT_{av}} \quad (2\text{-}3)$$

$$N_{fp} = \frac{4Z_{av}f_{av}\dot{M}_a^2RT_{av}}{{P_{bh}}^2A^2d_wM_a}L \quad (2\text{-}4)$$

where, $\dot{M}_a$ [kg/s] is the mass flow rate of the compressed air, L [m] the length of the wellbore, Z_{av} [-] average compressibility factor of the compressed air, T_{av} [K] the average temperature of the compressed air in the wellbore, R [J/kg/K] gas constant, g [m/s^2] gravity constant, α [degree] the deviation angle of the wellbore, A [m^2] the area of the wellbore cross-section, d_w [m] the diameter of the wellbore, and f_{av} [-] the average fanning friction factor of 8.5×10^{-3} estimated after Goudar & Sonnad (2008) depending on the Reynolds number and the roughness of the inner surface of the wellbore.

In this scenario, the air pressure at the well head is assumed to be 43 bar, which is the pressure required at the gas turbine inlet if the pressure loss in surface pipelines is omitted. A total air mass flow rate of 417 kg/s is required by the gas turbine to produce 321 MW power. To ensure a well head pressure of 43 bar and a total air mass flow rate of 417 kg/s, the BHP at gas wells is estimated for different numbers of wells (see Fig. 2.6). Results show that if only one well is used, the BHP is found to be 50.2 bar with a pressure loss of 7.2 bar. Using three or more wells, the BHP is estimated around 46.5 bar indicating that a pressure loss of roughly 4 bar is expected. Therefore, to achieve a well head pressure of 43 bar, the BHP at gas wells needs to be 47 bar to overcome the pressure loss in the wellbore if three or more wells are used.

2.4.2 Well number and placement

An analytical solution (see Eq. (2-5)) after Katz (1959) is used by reservoir engineers to describe the gas flow deliverability of a single well in natural gas fields, showing that the flow deliverability is proportional to the reservoir permeability and thickness. For CAES operation, the air flow rate can be roughly estimated using this analytical solution for determining the well number assuming the skin factor is zero.

$$q_{st} = \frac{T_{st} Z_{st} P_{st} K_g \pi h \left(P_{rs}{}^2 - P_{bh}{}^2\right)}{\mu_g T_{rs} Z_{rs} ln\left({}^{r_{rs}}/_{r_w}\right)} \qquad (2\text{-}5)$$

where, q_{st} [m^3/s] is the air volume flow rate at surface condition, K_g [m^2] the maximum permeability for air flow, h [m] the thickness of the air reservoir, P_{st} [Pa] the pressure at the surface condition, P_{rs} [Pa] the pressure at the reservoir edge, P_{bh} [Pa] the pressure at the bottom hole of the gas wells, μ_g [Pa·s] the air viscosity at the reservoir condition, T_{rs} [K] the air temperature in the reservoir, T_{st}[K] the air temperature at the surface condition, Z_{rs} [-] air compressibility factor at reservoir

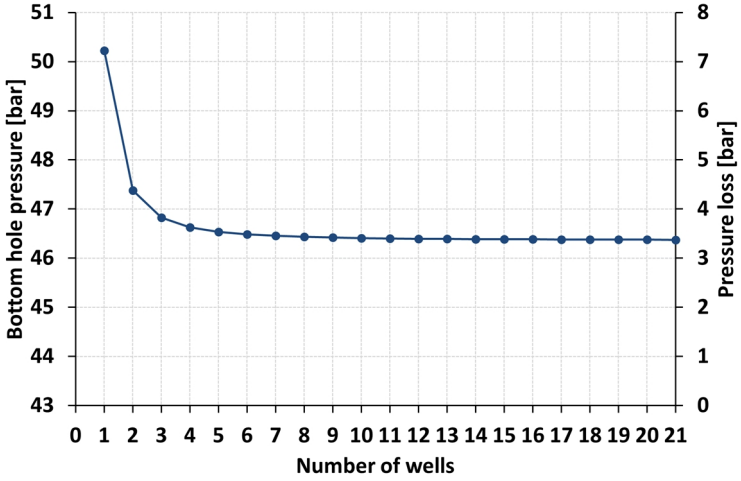

Figure 2.6 Bottom hole pressure (BHP) at a given well head pressure of 43 bar and the corresponding pressure loss between BHP and well head pressure.

condition, Z_{st} [-] air compressibility factor at surface condition, r_{rs}[m] the radius of the air reservoir, r_w [m] the radius of the gas wells.

Preliminary simulation results show that after the initial fill, the gas reservoir has a radius of roughly 500 m and the gas-water contact is at a depth of about 800 m. If the hydrostatic pressure of 80 bar is assumed at the edge of the gas reservoir, an air flow rate of 50 kg/s for a single well is calculated based on Eq. 2-5 for the required BHP of 47 bar. If the air flow rate in each gas well is considered identical, nine wells are therefore needed to deliver the air flow at a rate of 417 kg/s for a storage reservoir with a permeability of 500 mD.

The analytical solution is a steady-state solution for the airflow deliverability in a single well, the well interference between gas wells over an extraction period is not accounted for and thus the number of wells required can be underestimated. However, using this analytical solution can give a quick estimation of the minimum number of gas wells required and offer a starting point for determining well numbers using numerical simulations. Preliminary reservoir simulations of CAES operation (see also section 3.5.1) show that twelve vertical gas wells are actually required for delivering the air mass flow rate of 417 kg/s over a six-hour extraction. In the gas reservoir with a radius of roughly 500 m, a minimum distance of 200 m between wells is determined and the placement is shown in Fig. 2.7, which are symmetric at x- and y-axis. The gas wells are fully penetrated in the storage formation having a well screen length of 20 m.

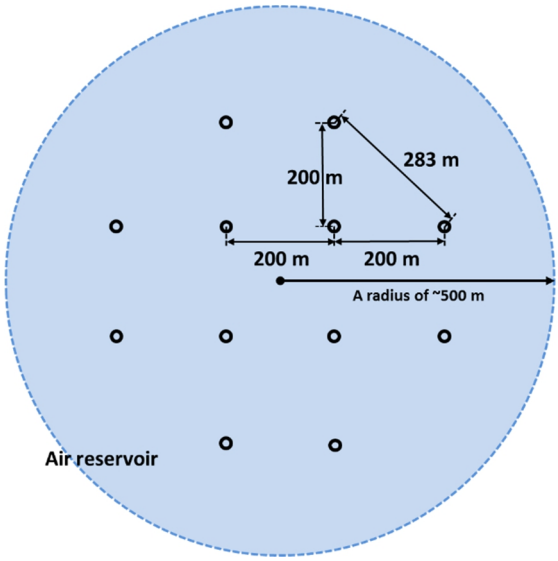

Figure 2.7 Well placement in the gas reservoir with a radius of roughly 500 m. Black hollow circles represent the location of gas wells with a minimum distance of 200 m.

2.5 Mathematical formulations on subsurface processes

Storing compressed air in subsurface geological porous formations involves hydraulic (H), thermal (T), geochemical (C) and geomechanical (M) processes in a multiphase-multicomponent system. This system consists of a gas phase, i.e. stored air, a liquid phase, i.e. formation water, and the solid phase, i.e. the rock and its mineral composition. Since the investigation of geomechanical processes is beyond the scope of this thesis, a brief description of the general mathematical formulations on THC processes is given in this section.

2.5.1 Hydraulic process

The general form of the multiphase flow equation for a phase i can be given as (Helmig 1997):

$$\frac{\partial(\rho_i \phi S_i)}{\partial t} - \nabla\left(\rho_i \frac{K_{ri}}{\mu_i} K(\nabla P_i - g\rho_i)\right) = q_i \rho_i \tag{2-6}$$

where ρ_i [kg/m^3] is the density of the phase i, ϕ [-] the porosity, S_i [-] the saturation, K_{ri} [-] the relative permeability, μ_i [Pa·s] the viscosity of the phase , K [m^2] the intrinsic permeability, P_i [Pa] the phase pressure, g [m/s^2] the gravity constant and q_i [m^3/s] the source and sink terms.

Here, the multiphase stands for the wetting phase, i.e. formation water, and the non-wetting phase, i.e. stored air. These two phases have supplementary constrains to Eq. (2-6) as:

$$\sum_{i=1}^{2} S_i = 1$$

and

$$P_{cwg} = P_w - P_g = f(S_w, S_g)$$

This means that the gas and water phases are related by the capillary pressure P_{cwg} [bar] and the saturation from both phases must sum up to unity. The relative permeability K_{ri} and the capillary pressure P_{cwg} of the porous formation can be estimated, e.g. after Brooks and Corey (1964) with the parameters listed in Table 2.2. Fluid properties of a phase i can be evaluated by equations of state with correlations to temperatures and pressures, such as the Peng–Robinson equations of state (Peng and Robinson 1976).

2.5.2 Thermal process

For a multiphase system, the general form of the heat transport can be formulated as Eq. (2-7), assuming the system is in thermal equilibrium locally (Bear and Bachmat 1990). Thus, the temperature represents an equilibrated temperature of three phases, i.e. stored air, formation water, and rock.

$$\frac{\partial (c\rho\, T)}{\partial t} + \sum_{\alpha}^{2} \nabla(\phi S_i c_i \rho_i v_i T) - \nabla(D^T \nabla T) = Q^T \quad (2\text{-}7)$$

where T [K] is the equilibrated temperature, $c\rho$ [J/m^3/K] the heat capacity of the three phases, D^T [W/m/K] the thermal diffusion-dispersion coefficient and Q^T [J/s] the heat source and sink terms. The heat capacity of the three phases can be formulated as Eq. (2-8) and the thermal diffusion-dispersion coefficient as Eq. (2-9) if volumetric rules are applied.

$$c\rho = (1-\phi) c_s \rho_s + \sum_i^2 (\phi S_i c_i \rho_i) \quad (2\text{-}8)$$

where c_s [J/kg/K] is the specific heat capacity of rock and c_i [J/kg/K] the specific heat capacity of a fluid phase α, i.e. formation water and stored air.

$$D^T = (1-\phi)\lambda_s + \sum_i^2 (\phi S_i \lambda_i) + \sum_i^2 (\phi S_i D_i^t) \quad (2\text{-}9)$$

where λ_s [W/m/K] is the thermal conductivity of rock, λ_i [W/m/K] the thermal conductivity of the fluid phase i and D_i^t [W/m/K] the thermal dispersion coefficient.

During the CAES cyclic operation away from gas wells, the air always expands regardless of injection or extraction due to the change in pressure driving flow. For a real gas, a temperature dependent term on pressure change can be quantified by the Joule-Thomson coefficient as Eq. (2-10). For air, the Joule-Thomson coefficient is positive meaning pressure decrease leads to a cooling of air.

$$\mu_{JT} = \left(\frac{\partial T_g}{\partial P_g}\right)_H \quad (2\text{-}10)$$

where μ_{JT} [K/pa] is the Joule-Thomson coefficient, T_g[K] gas temperature, P_g [pa] gas pressure and H stands for the condition of constant enthalpy.

2.5.3 Chemical process

Injecting air into geological formations leads to a dissolution of air components in

formation water. The dissolved components can induce geochemical reactions resulting in mineral dissolution and precipitation. A general rate law for quantifying the change in minerals due to dissolution and precipitation can be written as (Appelo and Postma 2005):

$$\frac{dm}{dt} = -A_{react} \cdot k \cdot g(c) \cdot (1 - \frac{IAP}{K_s}) \tag{2-11}$$

where $\frac{dm}{dt}$ shows the overall reaction rate in [mol/s], m [mol] is the moles of mineral at a given time, t [s] the reaction time step, k [mol/m^2/s] the specific rate constant, A_{react} [m^2] the mineral reactive surface area, $g(c)$ a function accounting for the effects of the solution composition, such as pH, on mineral dissolution and precipitation rate (Lasaga 1998), IAP [-] Ion Activity Product, S [-] the solubility product and the ratio $\frac{IAP}{K_s}$ the saturation state of minerals at a given time. Thus, $(1 - \frac{IAP}{K_s})$ determines whether minerals are dissolving or precipitating by correcting the sign of Eq. (2-11).

The reactive surface area A_{react} can be calculated as the following equation (Klein et al. 2013):

$$A_{react} = \alpha \cdot A_{geom} \cdot m \cdot M_s \tag{2-12}$$

where α [-] is a factor accounting for the selective sites of mineral surface area involved in reactions, M_s [g/mol] the molar weight of minerals and A_{geom} [m^2/g] the mineral geometric surface area. The geometric surface can be calculated based on the following equation, assuming mineral particles are spherical (Cantucci et al. 2009; Klein et al. 2013):

$$A_{geom} = \beta \cdot \frac{6}{\rho_s \cdot d_s} \tag{2-13}$$

where ρ_s [kg/m^3] is the mineral density, d_s [m] the average grain diameter and β [-] a factor accounting for the roughness on mineral surfaces. If assuming a smooth surface, β equals one.

The specific rate constant k together with the function $g(c)$, i.e. the term $k \cdot g(c)$, for mineral dissolution and precipitation can be formulated according to Palandri and Kharaka (2004) as follows:

$$\begin{aligned} k \cdot g(c) = {} & k_s + \\ & k_{25}^{neutral} exp\left[\frac{-E_a^{neutral}}{R}\left(\frac{1}{T} - \frac{1}{298.15}\right)\right] \\ & + k_{25}^{acid} exp\left[\frac{-E_a^{acid}}{R}\left(\frac{1}{T} - \frac{1}{298.15}\right)\right] a_H^{n_H} \\ & + k_{25}^{base} exp\left[\frac{-E_a^{base}}{R}\left(\frac{1}{T} - \frac{1}{298.15}\right)\right] a_{OH}^{n_{OH}} \end{aligned} \tag{2-14}$$

where k_s [mol/m^2/s] is the rate constant due to other mechanisms, k_{25} [mol/m^2/s] the rate constant at 25 °C, E_a the activation energy in [J/mol], R the gas constant in [J/mol/K] , T [K] absolute temperature in the storage reservoir and $a_i^{n_i}$ the reaction order n_i with respect to the activity of species a_i.

As a result of mineral dissolution and precipitation reactions, a change in porosity and also permeability may occur. This effect is accounted for by changing porosity in balancing the mineral volume change due to the reactions (see Eq. (2-15)). The corresponding permeability change can be determined by a Kozeny-Carman porosity-permeability model (Bear 2013) as Eq. (2-16).

$$\phi_{t+\Delta t} = \phi_t + (1 - \phi_t) \sum_n^j [MV^n (m_t^n - m_{t+\Delta t}^n)] \tag{2-15}$$

$$K_t = K_{t0} \left(\frac{1-\phi_{t0}}{1-\phi_t}\right)^2 \left(\frac{\phi_t}{\phi_{t0}}\right)^3 \tag{2-16}$$

where ϕ [-] is the porosity, j the total number of minerals, MV^n [m^3_{rock}/mol] the molar volume of mineral n, m^n [mol] the mole of mineral n and K [m^2] the permeability.

2.6 Summary

A realistic and representative scenario of large-scale CAES operation in a geological anticline is developed in this chapter. It is a conventional diabatic CAES, which only stores the mechanical energy of the compressed air, i.e. in the form of high pressure, and does not reclaim the heat from air compression.

In this scenario, the gas turbine setup of the Huntorf power plant is used, which requires an air mass flow rate of 417 kg/s with a minimum turbine inlet pressure of 43 bar to produce 321 MW electric power. The exergy flow of the Huntorf gas turbine is estimated at 134 MW based on the air mass flow rate and the minimum inlet pressure representing the potential work done by compressed air without adding natural gas. The actual power output of this gas turbine can be estimated by multiplying a factor of 2.39 to the exergy flow calculated accounting for the additional energy input from the combustion of natural gas.

Instead of two salt caverns, a porous storage formation in an anticlinal structure is used as the storage reservoir. The anticline storage site is synthetically generated based on the typical geometrical data of suitable anticline structures found in the Rhaetian formation from the North German Basin. The anticline top is assumed to be at a depth of 700 m, the drop to be 900 m, with a closure radius of roughly 4 km and thus a dip angle of roughly 16 degree. The storage formation in this anticline is a homogenous permeable 20 m-thick saline aquifer bounded by two 30 m-thick impermeable layers. The lateral extension of the anticline is about 16 km. Open hydraulic boundary conditions are assumed, which allow for brine outflow and pressure relief. Based on the on-site data and the statistical study from the Rhaetian formation in the North German Basin, the storage formation is assumed to have an average permeability of 500 mD and a porosity of 0.35. One representative mineral assemblage of the storage formation shows the presence of carbonates, silicates, clay mineral K-mica, anhydrite and pyrite as primary minerals. The fluid chemistry indicates that the storage formation has a redox-sensitive chemical environment, and thus oxidation reactions are expected after injecting air into the pore space.

Allowing for cyclic operation, an initial fill with air is scheduled with five cycles in 2 years to create a gas reservoir having a radius of roughly 500 m. Due to the fast growth of power generation from photovoltaics, surplus energy is predicted as being highest at around noon. Add-on power would thus be required in the morning and evening. A daily operational cycle is thus assumed to produce power using the air storage for 6 hours in the morning (3 a.m. to 9 a.m.) and again in the afternoon (3 p.m. to 9 p.m.). Times of no production, i.e. around noon and midnight, are used to recharge the storage by using surplus electricity to inject the air. Both the injection and extraction air mass flow rate are set to 417 kg/s.

To support 6 hours of continuous power production as defined in this scenario, twelve vertical wells with a minimum distance of 200 m are required. Similar to

the wells used in the Huntorf power plant, wells in the scenario are assumed to have a 20-inch production string and fiberglass-reinforced plastic as the inner material. The average pressure loss within each well from the bottom hole to the well head is estimated as 4 bar, which means a minimum well BHP of 47 bar is required in order to maintain an air pressure of 43 bar at the gas turbine inlet.

3 Feasibility and storage capacity

The following chapter presents a feasibility study and a dimensioning of achievable storage capacity and storage rates for the compressed air energy storage (CAES) scenario presented in chapter 2. The numerical simulations are performed using ELCIPSE reservoir simulator and a description of model setup is given in section 3.2. Section 3.3 presents the pressure responses at the bottom of gas wells during the initial fill and the cyclic operation for the feasibility investigation. An estimation of other achievable air flow rates are given in section 3.4 for dimensioning the storage capacity and the storage rates. The section 3.5 presents a sensitivity analysis on the potential storage rates and capacity accounting for different permeabilities and well configurations.

Parts of this chapter are published as
Wang, B., & Bauer, S. (2017). Compressed air energy storage in porous formations: a feasibility and deliverability study. Petroleum Geoscience, petgeo2016-049. doi:10.1144/petgeo2016-049.
Wang, B., & Bauer, S. (2017). Pressure response of large-scale compressed air energy storage in porous formations. Energy Procedia, 125 doi:10.1016/j.egypro.2017.08.205.

3.1 Introduction

The transition of the energy supply from carbon rich fossil fuels to renewable energy sources, termed the “Energiewende” in Germany, is pursued by many countries in the world as a means of reducing greenhouse gas emission and mitigating climate change effects (Morris and Pehnt 2012; IPCC 2014). For example, in 2014, the share of renewable energy in Germany’s energy supply reached 27.8 % and prospectively increases to 40 % – 45 % in 2025 (BMWi 2015) and may reach 100 % by 2050 (UBA 2010). Major renewable energy sources are electric power generation by wind or solar power plants, which causes strong temporal fluctuations of the generated power due to the short term weather conditions. The possible solutions, such as grid-scale storage systems, improvement of cross-border grid connectivity and electrical demand-side management can be used to compensate these fluctuations (Sterner and Stadler 2014). Grid-scale stand-by storage systems are flexible in terms of different time scales. In order to stabilize the power grid and meet the demand during times of low renewable power production, a storage demand for Germany of up to 50 TWh electrical energy by 2050 may be required (UBA 2010). Besides pumped hydro storage as the main large scale above ground storage option (Sterner and Stadler 2014), subsurface geological storage has the largest potential to provide such large storage capacities on the longer time scales required (Bauer et al. 2013). Storage options include underground storage of natural gas (e.g. Bary et al. 2002), which accounts for about 20% of yearly demand in Germany in both salt cavern and porous formation storages (LBEG 2015), underground storage of hydrogen produced from surplus electric power via electrolysis (Pfeiffer and Bauer 2015; Reitenbach et al. 2015; Pfeiffer et al. 2016a, 2017),

compressed air energy storage (Crotogino et al. 2001) or subsurface storage of heat (Popp et al. 2016; Boockmeyer and Bauer 2016).

Compressed air energy storage (CAES) is seen as a promising option for balancing short term diurnal fluctuations from renewable energy production, as it can ramp output quickly and provide efficient part-load operation (Succar and Williams 2008). CAES is a power-to-power energy storage option, which converts electricity to mechanical energy and stores it in the subsurface (Sternberg and Bardow 2015). For CAES, off-peak energy is used to store energy as highly compressed air, which is used to generate power through gas turbines during times of peak demand. Subsurface storage of compressed air in salt caverns or porous formations offers large storage capacities. Currently, only two CAES facilities, i.e. in Huntorf in Germany and in McIntosh in the US are operating, both using subsurface salt caverns as reservoir for the compressed air (Raju and Khaitan 2012). Salt caverns can be mined at different depths within a suitable salt dome, which allows for a range of operation pressures. There is no inherent limitation on the deliverable air flow rates, like the hydraulic permeability in porous formations (Kushnir et al. 2012b). These can allow a better control on reservoir conditions with the use of salt caverns compared to porous formations. Nonetheless, porous formations have much wider geological availability compared to rock salt suitable for caverns and may provide much larger storage capacities (Kepplinger et al. 2011). Furthermore, the capacity of a porous formation storage can be extended by injecting additional air to develop a larger gas reservoir, or by drilling additional wells. Increasing the cavern size also increases the risks of instability (Succar and Williams 2008), so that additional caverns have to be constructed if storage size is increased. A first study of CAES using a porous formation was conducted in Pittsfield, Illinois, which shows that the concept is feasible at this site (ANR Storage Company 1990). A review by Succar and Williams (2008) comprehensively describes the technical and economic possibilities of large-scale CAES storage sites with wind farms, and also addresses the possibilities when using a porous formation as CAES storage reservoir. However, a planned CAES facility in a porous formation in Iowa was stopped due to inadequate local geological conditions as well as energy market reasons (Schulte et al. 2012).

So far, research has focused on studying feasibility of CAES using salt caverns as storage reservoirs to investigate hydraulic, thermal and mechanical behaviors during operation (Heusermann et al. 2003; Kushnir et al. 2012b; Nazary Moghadam et al. 2013; Khaledi et al. 2016a, b), as well as on CAES technology developments yielding optimized CAES plant configurations with enhanced efficiency (Nakhamkin et al. 2009; Ibrahim et al. 2010; Hartmann et al. 2012; Luo et al. 2016). Regarding underground CAES in porous formations, Kushnir et al. (2010) performed a simplified analytical investigation of a compressible gas flow within CAES porous formation storage reservoirs to calculate the optimal critical air flow rate for different formation thicknesses, well screen lengths and diameters etc.. Pei et al. (2015) analyzed the performance of a CAES plant for different permeabilities of the storage formation by analytical thermodynamic calculations and stated that both thermal and exergy

efficiencies increase with increasing permeability. Oldenburg & Pan (2013a, 2013b) simulated an idealized gently domed CAES porous formation storage and proved the feasibility of CAES operation using a single wellbore. One attempt of a large-scale field application is the Iowa Stored Energy Park planning a 270 MW CAES facility, but it is failed due to the site geological limitations mainly in permeability (Schulte et al. 2012). The unexpected low permeability in the storage formation leads to an insufficient air extraction rate and the planed 270 MW power output is thus not possible. Lessons learned from that is, based on the geological conditions of underground porous formation, a feasibility study of storage operation in terms of reservoir behaviors, e.g. airflow deliverability and storage pressure responses, is required. Referring to the uncertainty in reservoir properties, a dimensioning of storage capacity, such as possible deliverable rates and their duration, is helpful for planning large-scale CAES application in porous formations.

Therefore, the work presented in this chapter investigates the feasibility of a large-scale CAES operation based on the scenario developed in chapter 2, which is a hypothetical conventional CAES plant analogous to the Huntorf power plant in a geologically representative anticline site from the North German Basin. The feasibility of this CAES facility is investigated numerically by simulating reservoir behaviors during storage operation. For dimensioning the potential storage rates and storage capacity, the formation deliverability and the corresponding power output of the CAES plant are determined for different operating conditions and a sensitivity analysis is performed accounting for different formation permeabilities and well configurations.

3.2 Simulation setup

The numerical simulations are performed using the oil and gas reservoir simulator ECLIPSE 300 in compositional mode (Schlumberger 2016), in which compressed air is considered as a compositional gas of 78 % N_2, 21 % O_2 and 1 % Ar. Only the storage formation of the geological anticline is simulated, as the cap rock and bottom rock layers are assumed impermeable. The storage formation represents a homogeneous sandstone reservoir of 20 m thickness with a high-permeability of 500 mD, and the corresponding parameters are listed in Table 2.2. The capillary pressure-saturation function of the reservoir is determined by the Brooks and Corey (1964) correlation. Using compositional gas parameters listed in Table 3.1, air properties are calculated by a generalized form of the Peng-Robinson equations of state (Peng and Robinson 1976; Schlumberger 2016) in simulations. The gas flow close to wells is

Table 3.1 The parameters of air components N_2, O_2, and Ar (Lemmon et al. 2000; Kaye and Laby 2016).

Parameter	N_2	O_2	Ar
Critical Temperature	126.192 K	154.581 K	150.687 K
Critical Pressure	33.95 bar	50.43 bar	48.63 bar
Critical Molar Volume	8.95×10^{-5} m^3/mol	7.34×10^{-5} m^3/mol	7.46×10^{-5} m^3/mol
Acentric Factor	0.037	0.022	-0.002

simulated as laminar flow, not accounting for effects of non-Darcy flow, which might in this case slightly lower extraction rates.

Due to the symmetry of the structure and well configuration shown in Fig. 2.7, only a quarter of the anticline is simulated, in which three vertical fully penetrating wells (well I1, I2 and I3) are placed with a minimum distance of 200 m in between (Fig. 3.1). The total injection and extraction air mass flow rates of 417 kg/s are distributed to the twelve wells. The model domain is thus 8 km × 8 km × 20 m, and is discretized into 72 × 72 × 15 cells. A finer horizontal discretization of 10 m is used around the wells and a coarser discretization of 500 m at the model boundary. Vertical discretization uses cells of 1 m thickness at the top and coarser cells of 2 m thickness at the bottom. Close to well I1, the grid is locally refined again (horizontally from 0.5 m to 5 m; vertically to 1 m) to capture the pressure response near the well. It was found that this Tartan-type local grid refinement does not introduce numerical artifacts into the model results.

The initial pressure distribution is hydrostatic with 71.95 bar at 720 m depth. A threshold pressure of 47 bars is set to each well bottom hole during extraction to ensure the minimum gas turbine inlet pressure. Additionally, to avoid possible induced fractures in the reservoir rock during injection (e.g. Benisch and Bauer 2013; Mitiku and Bauer 2013), a maximum pressure of 150 % of the initial hydrostatic pressure at each well bottom hole, i.e. of 108 bar, is applied.

As the aquifer of the storage formation is laterally not closed, extended hydraulic boundary conditions are assigned at the model boundaries, by considering an additional lateral extension of the storage formation by 12 km in each direction, which allows for brine (with a salinity of 2.69 mol/kg (Mitiku and Bauer 2013)) outflow and pressure relief. This boundary condition is included by changing the pore volume of the outermost model cells, which represents this additional volume. At 20 km from the center of the storage, the boundary is closed to fluid flow. The top and bottom model boundaries are set as closed boundary conditions.

Before the cyclic operation, an initial fill with air is required to build a gas reservoir. A gas reservoir with a radius of about 500 m (Fig. 3.1) is thus developed with five cycles in 2 years, which are 100 days of injection using a rate of 9.62 kg/s, 100 days of shut-

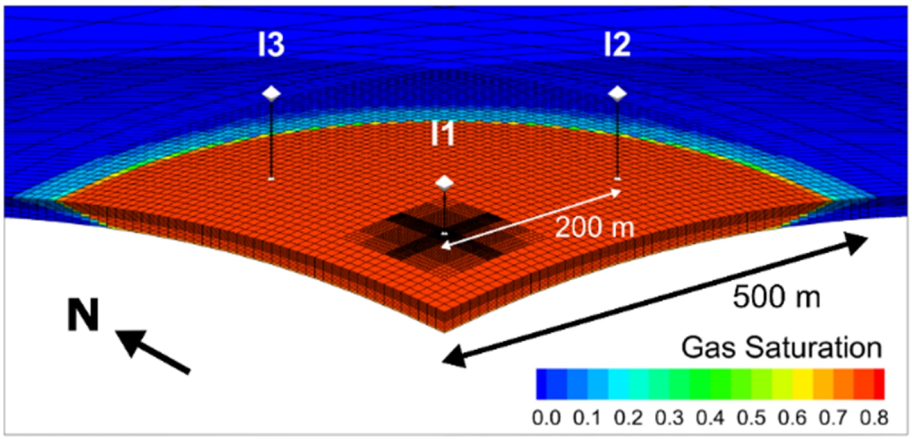

Figure 3.1 Side view of gas phase distribution after a 2-year initial fill in one quarter of the storage formation and the spatial distribution of three wells with a minimum distance of 200 m.

in, 4 times 35 days of injection using a rate of 16.98 kg/s, 3 times 70 days shut-in in between and 181 days shut-in after the 5th injection. The shut-in periods in between are designed to allow the redistribution of air driven by buoyancy in the reservoir. The initially filled gas reservoir thus has a gas-water contact at 800 m depth and in total 2.88×10^8 kg air in place with a maximum gas saturation of 0.8. Vaporization of water into the gas phase is not considered. Based on this initial condition, the cyclic operation is simulated for 10 years, corresponding to about 7300 cycles.

3.3 Feasibility study

This work investigates the CAES feasibility by assessing whether the porous formation is able to deliver the required air mass flow rate during storage operation in terms of reservoir behaviors. For CAES operation using a porous formation as the storage reservoir, the chosen storage formation must ensure the required air flow deliverability and at the same time maintain the pressure response within the given pressure thresholds of fracture pressure and operation pressure required (The HYDROdynamics Group LCC 2011; Schulte et al. 2012). Regarding the developed CAES scenario presented in chapter 2, the bottom hole pressure (BHP) at gas wells during storage operation thus needs to be validated for two pressure thresholds, i.e. the maximum safe pressure of 108 bar and the minimum required pressure of 47 bar while delivering the given air mass flow rate of 417 kg/s.

The BHP profile of well I1 simulated for the 2-year initial fill and the 10-year cyclic operation is shown in Fig. 3.2. At the bottom of gas wells I2 and I3 show similar pressure responses to well I1 (difference in pressure is less than one bar), and thus not shown here. Initially, the pressure at the bottom of well I1 is 71 bar, i.e. the hydrostatic pressure, and increases to 101 bar after the first stage of air injection. The pressure drops when the well shut-in phase starts, and reaches 80 bar after the first shut-in period. The well shut-in phase prevents the pressure build-up from exceeding the maximum safe pressure, and also allows the injected air to rise towards the top of the anticline by the buoyance effect. The BHP of well I1 reaches 104 bar at its maximum after the second stage of the initial fill but not the fifth one. This is because more air is injected in the storage reservoir and the pressure build-up is thus lower due to gas compressibility. At the end of the initial fill, the BHP drops to 86 bar again.

During the cyclic operation, the average pressure at well bottom (Fig. 3.2 red dashed line) drops from 82 bar to 77 bar after 10 years. This pressure dissipation is because of the extended boundary conditions assumed in the simulation by extending the model area. The BHP of well I1 fluctuates around this average pressure and its responses are lower than the maximum safe operation pressure and higher than the minimum required BHP. The lowest observed BHP during extraction is 60 bar, which is above the 47 bar required by the turbine, and during injection the BHP reaches up to 102 bar maximally, which is below the 108 bar assumed for fracture pressure. The injection and extraction air mass rates specified thus can be supported by the storage formation if twelve wells are used. For the developed CAES scenario, this indicates that the porous formation simulated can support the cyclic operation of the Huntorf gas turbine, and can sustain a

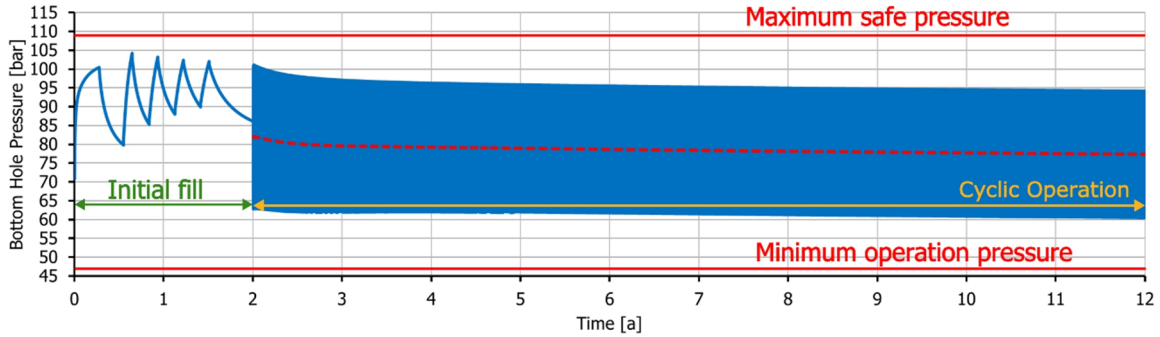

Figure 3.2 BHP profile of well I1 during 2-year initial fill and 10-year daily cyclic operation. Red dashed line shows the average pressure.

continuous power output of 321 MW for 6 h at an extraction air mass flow rate of 417 kg/s for 10 years. This corresponds to an energy output per day of 3,852 MWh, and the total is 14,060 GWh for 10 years.

Simulations show that the average pressure at well bottom decreases over time regardless of cyclic operation, and thus may drop to the initial reservoir pressure eventually depending on the formation boundaries. The air extraction during one storage cycle may lead to a decrease of BHP lower than the specified minimum operation pressure. Considering this during storage operation, the reservoir model is initialized with a pressure of 71.95 bar at 720 m depth and a gas–water contact at 800 m depth. This initialization represents a vertically equilibrated gas phase in the reservoir after years of the storage operation, and the lower limit for the average reservoir pressure during the storage operation. Based on this initial condition, the cyclic operation of the developed CAES scenario is simulated. To account for the on-going pressure dissipation, the total injection air mass flow rate is set to 430 kg/s.

The BHP of well I1 during cyclic operation for seven days is shown in Fig. 3.3. The BHP of well I1 fluctuates around the initialized pressure and its responses are lower than the maximum safe operation pressure and higher than the minimum required BHP. The lowest observed BHP during extraction is 51 bar, which is still above the required 47 bar by the turbine, and during injection the BHP reaches only up to 89 bar maximally, which is well below the 108 bar assumed for fracture pressure. The injection and extraction rates specified

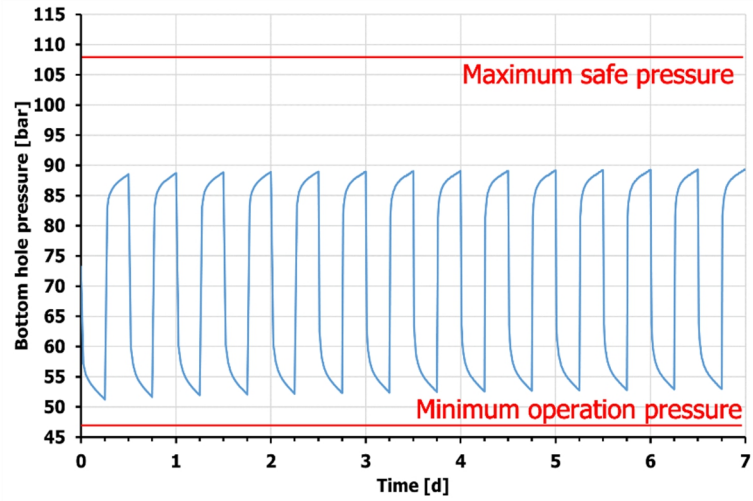

Figure 3.3 BHP profile of well I1 during daily cyclic operation under the initial reservoir pressure.

thus can be supported by the formation, even the lower limit of the average reservoir pressure is used. Together with the BHP responses shown in Fig. 3.2 for the 2-year initial fill and the 10-year cyclic operation, the storage formation is technically feasible for the CAES operation to sustain a continuous power output of 321 MW for 6 h at an extraction air mass flow rate of 417 kg/s.

3.4 Storage rates and storage capacity

According to the power output estimation of CAES gas turbines described in section 2.1.2, the storage rates and the storage capacity of CAES highly depends on the extracted air mass flow rate and the pressure of extracted air. Thus, in this study, a dimensioning of storage rates and storage capacity for the CAES scenario is performed through the airflow deliverability analysis on the used storage formation to quantify the potential energy outputs. The numerical model used is described in section 3.2, but is initialized with a reservoir pressure of 71.95 bar at 720 m depth and a gas–water contact at 800 m depth. This is to represent the lower limit for the average reservoir pressure during the storage operation, which actually reduces storage deliverability, as some elevated formation pressure would allow for higher extraction rates. Thus, the storage rates and the storage capacity of the CAES scenario is given as the lowest estimate.

Without refilling the air, the compressed air is continuously extracted from the gas reservoir by maintaining the extraction air mass flow rate, i.e. gas production rate (GPR), of 417 kg/s, and the well BHP of 47 bar. After 9.6 hours, the extraction air mass flow rate of the wells starts to decrease and the power output drops (Fig. 3.4 green and red lines). This shows that the reservoir can continuously produce 321 MW power for up to 9.6 hours, delivering a total air mass of 1.44×10^7 kg corresponding to about 5.0 % of the initial air mass. In total, the produced electrical energy is 3082 MWh, which is the storage capacity of this CAES facility without refilling the air. After 9.6 hours, the extractable air mass flow rate decreases continuously and correspondingly the power output decreases as well.

According to the operational experiences of the Huntorf power plant (Hoffeins and Mohmeyer 1986), in some working days, the CAES facility needs to start up and reach its full capacity within half an hour due to unexpected failures in the electrical grid. These situations are typical now, as the intermittent energy production from renewable resources leads to the increase of load balancing requirements. Therefore, the storage capacity of the CAES scenario is also estimated and given for potential maximal power output in short time periods, e.g. in half an hour.

In numerical simulations, an estimation of the maximum possible instantaneous power output is performed by only maintaining the well BHP (Fig. 3.4 blue line) and thus allowing higher flow rates at the wells. This corresponds to the case where a maximum of air is extracted at each point in time and thus instantaneous power is high. In the first 30 minutes, the average maximum extraction air mass flow rate of the twelve wells is 630 kg/s, corresponding to 484 MW power using the Huntorf gas turbine. The achievable air mass flow rate (Fig. 3.4, blue line) is dropping continuously with time, as air is extracted from the closer vicinity of the wells, and therefore also the

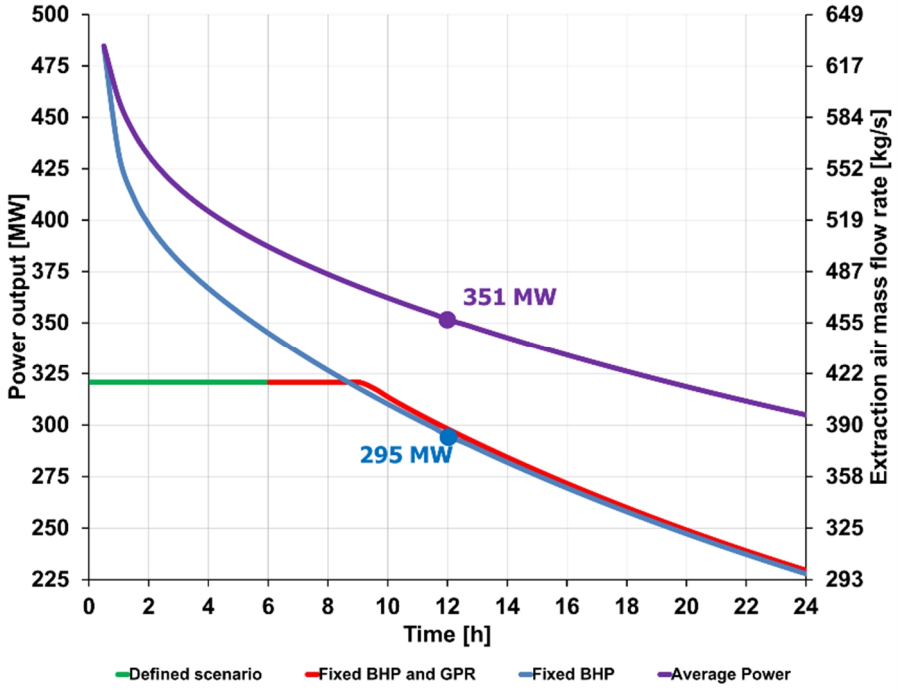

Figure 3.4 Extraction air mass flow rate (right axis) and power output (left axis) for: continuous power output as the designed scenario ('Defined scenario': green line), continuous power output by fixing BHP and extraction air mass flow rate ('Fixed BHP and GPR': green and red lines), instantaneous power output by fixing BHP ('Fixed BHP': blue line), and average power output calculated based on the instantaneous power output ('Average power': purple line).

instantaneous power output is decreasing. Based on the instantaneous power, the possible average power output over time is calculated (Fig. 3.4 purple line). It shows, for instance, that after 12 hours the actual instantaneous power is 295 MW at an air mass flow rate of 383 kg/s, while the average power output achieved, i.e. the average output of the 12 hours, is 351 MW.

Results of the instantaneous power output show that at 8.6 hours the power production is 321 MW. However, according to the continuous power production, the reservoir can produce the same amount of power up to 9.6 hours. This difference is due to the fact that the reservoir is operated at lower extraction rates in case of a continuous output and the corresponding power can be obtained for longer periods. Thus, the blue line in Fig. 3.4 allows for a conservative estimate of the production rates, the corresponding power achieved and the time periods over which the power is provided, so that other shorter operation cycles can be designed using this line as well. This provides flexibility in power output as well as power delivery times, both required for an electricity production dominated by fluctuating renewable energy.

3.5 Sensitivity analysis

Sensitivity analysis offers the opportunity to investigate feasibility and dimension the storage capacity as well as the storage rates considering the uncertainties in CAES operations. Here, the properties of the storage formation, i.e. permeability and porosity, and the configuration of gas wells are varied. This is because the permeability of the storage formation strongly affects the deliverability and thus the power output of an underground CAES storage. The investment of drilling wells is very

Table 3.2 List of the varied permeabilities and porosities in sensitivity analysis.

Parameter	Storage Formation													
Permeability [mD]	10	100	200	300	400	500	600	700	800	900	1000	1500	2000	2500
Porosity [-]	0.15	0.25	0.25	0.30	0.30	0.30	0.30	0.30	0.35	0.35	0.35	0.40	0.40	0.40

expensive, so it is interesting to investigate the well configuration required for different reservoir conditions and thus design a cost-effective plant.

3.5.1 The number of vertical wells

To improve the deliverability of a low-permeability formation, one of the approaches is to increase the number of wells used for injecting and extracting the compressed air. The average permeability of the storage formation is varied from 10 mD to 2500 mD, and the corresponding porosity varied from 0.15 to 0.40 (See Table 3.2). The ranges of permeability and porosity used here are referring to the on-site data of the Rhaetian formation from the North German Basin from Hese (2011, 2012) and the statistical study from Dethlefsen et al. (2014). As there is no correlation between permeability and porosity reported in this work, an increase of porosity with permeability is assumed, covering the porosity values reported.

To find out the number of vertical wells required for the varied permeabilities and porosities, the full storage formation in the anticline (see section 2.2) is simulated since the positioning of wells cannot be symmetrically arranged for all the well numbers investigated here. The storage formation is discretized into 120 × 120 × 25 cells, with a finer horizontal discretization of 10 m around the wells and a coarser discretization of 1000 m at the model boundary. The vertical discretization is gradually coarsened with finer cells of 0.5 m thickness at the top and coarser cells of 1 m thickness at the bottom. Initially, the pressure distribution is hydrostatic with 71.95 bar at 720 m depth (Fig. 3.5a), and the gas-water contact is set to 800 m (Fig. 3.5b) representing a vertically equilibrated gas phase in the reservoir. With a minimum distance of 200 m between each pair of wells, a total of 21 wells can be placed within that 500 m radius gas reservoir, and the spatial well set up is shown in Fig. 3.5. All the wells are fully screened wells in the storage formation.

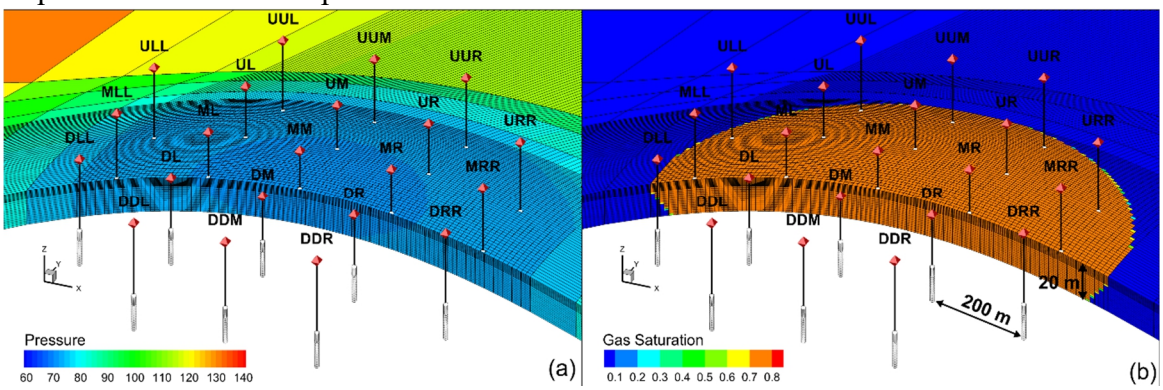

Figure 3.5 Side view of an initial pressure distribution (a) and gas phase distribution (b) in the gas reservoir for analyzing the number of wells required (using a vertical exaggeration of ×4). The spatial distribution of 21 wells within a minimum distance of 200 m is shown.

For different permeabilities of the storage formation, the number of vertical wells needed to support the required flow rate of 417 kg/s for 6 hours is shown in Fig. 3.6. When the permeability is less than 300 mD, even using 21 wells, the storage formation cannot support the required air mass flow rate of 417 kg/s for 6 hours, i.e. the CAES facility cannot produce 321 MW power for 6 hours. With increasing permeability, fewer wells are required to achieve the specified flow rate. A minimum of three wells is always required, even for a high permeability of 2500 mD. As can be seen in Fig. 3.6, the number of wells required to support the required flow rate does not linearly decrease with increasing permeability of storage formation. This is due to well interference at longer extraction times, and causes higher well numbers compared to the case of no well interference.

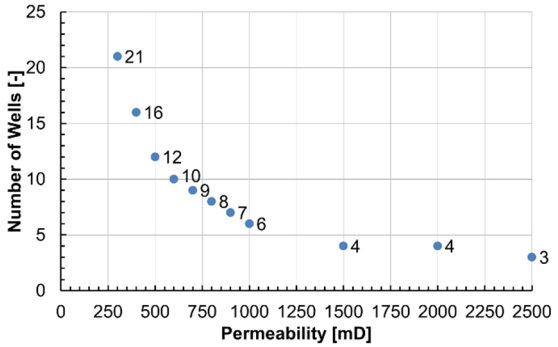

Figure 3.6 Number of vertical wells required to support the CAES operation vs. permeabity of the storage formation.

Additionally, a study on estimating the power output is performed if different numbers of wells are used, and the efficiency of power output is investigated by only using more wells. The hours for a continuous power output of 321 MW (Fig. 3.7a) and the maximum power output for the first 30 minutes (Fig. 3.7b) are both analyzed at a permeability of 1000 mD in the storage formation. Both results show a linear increase with increasing number of wells. A minimum of six wells is required to provide 321 MW for 6 hours at a permeability of 1000 mD. If 13 wells are used, the designed CAES plant produces 321 MW power for up to 40 hours, corresponding to an electric energy production of 12840 MWh, and for the first 30 minutes, it produces maximally 991 MW power. It is found that by using one additional well the storage formation at a permeability of 1000 mD can continuously produce 321 MW power for 4.8 hours longer, i.e. the storage capacity is increased by 1541 MWh correspondingly, and the

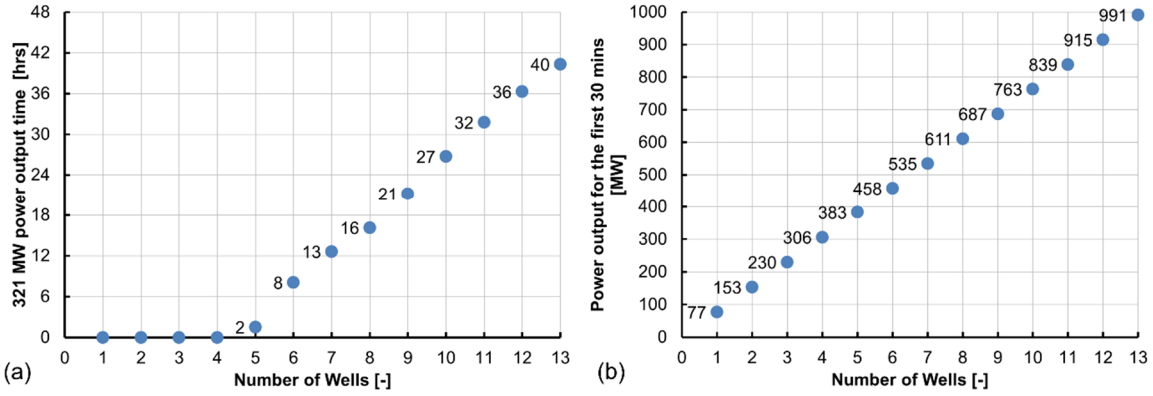

Figure 3.7 Hours of continuous power output (a) and the maximum power output for the first 30 mins (b) provided for different numbers of wells used (at a permeability of 1000 mD).

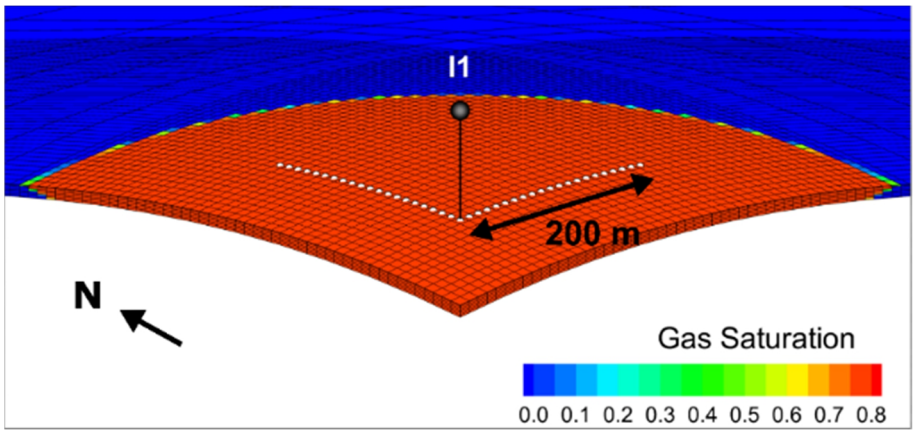

Figure 3.8 Side view of the spatial distribution of two horizontal wells with a screen length of 200 m at the middle depth of the storage formation.

maximum power output for the first 30 minutes is increased by 76 MW.

3.5.2 Using horizontal wells

Horizontal wells can be applied to improve the deliverability of a low-permeability formation because the screen length of horizontal wells can be hundred meters long allowing for a higher air mass flow rate. Thus, an estimation of the possible power outputs is given for the developed CAES scenario if four or eight horizontal wells are used at different permeabilities in the storage formation.

Considering that four or eight horizontal wells can be symmetrically placed in the storage site, only a quarter of the anticline is simulated. If eight horizontal wells are used, two horizontal wells with a screen length of 200 m are placed in this quarter of the gas reservoir in the middle grid layer with a thickness of 1 m (Fig. 3.8). The model domain is thus 8 km × 8 km × 20 m, and is discretized into 72 × 72 × 15 cells. A finer horizontal discretization of 10 m is used around the wells and a coarser discretization of 500 m at the model boundary. Vertical discretization uses cells of 1 m thickness at the top and coarser cells of 2 m thickness at the bottom. Initially, the pressure distribution is set to 71.95 bar at 720 m depth, and the gas-water contact is set to 800 m representing a vertically equilibrated gas phase in the reservoir.

The hours for a continuous power output of 321 MW (Fig. 3.9a) and the maximum power output for the first 30 minutes (Fig. 3.9b) are estimated for the storage formation at permeabilities up to 1000 mD of (see Table 3.2). Simulation results show that using horizontal wells can increase the power output, especially for low-permeability reservoirs. At a permeability of 300 mD in the storage formation, 21 vertical wells cannot produce 321 MW even for the first 30 mins. However, if four horizontal wells are used, the designed CAES plant can produce 321 MW power for up to 13.6 hours, corresponding to an electric energy production of 4.4 GWh, and for eight horizontal wells, the electric energy production is increased to 12.1 GWh. The storage capacity of this CAES plant is thus increased by 7.7 GWh if four more horizontal wells are used, i.e. roughly 1.9 GWh per horizontal well correspondingly. At a permeability of 1000 mD, using one more horizontal well, the storage capacity is increased by about 1.2 GWh. This non-linear increase in energy production with increasing permeability is due to well interference for

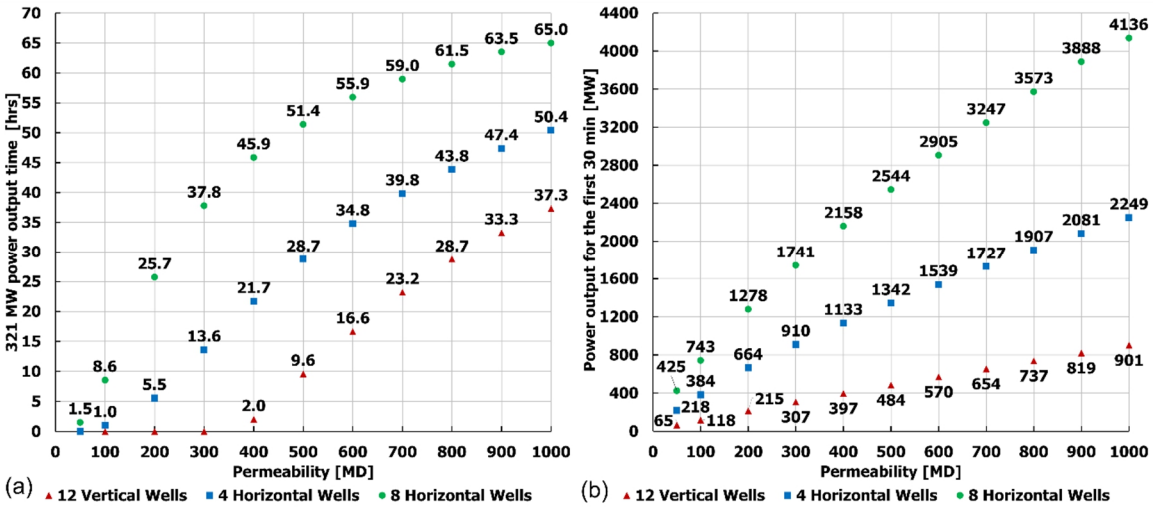

Figure 3.9 Hours of continuous power output (a) and the maximum power output for the first 30 mins (b) provided for different well configurations and permeabilities of the storage formation.

longer withdrawal. For the first 30 minutes, using four horizontal wells, this CAES plant produces maximally 910 MW power, and for eight horizontal wells maximally 1.7 GW power at a permeability of 300 mD in the storage formation. For a permeability of 1000 mD, this number increases to 2.2 GW and 4.3 GW correspondingly. The instantaneous power output for the first 30 mins shows a linear increase with increasing number of wells, which is roughly 200 MW per horizontal well at a permeability of 300 mD and 525 MW at a permeability of 1000 mD.

3.6 Discussion

Using the Huntorf power plant as a reference, the two salt caverns provide a total volume of roughly 3.1 × 10^5 m^3 and 321 MW power for up to 3 hours (Crotogino et al. 2001). The corresponding storage capacity is 963 MWh and the energy density is about 3.1 kWh/m^3. As shown in Fig. 3.7a, a porous formation with a permeability of 1000 mD may provide 321 MW for up to 8 hours using six wells and a total volume of air in place of about 4.2 × 10^6 m^3. The corresponding storage capacity is 2568 MWh and the energy density is about 0.6 kWh/m^3. If 13 wells are used, the energy density can reach about 3.1 kWh/ m^3 and the formation has a much higher capacity of 12840 MWh. If eight horizontal wells are used (see Fig. 3.9a), the energy density can reach about 5.0 kWh/ m^3 even higher than the Huntorf power plant. So while CAES in salt caverns is scalable by increasing the number of caverns, porous media CAES is scalable by increasing the well number or using horizontal wells.

In difference to salt caverns, the hydraulic permeability of porous formations represents an inherent limitation on the achievable air flow rates (Kushnir et al. 2012a). The sensitivity analysis based on the average permeability performed in this thesis provides a first step towards estimating the number of wells needed and designing a cost-effective CAES facility. There are additional factors which influence reservoir performance, such as the anticline closure radius, well screen length and distances, permeability distribution, and residual water saturation.

The closure radius of the anticline must be at least as large as the radius of the required air volume (Succar and Williams 2008). In

the scenario using in this work, the initial air volume is present within a radius of approximately 500 m, which is about 1/6 of the anticline closure radius. This large closure radius would thus allow to increase the stored air volume, which increases the storage capacity as well as the rates, if also more wells are used. With a smaller closure radius but the same vertical drop, the dip angle of the anticline will increase. This will reduce the effect of gravity override during injection, help gas to aggregate at the anticline top and therefore enhance extraction rates due to higher gas saturations near wells.

Because of the variable thickness in storage formations, the well screen length, i.e., the open-hole section, needs to be adjusted to avoid water coning (Wiles and Mccann 1981). The shorter the well screen length, the higher the pressure response while maintaining a required gas flow rate. When pressure is limiting, therefore only lower flow rates can be achieved. The larger the well distance, the less interference occurs, so that higher air flow rates can be applied. However, with increasing well distance, also less wells can be placed within the gas reservoir, which lowers the total extraction rate from the storage site.

Permeability will also vary spatially around the average value used in the sensitivity analysis in horizontal and vertical directions because of formation heterogeneity. This will likely lower the deliverability and thus increase the number of wells required to achieve a target rate, with the well number depending strongly on the type of local permeability and porosity heterogeneity. For real storage applications, well deliverability tests and history matching are applied to determine the required well number (The HYDROdynamics Group LCC 2011). The residual water saturation is assumed constant at 0.2 in the sensitivity analysis. A larger residual water saturation will reduce the air volume in the pore space, and thus the available amount of air accessible to each well during injection or extraction. This may limit the time a continuous gas extraction rate can be upheld to provide a continuous power output, especially for low permeability formations. According to the well deliverability curves in the Pittsfield test (ANR Storage Company 1990) for vertical wells, the air flow rates of wells will decrease if turbulent flow close to wells is encountered. This non-Darcy behavior can lower the maximum power output within the first 30 minutes due to a high extraction flow rate, however is not considered in this thesis.

Apart from the reservoir performance analysis, induced impacts can be considered for assessing this energy storage option (Bauer et al. 2013), such as thermal and geochemical impacts. The current operating CAES facilities at Huntorf and McIntosh operate as diabatic storages, which loses heat during compression of the air and regain this heat by burning natural gas with the compressed air during expansion. The thermal energy from the compression is not stored. According to the design of the Huntorf power plant (Crotogino et al. 2001), the temperature of the injected air at the well head after the compressor is cooled to the ambient temperature of the rock salt cavern. At the well bottom hole, the air temperatures may increase by a few Kelvin due to the slight pressure increase along the well. The local geothermal gradient determines the ambient temperature of the reservoir formation and thus the temperature to which the air would be

cooled. During air extraction, the compressed air with the ambient temperature of the geological formation will expand along the well. This temperature decrease however is small compared to the temperature decrease caused by the expansion of the gas in the turbine. A higher geothermal gradient would thus be beneficial, as air does not have to be cooled so much and less natural gas is required during air expansion in the turbine. Injecting air at higher temperatures would thus also be beneficial, but the mechanical integrity of the host rock would have to be proven. Storing the compression heat for heating the expanding gas is an idea of adiabatic CAES, which is currently at the research stage (RWE Power 2010). The main problem here is the high heating rates required. An analysis of air temperature change in the storage formation will be given in chapter 4 assuming that the temperature of the injected air is the same as the average temperature in the storage reservoir.

Injection of oxygen as a component of air into geological formations long free of oxygen may cause geochemical reactions. As an analogy, injection of CO_2 for CO_2-storage (CCS) with about 4% of O_2 as an impurity may lead to mineral oxidation if redox-sensitive minerals or ferrous iron-bearing minerals are present in the storage formation. This is especially so in the case of pyrite (Lu et al. 2014; André et al. 2015). Pyrite oxidation increases the dissolution of carbonates, as these buffer the H^+ from pyrite dissolution, typically leading to gypsum precipitates. This reaction was found to stop once the oxygen is consumed. During operation of CAES, oxygen is injected into the storage formation with each injection cycle, which could result in a lower pH of the storage formation water and thus a higher risk of wellbore corrosion, as well as reduced oxygen contents in the outflowing air. Precipitates like ferrous sulphate or gypsum in the storage formation might reduce porosity and thus also permeability and well deliverability (Succar and Williams 2008). However, research by Huminicki and Rimstidt (2009) and Berta et al. (2016) show that if enough carbonates are present in the mineral phases or dissolved in the fluid phase, the pH of the formation water will remain at neutral levels. Ferric ion containing hydroxide was found to precipitate mainly on the pyrite mineral surfaces and therefore forms a coating which strongly limits further pyrite oxidation and thus oxygen consumption. These geochemical impacts thus depend on the chemical composition of the storage formation and the formation water, but can be experimentally assessed using site-specific data. A quantitative evaluation of possible induced geochemical impacts is given in chapter 4.

In the Huntorf power plant, due to the high pressure reduction rates (up to 15 bar/h), the stability of the surrounding salt and the volume losses have been monitored during its life period (Crotogino et al. 2001). The corrosion of production strings has been discovered in the Huntorf power plant because of the humidity in air. In porous formation CAES, the same risks should be considered, as well as potential brine movement or uprising induced by large-scale pressure built-up due to the initial fill (see e.g. Delfs et al. (2016)). The production string can have a higher risk of corrosion due to the presence of residual water and the possible acid production due to mineral oxidation. While for a salt cavern the spatial position is exactly known, the

spatial position of the gas phase for a porous formation CAES is not directly known. However, geophysical monitoring techniques like seismic, geoelectric and gravimetric measurements might be employed to monitor the extension of the gas phase (Benisch et al. 2015; al Hagrey et al. 2016; Pfeiffer et al. 2016a; Köhn et al. 2016).

3.7 Summary

A realistic scenario of large-scale CAES operation using a porous formation as storage site is numerically simulated within a typical geologic anticline structure in the North German Basin. The numerical simulations are performed using ECLISPE reservoir simulator for a 2-year initial air filling and a 10-year cyclic operation.

During the storage operation, the pressure fluctuation at the bottom of gas wells is found to be within the system thresholds, thus supporting the specified air injection and extraction rates of 417 kg/s, and the minimum inlet pressure of the gas turbine of 43 bar. Using the initial hydrostatic pressure to represent the lower limit of the average reservoir pressure, the BHP of gas wells also fluctuates within the system thresholds. This shows that, in terms of reservoir behaviors during storage operation, it is technically feasible to operate the designed CAES facility on a daily basis. Using twelve vertical gas wells, 321 MW of power can be produced for 6 h, corresponding to an energy production of 1926 MWh. With two withdrawn periods of 6 h in the early morning and in the late afternoon, this CAES produces an energy of 3852 MWh per day and 14060 GWh for 10 years.

For the designed CAES scenario, the analysis of the storage capacity and the storage rates show that the reservoir can continuously support up to 9.6 hours of 321 MW power production before reaching the minimum operating pressure, thereby extracting about 5.0 % of the total air in the reservoir. The storage capacity of this CAES plant is thus 3082 MWh as electrical energy output. Furthermore, for the first 30 minutes, the maximum achievable extraction air mass rate of the storage formation is higher at 630 kg/s, corresponding to 484 MW power. Instantaneous power output is dropping from 484 MW to 295 MW within the first 12 hours.

The number of vertical wells required is estimated accounting for different permeabilities of the storage formation. When the permeability is less than 300 mD, the storage formation is not able to deliver the specified extraction air mass flow rate for 6 hours, even when 21 vertical wells are used. A minimum of three vertical wells is always required even for a permeability of 2500 mD, and well interference has to be considered. For each additional vertical well, the storage formation at a permeability of 1000 mD can continuously produce 4.8 hours longer the required power of 321 MW, while for the first 30 minutes, the maximum power output is increased by 76 MW. This sensitivity analysis shows that the well number required to reach the target storage capacity is strongly affected by the formation permeability, with low permeability requiring higher well numbers. However, due to well interference, this relationship is non-linear and depends on the detailed geometric set-up of the wells in the porous formation.

Using horizontal wells can increase the potential power output of this CAES plant especially for low-permeability reservoirs, because horizontal wells have much longer

well screen length compared to vertical wells allowing for higher air extraction rates. At a permeability of 300 mD, if eight horizontal wells are used, this CAES facility can produce 321 MW power for up to 37.8 hours, corresponding to an electric energy production of 12.1 GWh. For the first 30 minutes, this CAES plant produces maximally 1.7 GW electric power using eight horizontal wells.

The analysis on continuous power output and instantaneous power output presents a methodology of estimating the storage rates and the storage capacity for CAES in porous formations. Combining with the analysis of well configurations required at different permeabilities allows a first design of such a CAES storage site in a permeable porous formation to be made.

4 Induced Impacts

Using a typical anticline in the North German Basin, the operation of a hypothetical large-scale compressed air energy storage (CAES) facility is proven to be technically feasible in terms of reservoir behavior. Operating CAES in the porous storage formation also induces secondary hydraulic, thermal and geochemical impacts, and a quantification of these effects is given in this chapter. The hydraulic and thermal impacts induced by the storage operation are presented as the change of the pressure and the temperature in the storage formation in section 4.1 and section 4.2, respectively. With a prior developed consistent geochemical system of the storage formation, the induced geochemical reactions are assessed in section 4.3 for the impacts on the stored air, the storage formation, and the storage operation.

Parts of this chapter are published as
Wang, B., & Bauer, S. (2017). Pressure response of large-scale compressed air energy storage in porous formations. Energy Procedia, 125, 588–595. doi:10.1016/j.egypro.2017.08.205.
Parts of this chapter are submitted to Applied Geochemistry as
Wang, B., & Bauer, S. (2018). Induced geochemical reactions by compressed air energy storage in a porous formation in the North German Basin.

4.1 Hydraulic impacts

4.1.1 Introduction

Compressed air energy storage (CAES) is comparable to natural gas storage or carbon dioxide capture and storage, which are well studied for their hydraulic process from decades of experience in the oil and gas industry. Storing gases in a porous formation can cause pressure changes in gas wells and in the storage formations as well. The study of pressure changes is useful to identify the potential risks of running gas storages in porous formations, such as potential brine movement or uprising by pressure build-up due to the gas injection (e.g. see Delfs et al. 2016). Besides, the investigation of large-scale reservoir pressure changes provide the first ideas for where and when the geomechanical changes may happen and also for the setup of geophysical monitoring (Rutqvist 2012). The monitoring of pressure changes also helps for determining the extension of the gas phase, which defines the impact area of potential induced geochemical changes.

A synthetic but representative geological anticline site in the North German Basin is used to store compressed air for a large-scale CAES operation scenario (see chapter 2). In this anticline, the pore space of the storage formation is initially saturated with saline water, and thus an initial fill with air is performed to create a gas reservoir and allow for CAES cyclic operation. During the initial fill, the injected air pressure needs to be higher than the hydrostatic pressure in the storage formation to displace the water. This higher air pressure thus leads to a pressure build-up observed at the bottom of gas wells (see chapter 3 Fig. 3.2). Studies from CO_2 injection and natural gas storages

indicate that the elevated pressure is highest at gas wells, propagates away from gas wells towards the formation boundaries, and results in a pressure increase throughout the storage formation (Bary et al. 2002; Leetaru et al. 2009; Zhou and Birkholzer 2011; Benisch and Bauer 2013; Cihan et al. 2013). This induced hydraulic changes are also expected by the initial fill of air.

During the storage operation, the compressed air is cycled within the created gas reservoir. The air injection at gas wells thus leads to air compression in the storage reservoir and pressure build-up, but the air extraction causes air expansion resulting in a pressure decrease. Since the CAES in this scenario is designed to balance short diurnal fluctuations in energy production, the cyclic amount of air is much smaller compared to the air in the storage reservoir injected by initial fill. Because of this, the induced pressure responses during cyclic operation may be only within the gas reservoir referring to the study by Oldenburg and Pan (2013a), who uses a porous formation CAES with a single well to produce half of the power as Huntorf power plant. The investigated CAES scenario here, however, has a larger storage capacity, which produces the same power as the Huntorf power plant but for a longer extraction period of 6 hours. Twelve vertical wells are used and stronger pressure responses at gas wells and in the storage reservoir are expected due to the effects of well interference. A quantification of induced hydraulic impacts is given as follows in terms of the pressure responses observed in the storage formation during the 2-year initial fill and the 10-year cyclic operation.

4.1.2 Pressure response

To quantify the induced hydraulic impacts as pressure responses during the CAES operation, numerical simulations are performed using the oil and gas reservoir simulator ECLIPSE 300 in compositional mode (Schlumberger 2016). The setup of numerical simulations has been described in section 3.2 for investigating the feasibility of the developed CAES scenario.

The observed spatial pressure responses in the storage formation are shown in Fig. 4.1 at four times during the 12-year storage operation, which are after the 2nd stage (Fig. 4.1a) and at the end (Fig. 4.1b) of the initial fill, and at the last extraction (Fig. 4.1c) and injection (Fig. 4.1d) of cyclic operation. During the initial fill, a pressure response of more than one bar can be observed throughout the whole model domain, i.e. at distances larger than 8 km from the center of the storage (see Fig. 4.1a and 4.1b). In comparison, a pressure response of more than one bar induced by the cyclic operation is only observed in the gas phase, i.e. within a radius of about 500 m (see Fig. 4.1c and 4.1d).

The profiles of pressure response are shown at different distances from well I1 (Fig. 4.2). In the storage formation, the maximum pressure build-up is about 33 bar observed at a distance of one meter from the well I1 after the 2nd stage of initial fill, and the maximum pressure drop reaches about 11 bar after the last air extraction at 12 years. At a distance of 10 km from the well I1 in the storage formation, the pressure increases to a maximum of about 3 bar at 2.7 years due to the initial fill of air, and continuously drops because of the

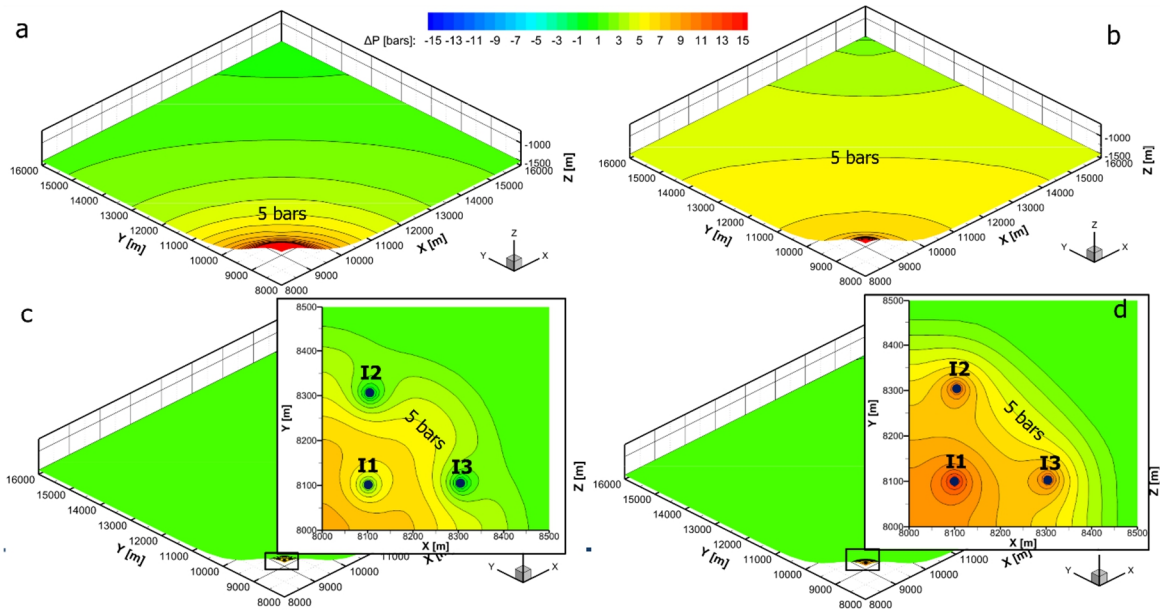

Figure 4.1 Pressure response in the storage formation at four times during 12-year operation time: (a) after the 2nd stage of initial fill; (b) at the end of the initial fill; (c) after the last extraction of the cyclic operation; (d) after the last injection of the cyclic operation.

extended boundary conditions. The cyclic behavior in pressure response can be observed within a distance of 400 m from the well I1, which is roughly at the edge of the gas reservoir. This is because the air is highly compressible, which dampens the pressure response. Besides, the mass of cycled air is about 9.0×10^6 kg, which is about 3.1 % of the total mass of air in place. This helps to stabilize the distribution of the gas phase and reduce the energy loss by avoiding the movement of the gas-water contact.

4.1.3 Discussion

For large-scale CAES in porous formations, the impacts of induced pressure changes laterally are due to the initial fill of air and also strongly depend on the lateral boundary conditions assigned. When considering mutual pressure inferences of multiple storage sites, pressure superposition occurs and pressure responses will thus add up. The current set-up assumes closed hydraulic boundary conditions at 20 km distance. This can represent impermeable barriers or the end of the formation, but could also be interpreted to represent a periodic siting of identical CAES storage sites every 40 km.

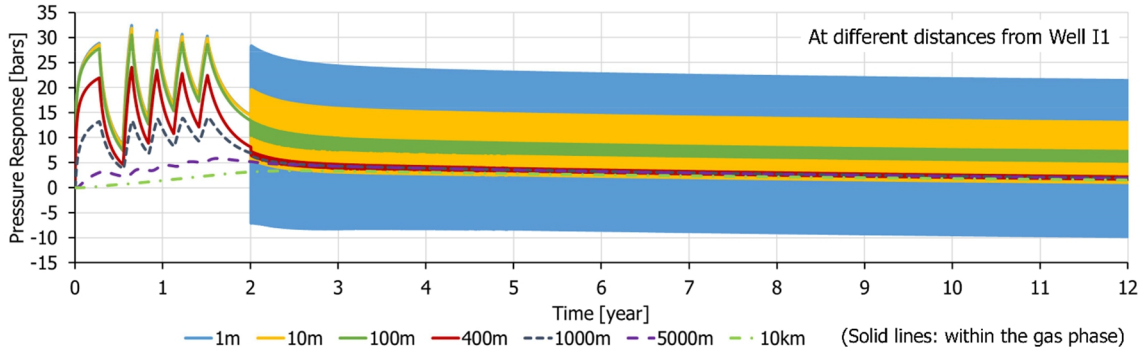

Figure 4.2 Pressure response in the storage formation at different distances from well I1.

For the current set-up, no significant pressure inference was found to limit the storage operation. The spacing could be reduced by assuming closed boundary conditions closer to the storage site. This would lead to a higher pressure level in the storage formation after the initial fill. As the pressure cannot dissipate either, it would actually increase the performance of the daily operation.

4.2 Thermal impacts

4.2.1 Introduction

According to the design of Huntorf power plant (Hoffeins 1994), the air temperature after the compressor train is cooled down to the temperature close to the average temperature of the salt cavern. The same design for the temperature of the injected air is assumed here for the developed large-scale CAES operation scenario in a typical anticline in the North German Basin, which is thus close to the average temperature of the gas reservoir. Studies by Oldenburg and Pan (2013a) and Guo et al. (2016) show that, under this assumption, the induced temperature change in the storage formation is minor by only a few Kelvins, and spatially limited to regions very near to the well. However, in their studies, the air is assumed as an ideal gas and the Joule-Thomson effect is thus not considered. The Joule-Thomson effect, or the Joule-Thomson process, quantifies the temperature change of a real gas due to the change in pressure driving flow assuming that no heat is exchanged with the environment (Joule and Thomson 1854).

Pressure responses of this CAES operation (see Fig. 4.2) show that, the air injected by gas wells expands and flows from a high pressure region, i.e. near gas wells, towards a low pressure region, i.e. the edge of the storage reservoir. During the air extraction, the stored air also expands from the reservoir edge towards the gas wells. Both expansion processes are driven by pressure changes which can result in a decrease of air temperature due to the Joule-Thomson effect. A quantification of induced thermal impacts is given as follows in terms of temperature change in the storage formation during the 2-year initial fill and the 10-year cyclic operation.

4.2.2 Simulation setup

The numerical simulations are performed using the oil and gas reservoir simulator ECLIPSE 300 with the “Thermal” option (Schlumberger 2016), in which the compressed air is considered as a single and non-condensable component. The air density is determined based on the molar volume of air, which is a function of air pressure and temperature. The air viscosity is explicitly given as a table depending on temperature after Kadoya et al. (1985). The thermal properties of air listed in Table 4.1 refers to the average temperature and pressure of the storage reservoir, i.e. 34 °C and 80 bar. The formation water is assumed to have a salinity of ~ 70 kg/m^3.

For quantifying induced temperature changes, the storage formation of the geological anticline as well as the cap rock and bottom rock layer, i.e. overburden and underburden layers, are simulated. The storage formation represents a homogeneous sandstone reservoir of 20 m thickness with a high-permeability of 500 mD. The cap rock and bottom layer have a thickness of 30 m, but additionally extended by 130 m and 150 m, respectively. This is because, preliminary simulation results show that the induced temperature changes by cyclic operations can be

Table 4.1 The thermal parameters of air and water (Kadoya et al. 1985; Mottaghy et al. 2010; Stober and Bucher 2012; Kaye and Laby 2016).

Parameter	Air	Water
Specific heat capacity [J/kg/K]	1134	3993
Thermal conductivity [W/m/K]	0.03	0.60
Joule-Thompson coefficient [K/Pa]	0.16×10^{-5}	-

observed beyond the thickness of the cap rock and bottom layer. The corresponding parameters of the geological anticline are listed in Table 2.2. The capillary pressure-saturation function of the reservoir is determined by the Brooks and Corey (1964) correlation. With a higher entry pressure of 20 bar given for the overburden layers and a very low permeability of 1.0×10^{-5} mD, these layers are impermeable for gas uprising.

Due to the symmetry of the structure and well configuration shown in Fig. 2.7, only a quarter of the anticline is simulated, in which three vertical fully penetrating wells are placed with a minimum distance of 200 m in between (see Fig. 3.1). The total injection and extraction air mass flow rates of 417 kg/s are distributed to the twelve wells, i.e. 34.75 kg/s each well. The model domain is thus 8 km × 8 km × 360 m, and is discretized into 72 × 72 × 35 cells. A finer horizontal discretization of 10 m is used around the wells and a coarser discretization of 500 m at the model boundary. Vertical discretization uses cells of 1 m thickness at the top and coarser cells of 2 m thickness at the bottom. Close to well I1, the grid is locally refined again (horizontally from 0.5 m to 5 m; vertically from to 1 m to 10 m) to capture the temperature changes near the gas well I1 (see Fig. 3.1).

The pressure and temperature at the surface condition are assumed to be 15.56 °C and 1.01 bar, respectively. The initial pressure distribution is hydrostatic with 71.95 bar at 720 m depth, and the initial geothermal gradient is 25 K/km. The enthalpy of the injected air is assumed to be 34 °C at a pressure of 72 bar, which is close to the average temperature and pressure of the gas reservoir. A threshold pressure of 47 bar is set to each well bottom hole during extraction to ensure the minimum gas turbine inlet pressure. Additionally, to avoid possible induced fractures in the reservoir rock during injection (e.g. see Benisch and Bauer (2013); Mitiku and Bauer (2013)), a maximum pressure of 150 % of the initial hydrostatic pressure at each well bottom hole, i.e. of 108 bar, is applied.

As the aquifer of the storage formation is laterally not closed, extended hydraulic boundary conditions are assigned at the model boundaries, by considering an additional lateral extension of the storage formation by 12 km in each direction, which allows for brine (with a salinity of 2.69 mol/kg (Mitiku and Bauer 2013)) outflow and pressure relief. This boundary condition is included by changing the pore volume of the outermost model cells, which represents this additional volume. At 20 km from the center of the storage, the boundary is closed to fluid flow. The top and bottom model boundaries are set as closed boundary conditions.

Before the cyclic operation, an initial fill with air is required to build a gas reservoir. A gas reservoir with a radius of about 500 m (Fig. 3.1) is thus developed with five cycles in 2 years (see section 2.3.1), which are 100 days of injection using a rate of 9.62 kg/s, 100 days of shut-in, 4 times

35 days of injection using a rate of 16.98 kg/s, 3 times 70 days shut-in in between and 181 days shut-in after the 5th injection. The shut-in periods in between are designed to allow the redistribution of air driven by buoyancy in the reservoir. The initially filled gas reservoir thus has a gas-water contact at 800 m depth and in total 2.88×10^8 kg air in place with a maximum gas saturation of 0.8. Vaporization of water into the gas phase is not considered. Based on this initial condition, the cyclic operation is simulated for 10 years, corresponding to about 7,300 cycles.

4.2.3 Temperature change

Temperature at the bottom of gas well

The temperature profile at the bottom of well I1 for the 2-year initial fill and the 10-year cyclic operation is shown in Fig. 4.3. At the bottom of gas wells I2 and I3 show similar temperature changes to well I1 (difference in temperature is less than one Kelvin), and thus not shown here. Initially, the temperature at the bottom of well I1 is 33.5 °C referring to a pressure of 71 bar, and increases to 38.7 °C after the first stage of the initial fill due to the pressure build-up (see Fig. 3.2). The temperature reaches 39.0 °C at its maximum after the second stage of the initial fill when the BHP is also at its maximum. At the end of the initial fill, the temperature is found to be 35.6 °C at the well bottom. Slight oscillations are observed within the well shut-in phases because the redistribution of the injected air leads to a mixing in air temperature as well.

During the cyclic operation, the behavior of the temperature fluctuations at the well bottom follows the same pattern as the observed pressure responses. The average temperature drops from 35.5 °C to 34.5 °C over 10 years along with the pressure dissipation. The highest observed temperature is 38.9 °C at the first injection of the cyclic operation, and the lowest temperature is found to be 32.0 °C at the last extraction. The simulation results show that only a minor decrease of air temperature is found during the extraction. This temperature change is very small that the extracted air does not require more natural gas for heating up and thus it will not affect the energy production.

Temperature change in the geological anticline

A profile of temperature change at 30 m away from the well I1 is shown in Fig. 4.4. During the initial fill, the temperature change at this location is found to be less than 1°C, and thus not strongly affected by the temperature of injected air (see Fig. 4.4a). In each cycle of the first 30-day operation (see Fig. 4.4b), a minor temperature decrease can be observed and

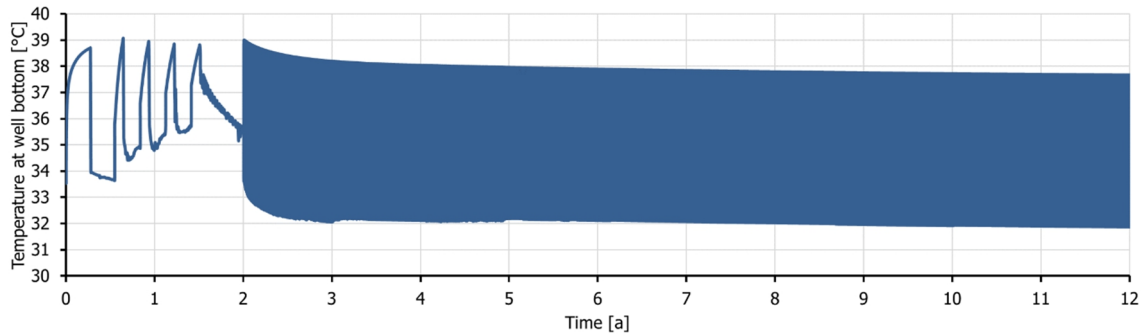

Figure 4.3 Temperature profile at the bottom of well I1 during 2-year initial fill and 10-year daily cyclic operation.

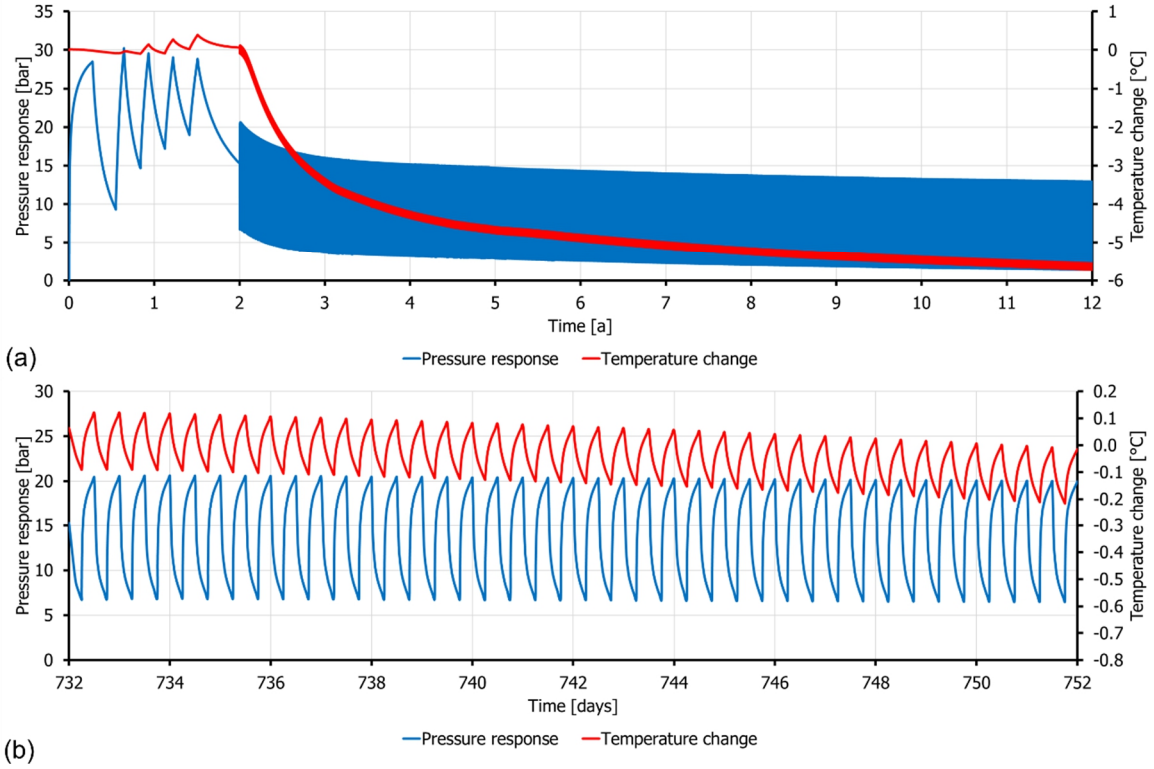

Figure 4.4 Pressure response and temperature change in the middle of the reservoir formation at a distance of 30 m from well I1. (a) for the 12-year storage operation; (b) for the first 30 days of cyclic operation.

this minor change accumulates over time resulting in a decrease of roughly 0.2 °C after 30 days. At the end of the cyclic operation after 10 years, a total temperature decrease of 5.8 °C is observed.

Simulation results show that the temperature changes along with the pressure response due to the Joule-Thomson effect. The temperature drops when the pressure decreases, and vice versa, the temperature also increases when the pressure increases. Since the average reservoir pressure decreases over time after the initial fill, a net pressure decrease between injection and extraction is found after each operation cycle. This minor pressure decrease thus leads to a minor temperature decrease as well and accumulating over time. Besides, away from gas wells, the increased temperature due to air injection at the wellbore dampens away with the transport of air (see Fig. 4.5d) and thus not affect the temperature at this location. Furthermore, air always expands regardless of injection or extraction away from gas wells, which can also lead to a cooling of air in the gas reservoir due to the Joule-Thomson effect.

The spatial temperature change of the storage formation is shown in Fig. 4.5 in the x-z plane at four times during the 12-year storage operation, which are after the 2nd stage (Fig. 4.5a) and at the end (Fig. 4.5b) of initial fill, and at the last extraction (Fig. 4.5c) and injection (Fig. 4.5d) of cyclic operation. After the 2nd stage of the initial fill, a temperature increase of 1 °C is observed at a distance of 15 m from well I1 in the storage reservoir, and its maximal increase is about 5.3 °C close to the wellbore. At the end of the initial fill, a temperature increase of 1 °C is observed at

a distance of 10 m above the reservoir formation because of heat diffusion, and in the reservoir formation at a distance of 20 m from well I1. After the last air injection of the 10-year cyclic operation, a temperature increase of 4 °C is observed due to air injection within a distance of 5 m from well I1. Further away from well I1, a cumulative

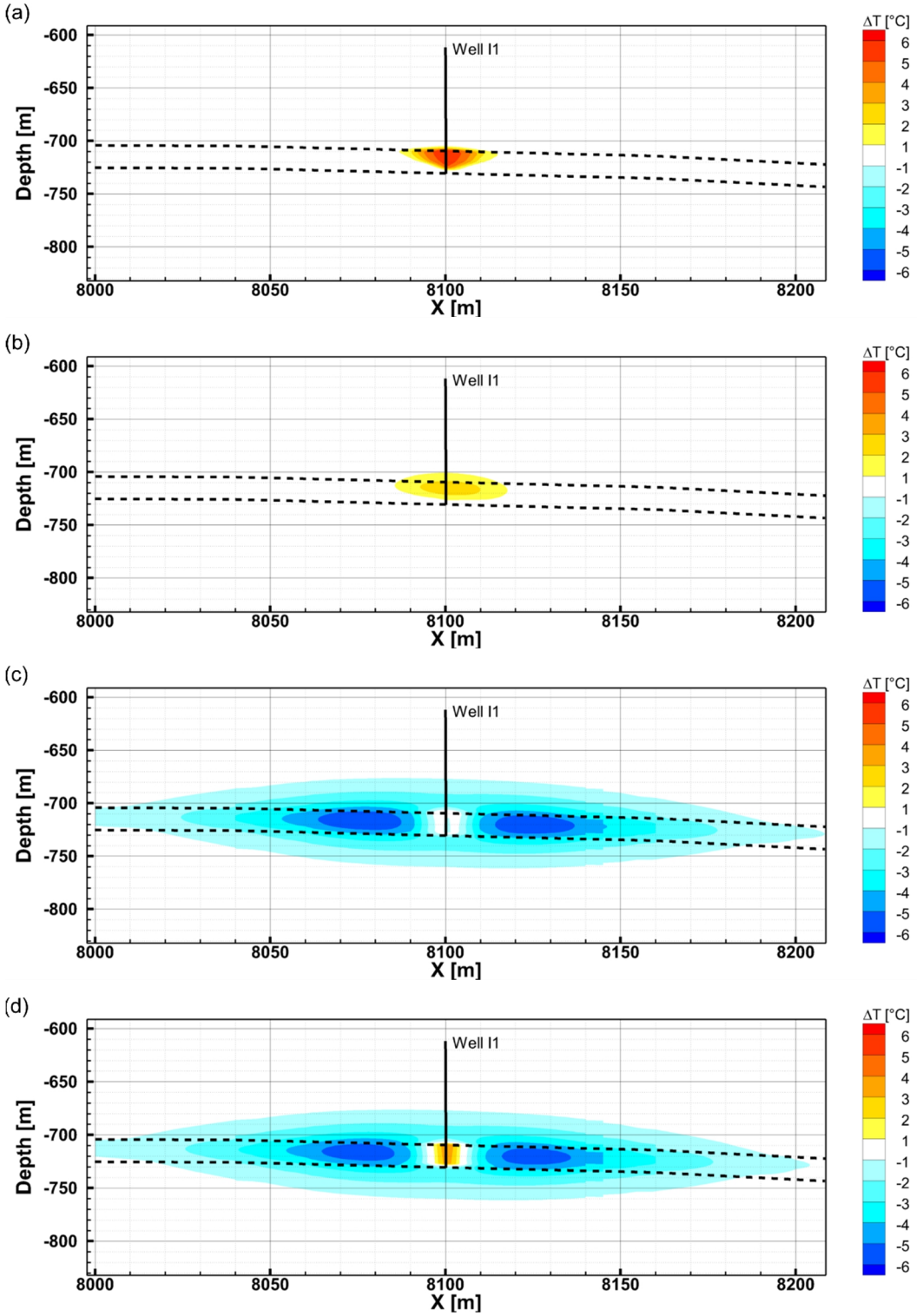

Figure 4.5 Temperature change near the gas well I1 in the x-z plane of the storage formation at four times during 12-year operation time: (a) after the 2nd stage of initial fill; (b) at the end of the initial fill; (c) after the last extraction of the cyclic operation; (d) after the last injection of the cyclic operation. The black dashed line indicates the reservoir formation.

temperature decrease of larger than 1 °C is found vertically at a distance of 40 m above and below the reservoir formation. Laterally, this temperature decrease of 1 °C is found at a distance of 100 m from well I1 in the reservoir formation. Near gas wells in the gas reservoir, a decrease of larger than 5 °C is observed at a distance of between 15 m to 40 m from well I1, and the maximum temperature decrease is about 5.8 °C.

Assuming that the injected air temperature is close to the average reservoir temperature, the induced thermal impacts during a large-scale CAES operation is thus found to be minor in terms of temperature change in the storage formation. During the initial fill, the temperature change can be observed only in the vicinity of gas wells, but after years of cyclic operation, a small temperature decrease of 1 °C can be found further away from gas wells in the storage formation.

4.2.4 Discussion

The induced thermal impacts in the storage formation assessed show a minor temperature change during and after the initial fill because the injected air temperature is assumed to be close the reservoir temperature. The injected air temperature largely depends on the surface installations, e.g. the configuration of gas compressor set, or the type of gas turbine used in CAES. In an adiabatic CAES, for example, the high-temperature air may be considered to be stored in underground porous formations for heat conservation. With a higher injected air temperature, the induced temperature change in the storage formation will thus be larger. This high temperature may lead to water vaporization and dehydrate the storage reservoir. The dehydration operation is also considered for diabatic CAES to prevent the depletion of oxygen from potentially induced geochemical reactions in the storage reservoir. However, the high temperature in the injected air may induce geomechanical changes on the reservoir rock due to thermal expansion and contraction, which can result in a permeability decrease and risks in reservoir integrity.

Because of the Joule Thomson effect, a cumulative temperature decrease in the storage reservoir is found during cyclic operation. The rates and times of air injection and extraction in one operation cycle is assumed identical as 417 kg/s and 6 h, respectively. Applying different operating schedules, e.g. a larger extraction rate compared to injection rate, or a longer extraction time, may lead to a larger pressure decrease and consequently also a larger temperature decrease. The CAES scenario assessed is operated as on-going air injection and extraction cycles for 10 years. Considering potential operation breaks, e.g. infrastructure maintenance, the observed minor temperature decrease can dissipate away to the surrounding formations. Besides, if the geothermal flux from the underburden formations and the natural heat generation from reservoir rocks are included in the numerical simulations, the induced temperature change will be even smaller.

4.3 Geochemical impacts

4.3.1 Introduction

The storage site used in the studied CAES scenario represents a typical geological anticline in the Rhaetian sandstone formation from the North German Basin. As the mineral composition of the Rhaetian sandstone shows the presence of pyrite (see

Table 2.3), operating CAES in this storage formations can induce pyrite oxidation, and thus the oxygen in the stored air can be partly or completely consumed (ANR Storage Company 1990). Without a refill of the storage reservoir, the reduced fraction of oxygen in the stored air may potentially cause a failure of a diabatic CAES facility, because the air extracted from the storage may not contain enough oxygen for the gas combustion process required to heat the expanding gas. Studies on acid mine drainage indicate that pyrite oxidation with on-going supply of oxygen, e.g. near gas wells for CAES operation, can lower the pH to very acidic conditions (INAP 2012; Nordstrom et al. 2015), which thus increases the risk of wellbore corrosion at the gas storage wells. Meanwhile, mineral precipitation induced by geochemical reactions may clog the pore space, thus reducing porosity and permeability of the storage formation, which would again lower the well deliverability and power output (Pei et al. 2015).

Due to these induced geochemical reactions and potential impacts, a reliable quantification of induced geochemical reactions is a prerequisite for assessing the feasibility of porous media CAES. This following section therefore focusses on investigating and quantifying potential induced geochemical impacts on the storage formation for the designed CAES operation scenario. The induced pyrite oxidation and other geochemical reactions are investigated under a consistent geochemical reaction system for the Rhaetian sandstone. The induced impacts on the stored air as well as the storage formation are also quantified using scenario analysis and process based kinetic batch modelling of such a geochemical system.

4.3.2 Geochemical scenarios

The scenario of a diabatic CAES operation presented in chapter 2 is used here, assuming the same gas turbine as in the Huntorf power plant. With a minimum inlet pressure of 43 bar, this gas turbine can produce 321 MW of electric power at an air mass flow rate of 417 kg/s and a natural gas mass flow rate of 11 kg/s (Hoffeins and Mohmeyer 1986; Hoffeins 1994; Kushnir et al. 2012b; E.ON SE 2016). The natural gas is required to heat the expanded air, which cools considerably in the turbine due to the Joule-Thompson effect. Instead of the two salt caverns used as air storage in the Huntorf power plant, a geometrically representative anticline in the Rhaetian formation from the Northern German Basin is assumed to provide a porous storage formation for the compressed air.

Before the cyclic operation, an initial fill with air is performed to create the gas reservoir in the anticline (see section 3.2), as the formation pore space is initially saturated with saline water. This initial fill can be operated with shut-in periods in between to minimize the buoyancy effect and obtain a well-mixed gas phase in the storage reservoir to provide the cushion gas required to support the high injection and extraction rates of such a CAES storage (The HYDROdynamics Group LCC 2005, 2011). During cyclic operations, when surplus power from renewable resources is available, the motor drives the compressor to compress air, which is then stored in the porous formation. During peak demand, the compressed air is retrieved through the wells from the porous formation. Along with natural gas it is burned in the gas turbine to drive the generator and produce electricity. In this work, the synthetic CAES facility is assumed to operate by a daily

cycle for 20 years with a 6-hour injection in the early morning and a 6-hour extraction in the late afternoon.

The storage reservoir is located in the main sandstone of the Rhaetian formation, which belongs to the Upper Keuper Subgroup (Exter Formation), i.e. the youngest part of the Triassic (Doornenbal and Stevenson 2010). The Rhaetian storage formation is in this study represented as a highly permeable sandstone with a permeability of 500 mD and a porosity of 0.35 (see Table 2.2) according to on-site data provided in Hese (2012, 2011) and the statistical study by Dethlefsen et al. (2014). The top of the storage reservoir is assumed to be located at a depth of 700 m, with a formation thickness of 20 m. The minerals in the Rhaetian sandstone considered here consist of carbonates, silicates, clay mineral K-mica, anhydrite and pyrite (see Table 2.3), as reported by Mitiku et al. (2013).

As the mineral composition of the Rhaetian sandstone shows the presence of pyrite (Mitiku et al. 2013; Dethlefsen et al. 2014), pyrite oxidation is the primary induced geochemical reaction resulting from oxygen dissolution into the formation water. Because the formation water has a high salinity with sodium chloride concentrations of more than some tens of kg/m^3, the activity of iron-oxidizing bacteria is strongly reduced (Shiers et al. 2005) and pyrite oxidation here is considered as an abiotic reaction. Without catalyzing iron-oxidizing bacteria, pyrite oxidation is very slow because the oxidation rate of ferrous iron by oxygen to ferric iron is limited at low pH conditions (Singer and Stumm 1970). At high pH conditions, the solubility of the ferric iron is generally low. Thus, dissolved oxygen is assumed to be the major oxidant for pyrite and the relevant chemical reaction for induced pyrite oxidation is (Lowson 1982; Taylor et al. 2009; Chandra and Gerson 2010):

$$FeS_2 + {}^{15}/_{4}\, O_{2(aq)} + {}^{1}/_{2}\, H_2O \rightarrow Fe^{3+} + 2SO_4^{2-} + H^+ \quad (4\text{-}1)$$

The designed operation of this hypothetical CAES facility in a porous formation has been proven to be feasible (see section 3.3) in terms of the required pressure at the gas turbine inlet and the corresponding air mass flow rate. Twelve wells are required to sustain the specified target rate of the CAES plant. Instead of simulating the entire CAES operation including initial fill and cyclic operation, the induced geochemical impacts on the stored air, the formation fluid and the mineral composition are addressed for the following “end-member” scenarios:

- For stored air injected and extracted within one storage cycle, geochemical changes are short term and assessed using a residence time of twelve hours.
- For stored air from the initial fill and air at the reservoir fringe, longer time scales with a residence time of up to 20 years are applied to assess geochemical changes.
- The potential change in the formation fluid and mineral composition within the gas reservoir is always long term for 20 years, however, near gas wells, it is expected to be driven by a constant supply of oxygen injecting as part of the stored air in each storage cycle.

4.3.3 Modeling approach

Software

The coupled multiphase-multicomponent ECLIPSE-OpenGeoSys-PHREEQC simulator (Pfeiffer et al. 2016b) is used to

quantify the induced geochemical reactions and the potential change in the stored air, the formation fluid and the mineral composition. This coupled simulator combines the multiphase-multicomponent reservoir simulator ECLIPSE (Schlumberger 2016) with the thermal-hydraulic-mechanical-chemical (THMC) process simulator OpenGeoSys (Kolditz and Bauer 2004; Kolditz et al. 2012), which is coupled to chemical reaction software packages, such as ChemApp (Beyer et al. 2012; Mitiku et al. 2013; Li et al. 2014) and PHREEQC (Xie et al. 2006; He et al. 2015). The following software is used for this purpose:

- PHREEQC (Parkhurst and Appelo 2013) is used to quantify equilibrium and kinetic chemical reactions between the formation fluid and the mineral phase, including mineral dissolution and precipitation.
- The ECLIPSE reservoir simulator is applied in the E300 compositional mode (Schlumberger 2016) to quantify multicomponent gas flow as well as the phase equilibrium between gas and the formation water.
- OpenGeoSys (OGS) adapts flow and transport parameters, such as porosity and permeability, due to changes in the mineral composition.

Reservoir batch model

A reservoir batch model with a constant volume is set up to quantify potential changes of the stored air composition for different residence times, as well as changes in the storage formation at the reservoir fringe. This batch model accounts for changes in stored air pressure and composition, by considering a constant volume of porous formation of 100 m^3. To quantify the change in the storage formation near gas wells, a constant air flow rate in the model accounting for the on-going supply of air from each storage cycle is included.

The depth of the reservoir batch model is at 710 m representing the average depth of the storage formation. The corresponding parameters are listed in Table 2.2 (Hese 2011, 2012; Dethlefsen et al. 2014), and the capillary pressure-saturation function of the reservoir is determined by a Brooks and Corey correlation (Brooks and Corey 1964). The water density is 1050 kg/m^3 representing a salinity of ~ 70 kg/m^3 at a depth of 710 m (Delfs et al. 2016). The reservoir batch model is initially equilibrated with the prior filled air at a hydrostatic pressure of 70.9 bar. Reservoir temperature is 33 °C, assuming a surface temperature 15 °C and a geothermal gradient of 25 K/km.

For investigating geochemical impacts, the air forming the cushion gas has a composition of 78.15 % N_2, 20.90 % O_2, 0.91 % Ar and 0.04 % CO_2. CO_2 is added compared to the simulation setup in the section 3.2 allowing for a build-up of CO_2 due to possible carbonate dissolutions. Air properties are calculated in E300 using a generalized form of the Peng-Robinson equations of state (Schlumberger 2016) and the compositional gas parameters listed in Table 4.2. The solubility of air components in the formation fluid are calculated by the methods described in the work from Mitiku et al. (2013a) and Li et al. (2018) accounting for the salinity of the formation fluid as well as reservoir temperature and pressure. Evaporation of residual water is not considered here, so that the residual water saturation remains constant during the simulation. The air in this batch model thus has a total volume of 27.36 m^3 and a weight

Table 4.2 The parameters of air components N_2,O_2, Ar and CO_2 (Lemmon et al. 2000; Kaye and Laby 2016).

Parameter	N_2	O_2	Ar	CO_2
Critical Temperature [K]	126.192	154.581	150.687	304.18
Critical Pressure [bar]	33.9	50.4	48.6	73.8
Critical Molar Volume[m^3/mol]	8.95×10^{-5}	7.34×10^{-5}	7.46×10^{-5}	9.19×10^{-5}
Acentric Factor	0.037	0.022	-0.002	0.224

of 2247 kg at a density of 82.11 kg/m^3. The air components are 592.43 mole/m^3 of O_2, 1.01 mole/m^3 of CO_2, 2215.64 mole/m^3 of N_2 and 26.01 mole/m^3 of Ar. For the case of on-going supply of air, an air volume flow rate of 0.016 m^3/s at reservoir conditions is applied to represent the air exchange during one storage cycle.

Geochemical batch model

Thermodynamic database

The thermodynamic database for PHREEQC geochemical calculations is based on the 6th released database from THEREDA (Altmaier et al. 2011), which uses the PITZER interaction model (Pitzer 1973) to account for activities in a high salinity condition and also includes aqueous species related to carbonate and silicate minerals. The corresponding parameters of PITZER interaction model for iron mineral related species, such as Fe^{2+}, Fe^{3+} and S^{2-}, are added based on the study by Cohen et al. (1987) and Moog and Hagemann (2004). The influence of pressure and temperature changes on solution species and mineral phases is not considered in the database. These effects are expected to be small due to limited temperature and pressure changes during a cyclic CAES storage operation.

Equilibrated geochemical system

The equilibrated geochemical system in the Rhaetian sandstone before air injection is set up in PHREEQC representing the initial condition for quantifying the induced geochemical reactions. The mineral composition in Table 2.3 represents a possible mineral assemblage for the Rhaetian sandstone according to the statistical study by Dethlefsen et al. (2014). The fluid composition (Table 4.3) shows measured values for the Rhaetian sandstone from an average depth of 1500 m. This composition is used here as reference data for the equilibration (Mitiku et al. 2013). The equilibration is achieved by a stepwise addition of minerals and by trying to find an equilibrium in each step by adjusting the concentration of solution species (Spaar 2016). In this tedious approach, firstly carbonates, followed by anhydrite and silicates and finally pyrite are adjusted.

The equilibrated fluid chemistry thus obtained is listed in Table 4.3 and shows a pH of 6.96, indicating a pH-neutral environment. The salinity of the formation fluid at 710 m depth is about 70 kg/m^3 instead of the 147 kg/m^3 at 1500 m, due to the lower solubility of NaCl at the lower pressure and temperature conditions given for the reduced storage formation depth assumed here. Therefore, the equilibrated concentrations of Na^+ and Cl^- are adjusted explicitly to represent the lower solubility and are thus lower than in the reference data set. The equilibrated concentration of SO_4^{2-} is one order of magnitude higher, because anhydrite is considered as a primary mineral instead of gypsum, and its solubility is larger at the formation temperature of 33 °C (Klimchouk 1996). The lower concentration of Fe^{2+} here is determined by the solubility

Table 4.3 The fluid chemistry of the Rhaetian sandstone formation: reference data and equilibrated results.

Species	Reference Concentration (Mitiku et al. 2013) [mol/m^3_{liquid}]	Equilibrated Concentration [mol/m^3_{liquid}]
Al^{3+}	Not measured	1.67×10^{-5}
CO_3^{2-}	Not measured	6.04×10^{-1}
Ca^{2+}	6.83×10^{1}	1.38×10^{2}
Cl-	2.69×10^{3}	$1.56 \times 10^{3*}$
Fe^{2+}	3.00×10^{-1}	1.37×10^{-4}
K^{+}	6.80	4.72
Mg^{2+}	3.21×10^{1}	7.65×10^{1}
Na^{+}	2.51×10^{3}	$1.20 \times 10^{3*}$
SO_4^{2-}	9.40	3.63×10^{1}
Si^{4+}	Not measured	1.07×10^{-1}
pH [-]	Not measured	6.96

* Concentration is adjusted explicitly considering the salinity of formation fluid at the reservoir condition.

of pyrite which is low at the lower pressure and temperature conditions at reduced depth. Equilibrated concentrations of all other solution species are also influenced by the chosen mineral assemblage for the Rhaetian sandstone. The differences to the measured data are within one order of magnitude, which is attributable to uncertainties in data sampling and is within the range of the spatial variation (Dethlefsen et al. 2014). The equilibrated concentrations of solution species is thus acceptable and considered as one representative example of the fluid chemistry in the storage formation.

Primary and secondary minerals

Minerals used for equilibrating the geochemical system of the Rhaetian sandstone formation are considered as primary minerals. The secondary iron-related minerals resulting from pyrite oxidation are selected based on studies on acid mine drainage. Nordstrom (1982) stated that, at a pH larger than 3.5, insoluble ferric hydroxide ($Fe(OH)_3$) is precipitated due to hydrolysis (see Eq. (4-2)) when pyrite is oxidized by dissolved oxygen in water (see Eq. (4-1)). Insoluble ferric hydroxide is in an amorphous state and will continuously transform to other mineral forms, such as goethite, ferryhydrite, schwertmannite, hematite and jarosite. Among these minerals, hematite is formed only under a dehydration process of ferric hydroxide at temperatures close to 100 °C (Cornell and Schwertmann 2003). This temperature is much higher than the temperature in the storage formation. According to Bigham et al. (1996), goethite is the most stable mineral phase over the pH range 2 to 6 compared to schwertmannite and ferryhydrite and the corresponding reaction is shown in Eq. (4-3). Work from Bigham et al. (1996) and Zolotov and Shock (2005) show that in a strong acid solution with a low pH (e.g. $pH < 2$) and rich in sulfate and ferric ions, the ferric hydroxyl sulfate mineral jarosite, here represented by potassium jarosite ($KFe_3(OH)_6(SO_4)_2$), may precipitate, as shown in Eq. (4-4) (Cornell and Schwertmann 2003). For the secondary iron-related minerals, therefore, goethite is considered as representing the minerals containing oxidized ferric iron at all pH conditions, and jarosite for the minerals buffering the solution with a high

concentration of H^+ and SO_4^{2-} at a pH of lower than 2.0.

$$Fe^{3+} + 3H_2O \rightarrow Fe(OH)_{3(a)} + 3H^+ \quad (4\text{-}2)$$

$$Fe(OH)_{3(a)} \rightarrow FeOOH_{(goethite)} + H_2O \quad (4\text{-}3)$$

$$K^+ + 3Fe(OH)_{3(a)} + 2{SO_4}^{2-} + 3H^+ \rightarrow KFe_3(OH)_6\,(SO_4)_{2(jarosite)} + 3H_2O \quad (4\text{-}4)$$

Pyrite oxidation produces acid, i.e. the hydrogen ion H^+ (see Eq. (4-1)). The H^+ can react with the carbonates calcite and dolomite in the Rhaetian sandstone formation and induce carbonate dissolution (Appelo and Postma 2005) (see Eq. (4-5) and Eq. (4-6)). Concentrations of Ca^{2+} and SO_4^{2-} in solution will increase and precipitation of anhydrite is expected. The clay mineral kaolinite ($Al_2Si_2O_5(OH)_4$) is chosen as the secondary mineral for mineral precipitation when the solution has a high concentration of Al^{3+}, following the study by Mitiku et al. (2013a).

$$CaCO_{3(calcite)} + 2H^+ \rightarrow Ca^{2+} + H_2O + CO_2 \quad (4\text{-}5)$$

$$CaMg(CO_3)_{2(dolomite)} + 4H^+ \rightarrow Ca^{2+} + Mg^{2+} + 2H_2O + 2CO_2 \quad (4\text{-}6)$$

According to Palandri and Kharaka (2004), the dissolution rate constant of silicates and clay minerals is often very slow and roughly six orders of magnitude lower than the rate for carbonates, anhydrite and pyrite. For quantifying the potential change in stored air with the constant volume batch model, preliminary model runs show that including silicates and clay minerals has no significant impact on the simulated results. Therefore, the dissolution of silicates and clay minerals is neglected. However, as preliminary model results near gas wells show that the pH of the formation fluid may drop below 1.0, precipitation of jarosite and dissolution of the silicate mineral K-feldspar and the clay mineral K-mica for balancing potassium concentration may occur. Therefore, these reactions and minerals have to be considered when quantifying the changes near a gas well.

Reaction kinetics

The equations on geochemical reaction kinetics are explained in section 2.6.3. Except pyrite and jarosite, the specific rate constant k together with the function $g(c)$, i.e. the term $k \cdot g(c)$, for all primary and secondary minerals are formulated according to Palandri and Kharaka (2004). The relevant data for all minerals are listed in Table 4.4.

The well-established rate law from Williamson and Rimstidt (1994) written as Eq. (4-7) is applied here for quantifying the rate of pyrite oxidation. It is valid for aqueous pyrite oxidation by dissolved O_2 referring to Eq. (4-1).

$$k \cdot g(c) = k_{WR} = 10^{-8.19} \times {m_{DO}^{0.5}}\Big/{m_{H^+}^{0.11}} \quad (4\text{-}7)$$

where m_{DO} [mol] is the mole of dissolved oxygen and m_{H^+} [mol] the mole of hydrogen ions.

For jarosite, a specific rate constant of 1.00×10^{-10} mol/m²/s as given by Brookfield et al. (2006) is applied for the term $k \times g(c)$. Additionally, a condition of pH < 2.0 is added in the formulation of the rate law as an indicator allowing the precipitation of jarosite for a solution rich of H^+ and SO_4^{2-}.

Table 4.4 Kinetic rate parameters for primary and secondary minerals.

Parameter	A_{react} [m^2/g]	Kinetic rate parameters (Palandri and Kharaka 2004; Brookfield et al. 2006)							
		Neutral mechanism		Acid mechanism			Base mechanism		
		k_{25} [$mol/m^2/s$]	E_a[kJ/mol]	k_{25} [$mol/m^2/s$]	E_a[kJ/mol]	n(H^+)	k_{25} [$mol/m^2/s$]	E_a[kJ/mol]	n(H^+)
Primary Minerals									
Anhydrite	1.01×10^{-3}	6.46×10^{-4}	14.3						
Calcite	1.11×10^{-3}	1.55×10^{-6}	23.5	5.01×10^{-1}	14.4	1.0	3.31×10^{-4}	35.4	1.0*
Dolomite	1.06×10^{-3}	2.95×10^{-8}	52.2	6.46×10^{-4}	36.1	0.5	1.13×10^{-3}		
Quartz	1.13×10^{-3}	1.02×10^{-14}	87.7						
Albite	1.15×10^{-3}	2.75×10^{-13}	69.8	6.92×10^{-11}	65.0	0.46	2.51×10^{-16}	71.0	-0.57
K-Feldspar	1.17×10^{-3}	3.89×10^{-13}	38.0	8.71×10^{-11}	51.7	0.5	6.31×10^{-22}	94.1	-0.82
K-Mica	1.02×10^{-2}	1.00×10^{-13}	22.0						
Pyrite	5.99×10^{-4}	**Rate law from Williamson and Rimstidt (1994) (Eq. (4-7))**							
Secondary minerals									
Goethite	7.89×10^{-2}	1.15×10^{-8}	86.5						
Jarosite	9.80×10^{-2}	1.00×10^{-10}							
Kaolinite	1.15	6.92×10^{-14}	22.2	4.90×10^{-12}	65.9	0.78	8.91×10^{-18}	17.9	-0.47

* Reaction order n with respect to partial pressure of CO_2.

Table 4.5 Change in components O_2 and CO_2 within one storage cycle of 12 hours at reservoir pressures of 71.0 bar and 106.5 bar.

Air Pressure	Time	O_2	CO_2	ΔO_2		ΔCO_2	
[bar]	[hour]	[mol]	[mol]	[mol]	[%]	[mol]	[%]
71.0	**0**	16209.64	27.88	-4.91	-0.03	4.60	16.48
	12	16204.73	32.48				
106.5	**0**	24333.60	43.25	-5.75	-0.02	5.55	12.82
	12	24327.85	48.80				

Following an approach by Klein et al. (2013), Cantucci et al. (2009) and Gaus et al. (2005), the average grain diameter for non-clay minerals is set to 2×10^{-5} m and for clay minerals to 2×10^{-6} m. White and Peterson (1990) showed that the true geometric surface area in laboratory experiments often exceeds the value evaluated based on the above equation due to the roughness on the mineral surface. A roughness factor of 10 is thus used here to quantify this effect, as shown in the studies by Zerai et al. (2006), Zhang et al. (2009) and Xu et al. (2010). However, compared to laboratory experiments, mineral dissolution and precipitation rates may be lower due to smaller reactive surface areas in natural environments (Beckingham et al. 2016). The α factor in Eq. (2-12) is thus applied to account for this possible reduced reactivity. Typical values range from 10^{-1} to 10^{-3} (Gaus et al. 2005; Klein et al. 2013; Bourg et al. 2015; Beckingham et al. 2016). This wide range shows the uncertainty in estimating mineral reactive surface areas, which is accounted for by varying this parameter within the given bounds. In this study, a factor of 10^{-3} is applied for primary minerals following the study by Klein et al. (2013), Gaus et al. (2005), Zhang et al. (2009) and Xu et al. (2010). For secondary minerals, the factor of 10^{-1} is used assuming a very large contact surface area with the fluids. Besides, a very small amount of about 1×10^{-8} moles is initially given in the model for secondary minerals as a 'seed' concentration to allow for precipitation. This results in an initial surface area of 1×10^{-6} (m^2/m^3_{rock}), similar to the work by Mitiku et al. (2013a) and Zhang et al. (2009). The calculated reactive surface areas for primary and secondary minerals are listed in Table 4.4.

4.3.4 Short- and long-term change in the stored air pressure and composition

The kinetic batch model using the concept of constant volume was applied to investigate the short- and long-term changes of stored air pressure and air composition due to induced geochemical reactions. As one storage cycle consists of six hours of air injection and six hours of air extraction, air has a residence time of 12 hours in the gas reservoir. Two different reservoir pressures were used, with 71 bar representing the average pressure during one storage cycle and 106.5 bar representing the highest occurring pressure and thus the case of highest O_2 solubility.

Results are reported in Table 4.5 and show that at a pressure of 71 bar, 4.91 moles of O_2 in the injected air is used to oxidize pyrite and the produced H^+ reacts with carbonates resulting in a production of 4.60 moles of CO_2. The difference in oxygen is due to precipitation of the mineral

goethite. This corresponds to a relative reduction of 0.03 % for oxygen and a relative increase of 16.48 % for CO_2, respectively. At the higher pressure of 106.5 bar, the absolute changes are larger due to the higher amount of dissolved O_2, however the relative changes are even smaller with 0.02 % and 12.82 %, respectively.

For a diabatic CAES, the oxygen loss in the stored air can affect the flammability of the gas mixture of extracted air and the added natural gas. According to Zabetakis (1964), at a pressure of 43 bar, which is the inlet pressure of the Huntorf gas turbine, the minimum oxygen concentration (MOC) required for flame propagation in a gas mixture of natural gas, nitrogen and oxygen is approximately 9.5 %, both in volume or moles. Therefore the change in O_2 during one cycle will not affect the flammability of the stored air mixed with the natural gas.

To investigate long-term changes in the stored air, the kinetic batch model was run for a simulation time of 20 years assuming a reservoir pressure of 71 bar. The resulting changes in air pressure and air composition are shown in Fig. 4.6. After one year, air pressure drops to 69.9 bar due to removal of oxygen. The corresponding air composition is 17.80 % O_2, 2.16 % CO_2, 79.11 % N_2 and 0.93 % Ar. The oxygen mole fraction drops below MOC at about 4.6 years (see Fig. 4.6b). After this time, the stored air cannot be used for burning natural gas. For even longer residence time, the air pressure drops further to 63.2 bar after about 14.5 years, and remains constant afterwards because all oxygen has reacted. The corresponding air composition is 12.59 % CO_2, 86.39 % N_2 and 1.01 % Ar. The air pressure decreases, because the gas density of CO_2 is higher than O_2. Furthermore, pyrite oxidation results in a decrease of one mole of O_2 in the gas phase, however, the mole increase of CO_2 due to carbonate dissolution is lower than one as goethite is precipitated. This represents a decrease in the total moles of the air components, which further reduces the air pressure and also causes an increase in N_2 and Ar mole fractions although the absolute moles of N_2 and Ar remain constant.

4.3.5 Change in the formation fluid and minerals within the gas reservoir

Air is brought to the edge of the gas reservoir during the initial fill, but is not

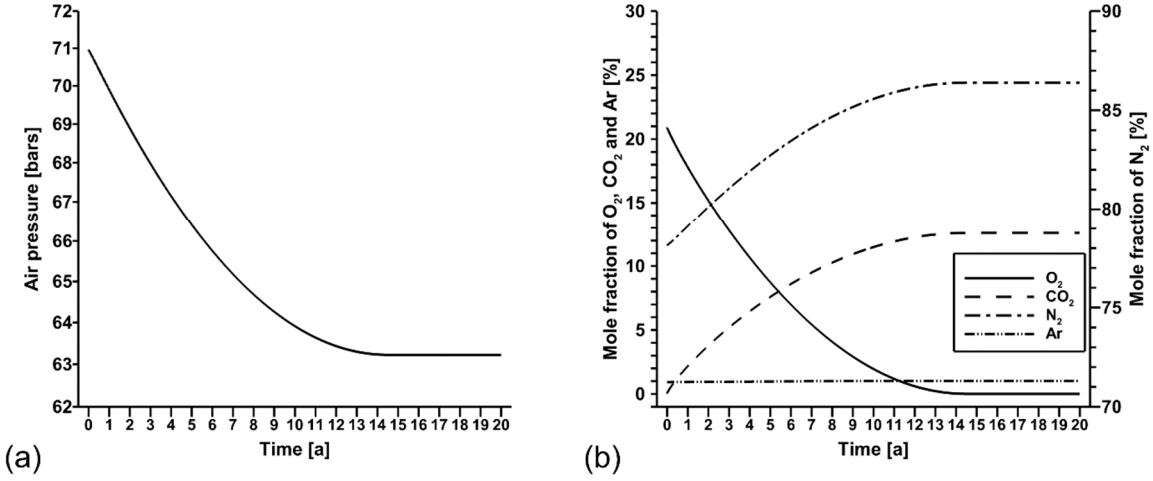

Figure 4.6 Change in the stored air without oxygen replenishment. (a) air pressure (b) air components.

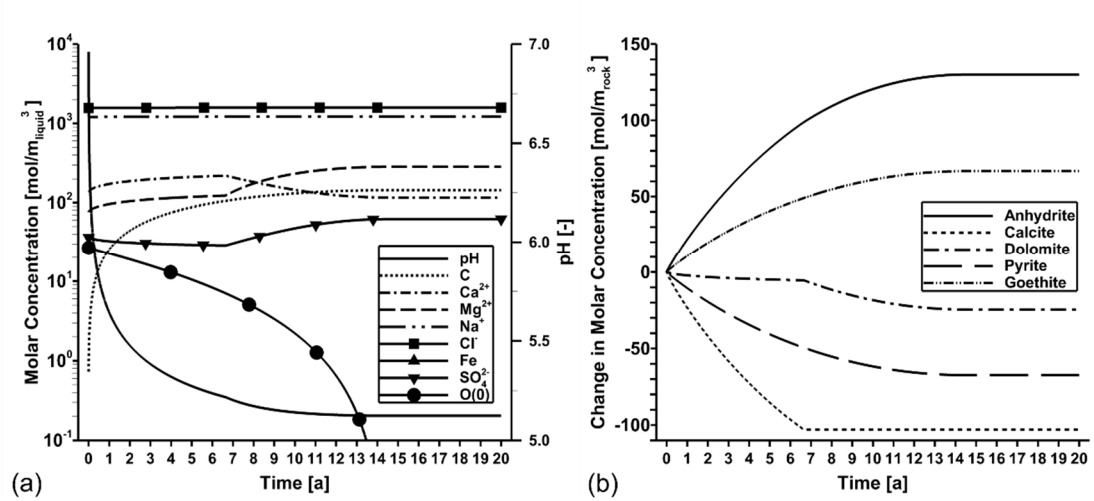

Figure 4.7 Geochemical composition of formation water and storage formation without oxygen replenishment. (a) pH and solution species of formation fluid (b) formation minerals.

replaced by the cyclic storage operation due to the long distance from the well. This causes a limited supply of oxygen, as oxygen is not replenished, and thus a different reactive behavior compared to the places near gas wells. The kinetic batch model with the concept of the constant volume is thus suitable to investigate the change in the formation fluid and minerals at the reservoir edge for a simulation time of 20 years. The pH of the formation fluid (see Fig. 4.7a) shows a fast decrease from the initial value of 6.96 to 5.48 within the first two years. Pyrite oxidation producing acid lowers the pH even with buffering by carbonate dissolution, because the produced CO_2 stays in the gas phase with an elevated partial pressure and thus has a higher solubility. After the O_2 in the stored air is completely consumed at about 14.5 years (see Fig. 4.7b), pH drops to 5.12 and remains constant afterwards. This demonstrates that pyrite oxidation can acidize the formation fluid, but pH will not drop further due to the limited supply of oxygen.

At a pH of 5.12 jarosite does not precipitate and thus jarosite, silicates and clay minerals are not considered in this case. Fig. 4.7a shows changes in solution species concentration of those species relevant to carbonates, anhydrite and iron minerals. The concentration of Ca^{2+} increases for about 7 years and decreases again afterwards. The increase results from the dissolution of calcite and dolomite (see Fig. 4.7b) due to the additional H^+ from pyrite oxidation. The enrichment of Ca^{2+} in the solution results in the precipitation of anhydrite which reduces the concentration of SO_4^{2-} at the same time. After the complete dissolution of calcite at about 7 years (see Fig. 4.7b), the precipitation of anhydrite causes a decrease of the concentration of Ca^{2+}. The anhydrite precipitation rate decreases due to a slower supply of Ca^{2+} from dolomite dissolution, which leads to an increase in SO_4^{2-} concentration. At the same time, the additional H^+ from pyrite oxidation can only react with dolomite, which shows as a faster increase of Mg^{2+} in the solution. The total concentration of Fe, i.e. the sum of Fe^{2+} and Fe^{3+}, is not observable in Fig. 4.7a because the small amount of Fe^{2+} in the initial solution is quickly oxidized by the dissolved O_2 and the Fe^{3+} from pyrite oxidation is precipitated as goethite (see Fig. 4.7b). The

weight percentage of pyrite used in this reaction up to MOC is about 0.15 %.

Near the gas wells fresh air containing oxygen is supplied in each storage cycle. This situation is simulated using the kinetic batch model with constant air flow. Due to this constant supply, the dissolved O_2 concentration remains constant (Fig. 4.8b). After about 12.5 years pH decreases from 6 to 1.5 (see Fig. 4.8a) when dolomite in the mineral phase has been completely dissolved (see Fig. 4.8c) and H^+ from pyrite oxidation cannot be buffered any more by carbonate minerals. The resulting acidic solution shows an increase in the concentration of Fe as Fe^{3+}, because goethite precipitation stops but pyrite oxidation still continues, as well as a further slow reduction in pH. A low pH in the solution also leads to the slow dissolution of silicate and clay minerals, which shows as an increase of Si^{4+} concentration and later K^+ concentration. The solution species of Ca^{2+}, Mg^{2+} and SO_4^{2-} show the same behavior as in the case of no oxygen resupply (see Fig. 4.7a), but the overall change in concentration is much larger. The low pH in the formation fluid increases the risks of corrosion in the gas wells and thus needs to be considered when selecting the materials of the gas wells.

Due to the produced acid, pyrite oxidation leads to a complete dissolution of calcite after approximately 5.3 years and for dolomite after approximately 12.5 years (see Fig. 4.8c). A 60 % increase in the molar concentration of anhydite can be found after 20 years, due to the enrichment of $Ca^{2+}$and SO_4^{2-} concentration in the pore fluid. The relative change in silicate minerals, such as quartz, is less than 1 % (see Fig. 4.8d) due to the small change of porosity. Approximately 6 % of the mineral K-mica has dissolved after 20 years, resulting in an increase of the K^+ concentration in solution. After 20 years, about 12 % of pyrite has reacted with the dissolved O_2. The iron-containing minerals goethite, jarosite and the clay mineral kaolinite are therefore precipitating (see Fig. 4.8e). The precipitated goethite starts to dissolve after the pH of the formation fluid reaches around 2.0, which also leads to the precipitation of kaolinite and jarosite. The overall mineral dissolution and precipitation in the storage formation result in a small increase of porosity and thus permeability, with relative changes of about 0.3 % and 1.2 % respectively (see Fig. 4.8f). A slight decrease is found after 12.5 years, when all carbonates have been dissolved and kaolinite as well as jarosite start to precipitate. The overall change in mineral dissolution and precipitation near gas wells thus induces only minor changes in porosity and permeability, with also minor impacts on well deliverability.

4.3.6 Sensitivity analysis

Influence of mineral reactive surface areas

Parametrization of geochemical reactions in geochemical models involves a range of uncertainties, as e.g. the amount of pyrite reactive surface area may spatially vary strongly. During the Rhaetian time, the depositional system in the Northern German Basin changed spatially from a non-marine system in the east through a paralic system in the middle to a marine setting in the west (Doornenbal and Stevenson 2010). These sedimentary conditions typically lead to a strong variation in grain sizes and grain morphologies of the pyrite deposited, implying an uncertainty of the reactive mineral surface area. The possible range of

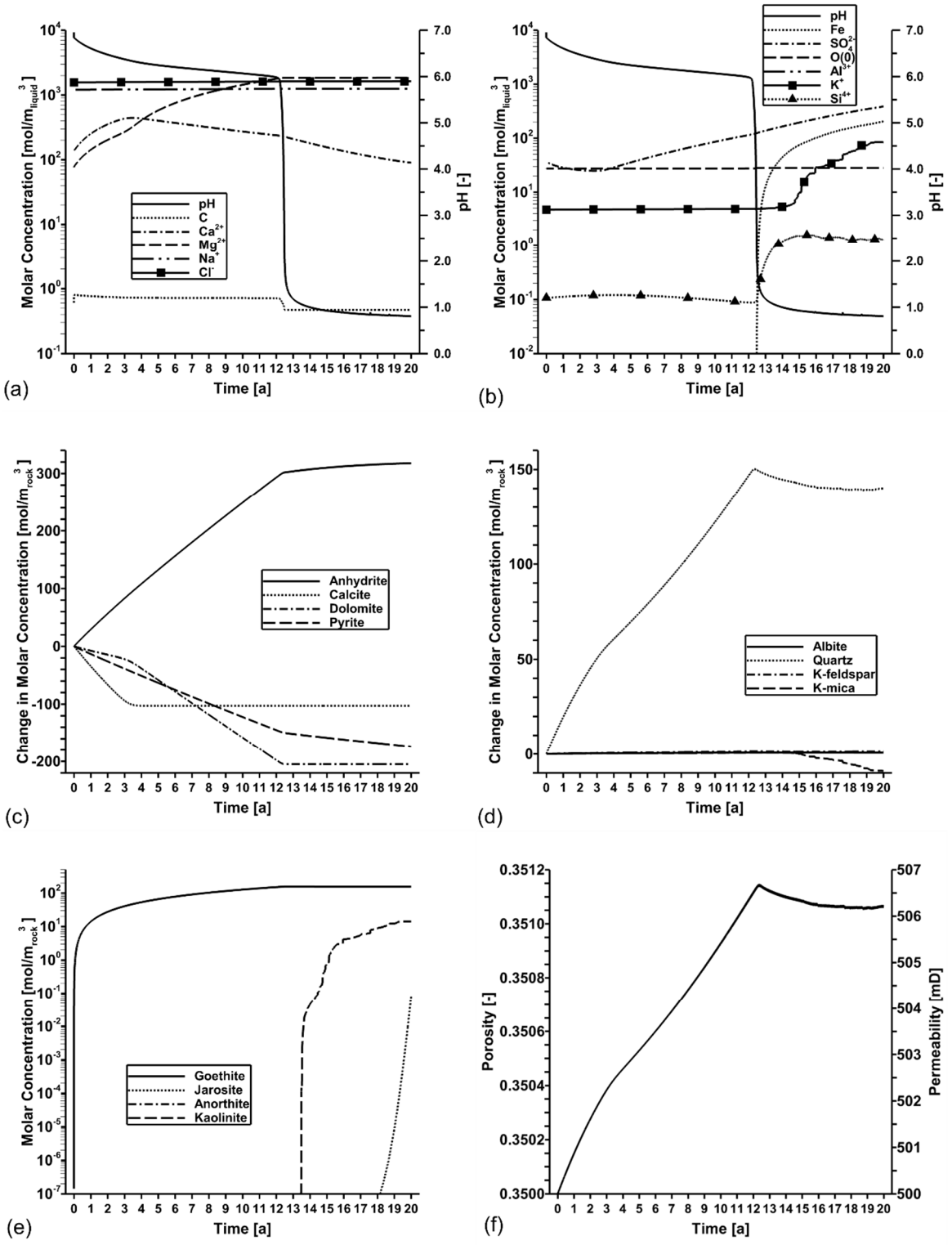

Figure 4.8 Geochemical composition of formation water and storage formation with oxygen replenishment. (a, b) pH and solution species of formation fluid (c, d) primary mineral compositions (e) secondary mineral compositions (f) porosity and permeability.

pyrite reactive surface area as reported by Bourg et al. (2015) is between 4×10^{-2} m^2/g and 1×10^{-4} m^2/g. Thus, larger surface areas than the value of 5.99×10^{-4} m^2/g used in this study are possible. Here, a roughness factor of 10 and a α factor of 10^{-2} is assumed to represent a larger reactive surface area of 5.99×10^{-3} m^2/g. For

Table 4.6 Change in components of O_2 and CO_2 within one storage cycle of 12 hours at reservoir pressure of 71 bar and 106.5 bar accounting for different mineral reactive surface areas.

Air Pressure	Time	A_{react}	O_2	CO_2	ΔO_2		ΔCO_2	
[bar]	[hour]	[m^2/g]	[mol]	[mol]	[mol]	[%]	[mol]	[%]
71.0	0		16209.64	27.88				
	12	5.99×10^{-5}	16209.12	28.43	-0.52	-0.003	0.55	1.98
		5.99×10^{-4}	16204.73	32.48	-4.91	-0.03	4.60	16.48
		5.99×10^{-3}	16163.60	68.25	-46.04	-0.29	40.37	144.78
106.5	0		24333.60	43.25				
	12	5.99×10^{-5}	24333.01	43.82	-0.59	-0.002	0.57	1.32
		5.99×10^{-4}	24327.85	48.80	-5.75	-0.02	5.55	12.82
		5.99×10^{-3}	24279.13	92.59	-54.47	-0.22	49.34	114.06

comparison, a roughness factor of 1 and a factor α of 10^{-3} is applied to represent a smooth geometric surface area of mineral grains with a smaller reactive surface area of 5.99×10^{-5} m^2/g.

Impact on short- and long-term changes of stored air pressure and composition

Accounting for different mineral reactive surface areas, the change in O_2 and CO_2 of the injected air within one storage cycle of 12 hours is shown in Table 4.6. Within one storage cycle, the O_2 in the injected air can decrease by 0.003 % at the smaller reactive surface area and up to 0.29 % at the larger reactive surface area, at a pressure of 71 bar. CO_2 increases accordingly by 1.98 % and 144.78 %, respectively. Therefore, even using a larger reactive surface area of 5.99×10^{-3} m^2/g, the loss of O_2 in the injected air within one storage cycle will not affect the flammability of the stored air mixed with the natural gas either.

Considering a longer residence time of 20 years, using a larger mineral reactive surface area of 5.99×10^{-3} m^2/g leads to a pressure drop of 7.8 bar within about 1.8 years (Fig. 4.9a) as well as the total depletion of oxygen in the stored air (Fig. 4.9b). MOC in the stored air is reached after already half a year, which is shorter than the time required for the initial fill of the gas reservoir. This faster decrease also

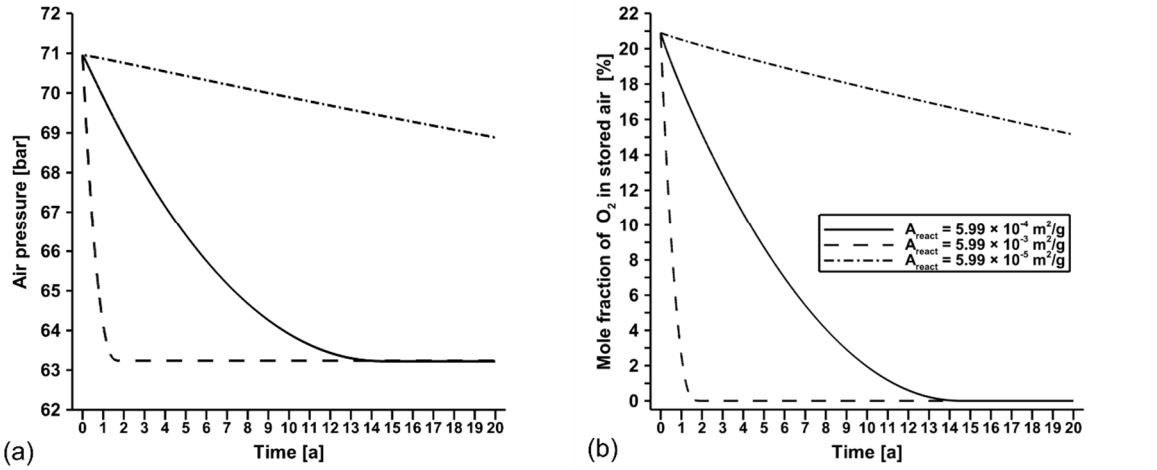

Figure 4.9 Influence of mineral reactive surface area on the change in the stored air without oxygen replenishment. (a) air pressure (b) oxygen mole fraction.

increases the risk of failure during operation of this diabatic CAES, as the stored air cannot be used for burning natural gas. However, lower reaction rates are also possible using a smaller reactive surface area of 5.99×10^{-5} m^2/g, which leads to a pressure drop of only 2.2 bar even after 20 years (Fig. 4.9a) and an oxygen mole fraction of 15 % (Fig. 4.9b). The depletion rate of O_2 in the stored air and the air pressure are thus very sensitive to the mineral reactive surface area, and for a reliable estimate of these changes, the analysis of this parameter of minerals from a target geological formation is thus required.

Impact on the porous storage formation

At the edge of the reservoir, where no oxygen is replenished during the cyclic operation, using a larger mineral reactive surface area of 5.99×10^{-3} m^2/g leads to a faster pH decrease to 5.12 within about 1.8 years. The pH remains constant afterwards as all oxygen has been consumed then (Fig. 4.10a). After 20 years, using a smaller mineral reactive surface area of 5.99×10^{-5} m^2/g, the pH has decreased to 5.47. The pH will further decrease until all oxygen has been consumed and will also reach 5.12 as in the other cases. If oxygen is not replenished, a different reactive surface

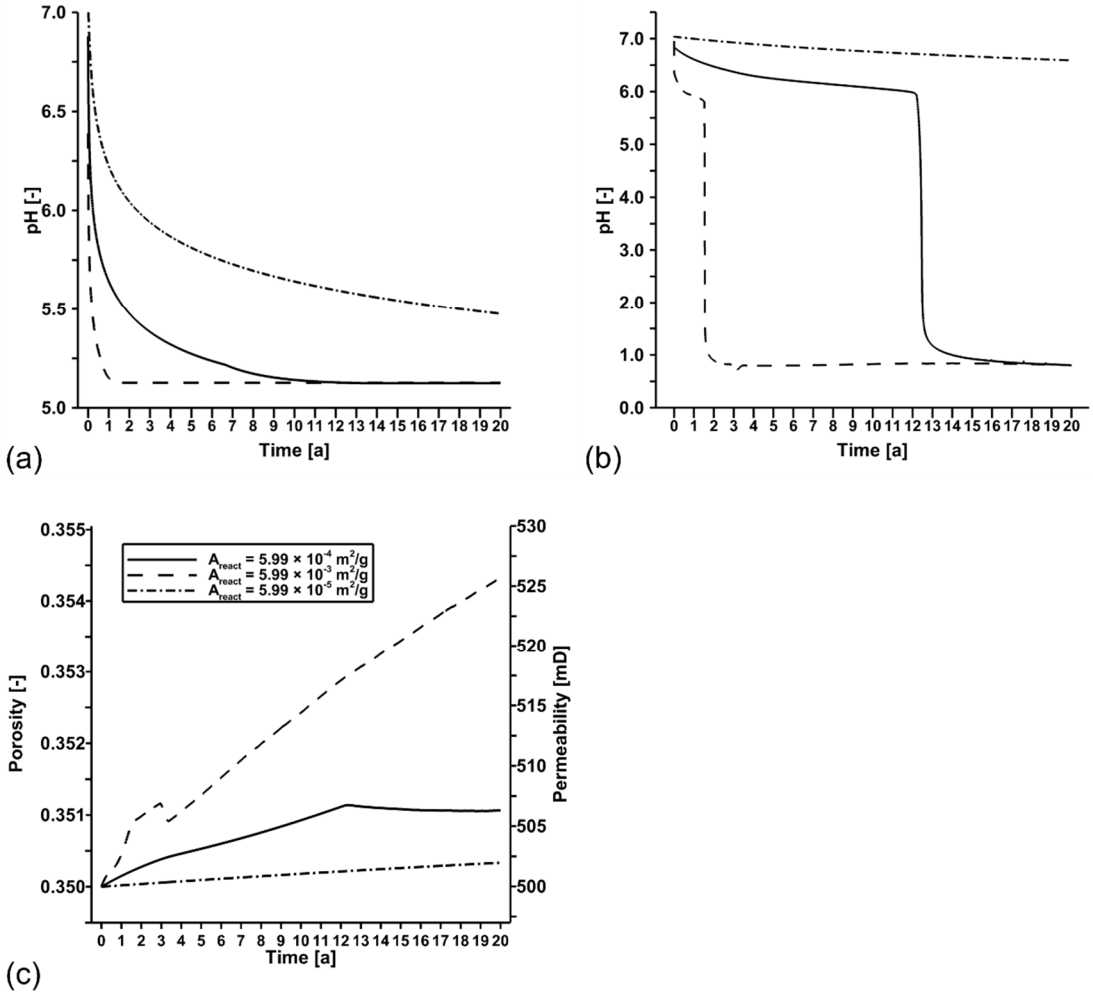

Figure 4.10 Influence of mineral reactive surface area on the change in the storage formation. (a) pH without oxygen replenishment (b) pH with oxygen replenishment (c) porosity and permeability with oxygen replenishment.

area only influences the rate of pH decrease but not the final magnitude.

However, near gas wells with a constant supply of oxygen containing fresh air, using a smaller reactive surface area of 5.99×10^{-5} m^2/g only causes a pH decrease to 6.58 after 20 years, which is even higher than the case without oxygen replenishment. This is because the CO_2 produced is extracted from the gas reservoir during each operation cycle. Therefore CO_2 partial pressure and solubility do not increase, as in the case without air replenishment. Using the larger reactive surface area, pH drops to 0.8 after about 2 years, and thus the risks of corrosion in the gas wells is increased substantially already at the beginning of the cyclic operation. The overall mineral dissolution and precipitation reactions induced in the storage formation result in relative increases of 1 % and 5 % of porosity and permeability after 20 years, as shown in Fig. 4.10c. This represents minor changes and thus will only slightly affect well deliverability.

Influence of pyrite mineral surface passivation

As pyrite oxidation is mainly a mineral surface controlled reaction (Chandra and Gerson 2010), the hydrolytic precipitation of ferric-ion-containing hydroxide may form a passivation layer on the pyrite mineral surface. Results from lab experiments on pyrite oxidation (Huminicki and Rimstidt 2009; Pérez-López et al. 2009; Berta et al. 2016) showed that carbonates present in the mineral or fluid phase reduce the reaction rate of pyrite oxidation due to the formation of a passivation layer. In the Rhaetian sandstone formation considered here, the mineral composition shows the presence of carbonate minerals together with pyrite, and these carbonates may help to form the passivation layer on the surface of pyrite.

Accounting for surface passivation in the model, the loss of O_2 of the stored air may be strongly reduced. To quantify this passivation effect, a rate law for pyrite oxidation is applied accounting for the surface passivation from Berta et al. (2016) (see Eq. (4-8)). This rate law also accounts for the influence by the partial pressure of O_2 in the gas phase.

$$k \cdot g(c) = (f_{rest} + f_{pass} \cdot pass) \cdot k_{WR} \tag{4-8}$$

where, f_{rest} [-] is the fraction of un-passivated pyrite, f_{pass} [-] the fraction of passivated pyrite, k_{WR} [$mol/m^2/s$] the rate law from Williamson and Rimstidt as shown in Eq. (4-9). The factor $pass$ is given by Berta et al. (2016) as:

$$pass = \left(1 - \frac{m_0 - m}{m_0} \cdot f_1 \cdot e^{f_2 \cdot P_{O_2}}\right)^{f_3}$$

$$\text{and } 1 \geq pass \geq 0 \tag{4-9}$$

where, m_0 [mol] is the initial moles of pyrite, m [mol] the moles of pyrite at a given time, P_{O_2} [bar] the partial pressure of O_2, and f_1 [-], f_2 [-] and f_3 [-] fitted parameters as 100, -0.015 and 0.75, respectively.

Impact on short- and long-term changes of stored air pressure and composition

Considering the surface passivation of pyrite, at a pressure of 71 bar only 0.006 % of O_2 in the injected air has reacted (Table 4.7). This value is five times smaller than in the case without surface passivation. The produced acid reacting with carbonates leads to a relative increase of 3.47 % CO_2 in the injected air. At the higher pressure of 106.5 bar, the relative changes are 0.004 % and 2.47 %, respectively. Because of

Table 4.7 Change in components of O_2 and CO_2 within one storage cycle of 12 hours at reservoir pressure of 71.0 bar and 106.5 bar accounting for surface passivation.

Air Pressure [bar]	Time [hour]	Pyrite oxidation kinetic	O_2 [mol]	CO_2 [mol]	ΔO_2 [mol]	ΔO_2 [%]	ΔCO_2 [mol]	ΔCO_2 [%]
71.0	0		16209.64	27.88				
	12	no passivation	16204.73	32.48	-4.91	-0.03	4.60	16.48
		with passivation	16208.67	28.85	-0.97	-0.006	0.97	3.47
106.5	0		24333.60	43.25				
	12	no passivation	24327.85	48.80	-5.75	-0.02	5.55	12.82
		with passivation	24332.53	44.32	-1.07	-0.004	1.07	2.47

surface passivation, the changes of O_2 and CO_2 in the injected air within one storage cycle are much smaller, which will not affect the flammability of the stored air mixed with the natural gas.

Considering a longer residence time of 20 years, pressure of the stored air decreases to 69.4 bar (see Fig. 4.11a) accounting for the surface passivation on pyrite, and the corresponding mole fraction of O_2 in the stored air is 16.4 % (see Fig. 4.11b). The same amount of change in oxygen can be observed at about 1.5 years without the surface passivation, which shows that the formed passivation layer strongly reduces the oxygen depletion rate. Thus, in the case of surface passivation occurring, the mole fraction of O_2 in the stored air is decreasing only slightly even for longer residence time, and values are always above MOC. Because the oxygen depletion rate is strongly determined by the kinetics of pyrite oxidation, experimental tests for a target formation are required to reliably quantify these impacts.

Impact on the porous storage formation

At the edge of the reservoir without oxygen replenishment, accounting for the surface passivation of pyrite leads to a pH decrease to 5.54 after 20 years (Fig. 4.12a) which is close to the fluid pH of 5.12 considering no surface passivation. Because oxygen is not replenished at the reservoir fringe, surface passivation does not significantly change the pH of the formation fluid there.

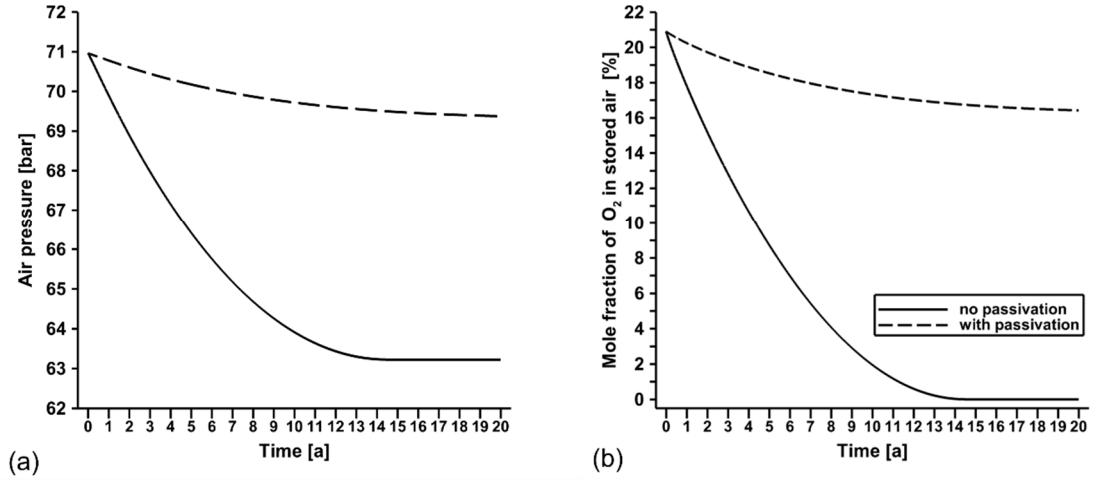

Figure 4.11 Influence of surface passivation on the change in the stored air without oxygen replenishment. (a) air pressure (b) oxygen mole fraction

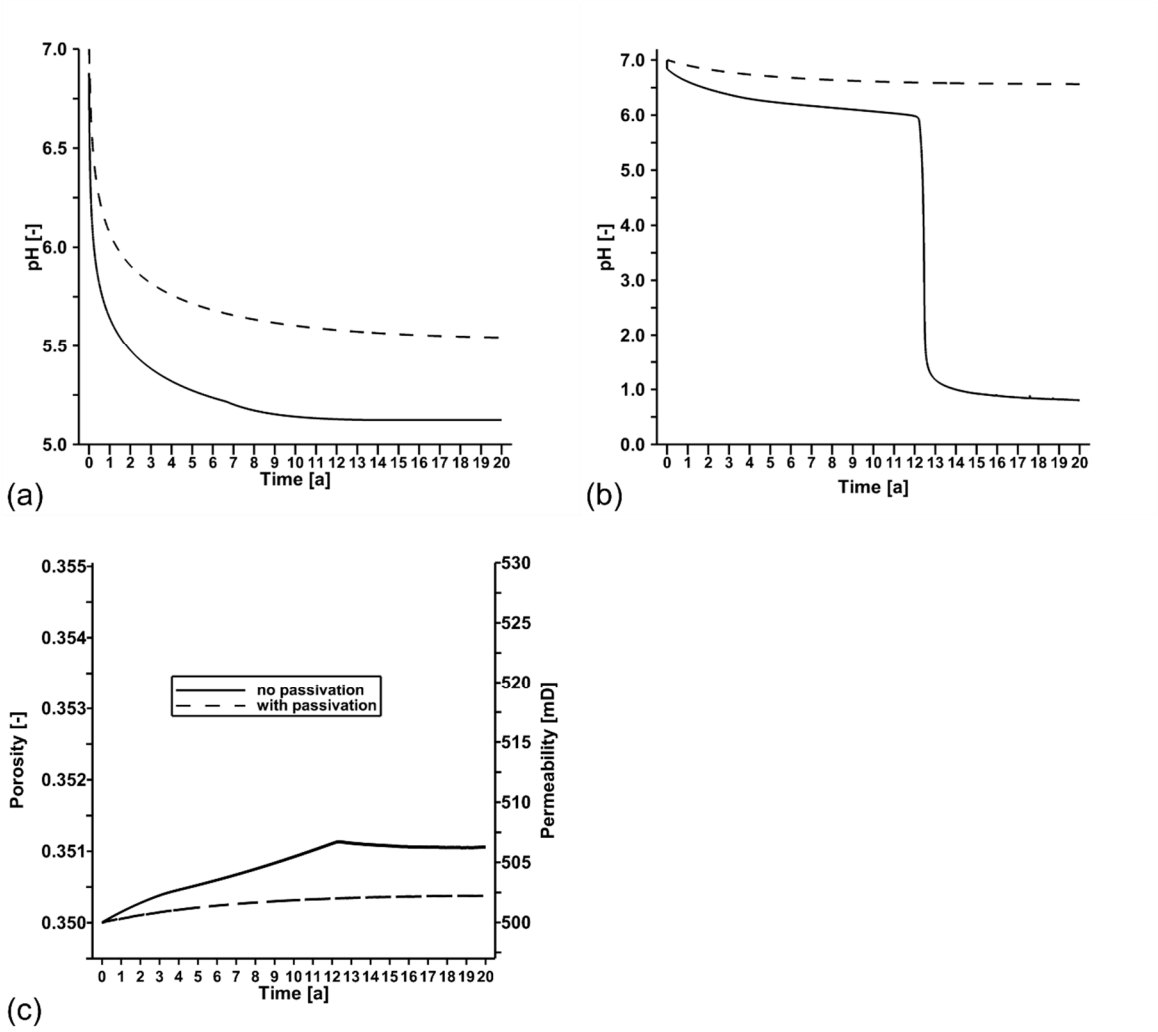

Figure 4.12 Influence of mineral surface passivation on the change in the storage formation. (a) pH without oxygen replenishment (b) pH with oxygen replenishment (c) porosity and permeability with oxygen replenishment.

Near gas wells with a constant supply of fresh oxygen containing air, however, accounting for surface passivation stabilizes pH at a neutral value of 6.56 even after 20 years (Fig. 4.12b). This strongly reduces the risks of corrosion in the gas wells for the operation of CAES. Correspondingly, after 20 years, overall mineral dissolution and precipitation in the storage formation causes relative changes of only 0.08 % and 0.40 % in porosity and permeability (see Fig. 4.12c). This effect is thus very small and does not change well deliverability.

4.3.7 Reduction of storage capacity and storage rates

Due to the change in the stored air composition, air pressure in the formation decreases and also air density increases as gas density of CO_2 is higher than O_2. Both changes can reduce the storage capacity, i.e. potential power output, by lowering the extraction air flow rate. To quantify the reduction in storage capacity, the simulated results of the stored air pressure and composition for different residence times are used as the initial condition to initialize the CAES reservoir model described in section 3.2. However, the air components

include CO_2 in this situation. This analysis stands for the possible power reduction without an intermediate refill. The following results are based on the residence times simulated in section 4.3.4, i.e. the base case scenario. Different residence times from the sensitivity analysis can change only the times for the estimated power reduction not the magnitudes.

The storage capacity and the storage rates are assessed by (see section 3.4): the short-term power output for a thirty-minute extraction, and, the time for a continuous power output of 321 MW can be maintained. Assuming a constant combustion efficiency of the gas turbine at different air compositions, the instantaneous power output for a thirty-minute extraction determined for different air residence times in the storage formation. Instantaneous power output is found to decrease from 468 MW to 358 MW after 4.6 years when MOC in the stored air is achieved (see Fig.4.13a) and natural gas cannot be burned along with the extracted air. For longer residence times, power output is only due to mechanical exergy, which are 148 MW after 5 years and 125 MW after 14.5 years when all oxygen is depleted.

For residence times of days, a continuous power output of 321 MW can be achieved for 9.6 hours. Twelve vertical storage wells are required to accommodate this power output of a diabatic CAES. After a residence time of one year the duration for a continuous power output reduces to below 6.0 hours (see Fig. 4.13b). This shows that without an intermediate refill of air the gas reservoir cannot sustain the required mass flow rate of 417 kg/s. In this case, more storage wells are required to reduce the pressure loss in the reservoir and the wells.

4.3.8 Discussion

Gas phase mixing in the storage reservoir

The short-term changes in stored air composition during one storage cycle assessed using the kinetic batch model show a very small decrease in oxygen content due to the induced geochemical reactions. This shows that on this short time scale no geochemical impacts on storage operation will occur. The long-term changes in stored air composition however indicate that the mole fraction of oxygen in stored air may be reduced to below MOC and even to zero at large time scales. In this case, an operation failure of the diabatic CAES facility will occur. This can be mitigated by a refill of fresh, oxygen rich air. These two models

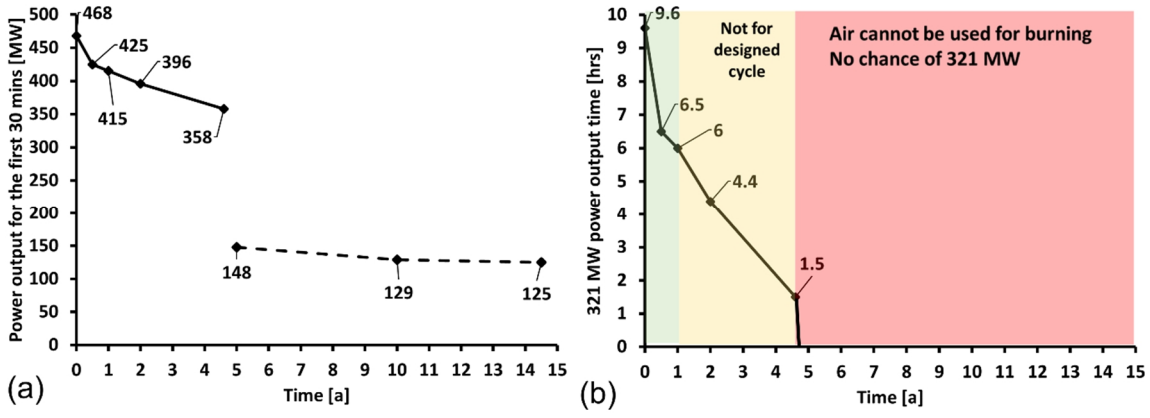

Figure 4.13 (a) Short-term power output for a thirty-minute extraction. The dashed line indicates that only mechanical exergy is considered. (b) Time a continuous power output of 321 MW can be achieved.

represent the "end members" of the spectrum of residence times that will occur in a gas storage reservoir. In a real porous gas storage formation, however, mixing between injected fresh air and air stored for longer times will occur. These mixing effects are not explicitly considered here by a full reservoir model, as they will depend strongly on the geometric and hydrodynamic characteristics of the storage formation. Thus, general findings on this mixing cannot be derived, but mixing effects are discussed in the following.

The mole fraction of O_2 in the extracted air will be between the two bounding cases considered here, providing a lower power output in the early stages of storage use than indicated by the short-term model. This effect is also found by Oldenburg and Pan (2013b), who considered porous formation CAES using CO_2 as cushion gas and found that in the case of 20 m air-CO_2 interface noticeable amounts of CO_2 were produced along with the extracted air during the first production cycle. With on-going cyclic operation, however, the mole fraction of O_2 in the extracted air will increase as oxygen mixed into the gas reservoir in prior cycles is recovered along with the short-term stored air. Some of the oxygen will diffuse to the reservoir fringe, due to the concentration gradient in the storage air, and supply somewhat more oxygen there than considered in the long-term simulations without gas flow. This may result in a stronger decrease of pH there than given by the current model. The extent of oxygen mixing and diffusion in the gas phase will thus also depend on the storage cycles used.

Mineral assemblage of the Rhaetian sandstone

In this study, one possible mineral assemblage is chosen to represent the mineral composition in the Rhaetian sandstone. Using other minerals, such as gypsum instead of anhydrite, or, gibbsite instead of kaolinite, would slightly change the simulation results, but would not change the basic findings of this study, such as oxygen reduction due to induced geochemical reactions. However, the amount of redox-sensitive minerals available in the mineral assemblage, here represented by pyrite, may affect the amount of oxygen reduction in the gas phase. The available core samples from the Rhaetian sandstone show amounts of pyrite in the mineral composition varying between zero and up to 6% (Dethlefsen et al. 2014). Therefore, the amount of pyrite is likely lower than the 5.7% assumed here, which would reduce the geochemical impacts accordingly. If the pyrite content is less than 0.15%, oxygen concentrations will always remain above MOC, which means that air can be stored for long. However, if organic carbon or other ferrous-containing minerals are present, the induced geochemical reactions may still result in a reduction of oxygen concentration below MOC because they can also react with oxygen.

Impact of residual water saturation

Gas dissolution in the residual formation water in the porous storage formation is considered here as an equilibrium process, because a small residual water saturation of 0.2 is assumed. If larger residual water saturation occur, the travel time for the dissolved oxygen to the mineral surfaces, where the reactions occur, as well as the respective travel time of carbon dioxide towards the gas phase, are increasing strongly. Accounting for this diffusion controlled transport process for the

dissolved gas components would thus further limit the reaction rates and the oxygen consumption. Therefore, at larger residual water saturations in the storage formation the depletion rate of O_2 in the stored air and the power reduction rate will be slower than shown here. The model used here is thus conservative with respect to this effect.

The cyclic injection of dry air may lead to evaporation of the residual water and thus a reduction of water saturation or a complete dry out near the wells. The induced geochemical reactions in the storage formation would thus be further reduced or even stopped when the formation is fully dehydrated, as the reactions can only occur if water is present. This would increase the relative permeability for gas flow and thus storage performance, as higher rates can be obtained. At the same time, the precipitation of all dissolved minerals in this dry out zone may reduce permeability and porosity, which would counter this effect.

4.4 Summary

A realistic diabatic CAES operation scenario based on the existing Huntorf power plant and employing the Rhaetian sandstone formation in the North German Basin as porous storage reservoir is investigated for induced hydraulic, thermal, and geochemical impacts.

The induced hydraulic impact is assessed in terms of pressure response in the storage formation during a 2-year initial air filling and a 10-year cyclic operation. To estimate the possible induced pressure response, the storage operation of this CAES is numerically simulated using the oil and gas reservoir simulator ECLIPSE 300 in compositional mode. Simulation results show that the well BHP reaches 104 bar in maximum after the 2nd stage of initial fill and drops to 60 bar after the last air extraction. Because of the assumed extended boundary conditions, the average pressure is found to decrease over time regardless of the cyclic operation. In the storage formation, the maximum pressure build-up is found to be about 33 bar at one-meter distance from the well I1 after the 2nd stage of initial fill, and the maximum pressure drop is about 11 bar after the last air extraction. At a distance of 10 km from the well I1, the induced pressure build-up can reach about 3 bar in maximum at 2.7 years. In comparison to the initial fill, the cyclic behavior in pressure response can be observed within a distance of 400 m from the well I1, which is roughly at the edge of the gas reservoir. This is because the air is highly compressible which dampens the pressure propagation and the cyclic air mass is much smaller compared to the air in place.

To quantify the induced thermal impacts, the potential temperature change in the storage formation is numerically simulated for the 12-year storage operation using the reservoir simulator ECLIPSE in the thermal mode. The injected air temperature during the initial fill and the cyclic operation is assumed close to the average reservoir temperature. Simulation results show that the temperature at the bottom of gas wells reaches 39.0 °C at maximum after the second stage of the initial fill when the BHP also reaches its maximum. At the end of the initial fill, the temperature is found to be 35.6 °C. During the cyclic operation, the temperature fluctuations at the bottom of gas wells follow the same pattern as the observed pressure responses. The highest observed temperature at well bottom is 38.9 °C at the first injection of the cyclic

operation, and the lowest temperature is found to be 32.0 °C after the last extraction. In the storage formation, after the 2nd stage of the initial fill, the maximal temperature increase of 5.3 °C is observed very close to the gas wells. At the end of the initial fill, a temperature increase of 1 °C is observed at a distance of 10 m above the reservoir formation, and at a distance of 20 m from well I1 in the reservoir formation. After the last air injection of the 10-year cyclic operation, the maximal temperature increase of 4 °C is observed due to air injection at a distance of 5 m from well I1. Further away from well I1, a cumulative decrease in temperature is found during the 10-year cyclic operation due to the Joule-Thomson effect. A decrease of more than 5 °C is observed at a distance of between 15 m to 40 m from well I1, and the maximum decrease is about 5.8 °C at roughly 25 m. A temperature decrease of larger than 1 °C is found vertically at a distance of 40 m above and below the reservoir formation. Laterally, this temperature decrease is found at a distance of 100 m from well I1 in the reservoir formation.

Due to the presence of pyrite in the mineral assemblage of the Rhaetian sandstone, injecting air into the storage formation induces pyrite oxidation and other geochemical reactions. To assess the induced geochemical impacts on the stored air as well as the storage formation, these reactions are investigated under a consistent geochemical reaction system for the Rhaetian sandstone. Using the coupled multiphase-multicomponent ECLIPSE-OpenGeoSys-PHREEQC simulator, the scenario analysis and process based kinetic batch models are numerically simulated for such a geochemical system. A sensitivity analysis is performed accounting for the uncertainties in model parameterization, such as the mineral reactive surface area and the kinetics of pyrite oxidation. Simulation results show that within one storage cycle of air injection and extraction, i.e. 12 hours residence time in the storage formation, the loss of O_2 can vary from 0.003 % to 0.29 % relatively. The oxygen loss in stored air is found to be very small, which does not affect the flammability of the stored air mixed with natural gas and thus will not influence the cyclic operation of CAES. Considering a longer residence time, e.g. for the initial filled air, the air pressure decreases continuously due to the change in air composition as O_2 consumption and CO_2 production. After two years, the storage pressure can drop from 71 bar to 69 bar, and the mole fraction of O_2 in air decreases to 15.18 %. The estimated corresponding power output decreases from 468 MW to 415 MW assuming that the combustion efficiency of the gas turbine remains constant. At about 4.6 years of storage time, the storage pressure drops to 66.7 bar and the mole fraction of O_2 reaches the minimum oxygen concentration (MOC) for flame propagation. If larger mineral reactive surface areas are considered, the time for reaching the MOC is reached at about half a year. The air injected during the 2-year initial fill thus cannot be used for burning the natural gas anymore in this diabatic CAES without air refill, which indicates an adiabatic CAES may be a preferable option for the porous formation storage. However, considering small mineral reactive surface areas or mineral surface passivation, the concentration of O_2 in stored air does not reach MOC even after 20 years. Regarding the potential change in the storage formation near gas wells, only at a small mineral reactive surface area or with

mineral surface passivation can prevent the pH of the formation fluid to drop below 1.0. Otherwise, the formation fluid can become a strong acidic solution (pH < 1.0) after 20 years due to induced geochemical reactions, which increases the risks of gas well corrosion. The overall mineral dissolution and precipitation result in an increase of porosity and permeability in the storage formation, but the relative changes are very small and at a maximum of 1 % and 5 %, respectively, which will not affect the storage performance in terms of well deliverability.

5 Model development for energy storage at real geological sites

The following chapter presents the model development of a workflow allowing for the investigation of underground energy storage at real geological sites. This workflow is to combine realistic static geological models of the subsurface with numerical dynamic process models for fluid flow and transport as a model basis for determining storage characterization and assessing induced impacts for real conditions. The technical details of implemented methods are described in section 5.2, including the conversion of numerical grids, the transfer of parameterized properties, and the projection of well trajectories. To test the applicability of the developed tool, a scenario of a deep geothermal exploration in a real geological setting is presented in section 5.3 using numerical simulations.

The content of this chapter is published as
Wang, B., & Bauer, S. (2016). Converting heterogeneous complex geological models to consistent finite element models: methods, development, and application to deep geothermal reservoir operation. Environmental Earth Sciences, 75(20), 1349. doi:10.1007/s12665-016-6138-8.

5.1 Introduction

Mathematical modelling of subsurface processes in geoscientific applications requires adequate representation of both the static subsurface as well as the process dynamics. Applications include geothermal energy extraction, ground water abstraction, and oil and gas recovery, underground storage of natural gas as well as deposition of hazardous materials in the subsurface. To investigate the use of the geological subsurface and to quantify possible induced impacts, a multidisciplinary approach is required, which combines fields of geology, numerical modelling, geochemistry and geophysics, etc. (Blöcher et al. 2010b; Franco and Vaccaro 2014; Sa et al. 2014; Pfeiffer and Bauer 2015; Bauer et al. 2015). Within this approach, a static model, which can correctly represent the geological nature of the studied reservoir and its environment in the subsurface, is the prerequisite in order to achieve a reliable evaluation and assessment through numerical simulations. Dynamic models are thus required for simulating reservoir behaviors and dimensioning of the individual operation as wells as for the assessment of induced effects.

Large scale geological models in the subsurface often show a high complexity in geometry and hydraulic connectivity, due to the existence of faults, pinch-outs and eroded layers. With the interest of exploring and exploiting hydrocarbon reservoirs in the subsurface, the petroleum industry has invested large efforts in building static

geological models and has developed powerful geological reservoir modeling codes, such as GOCAD (Geological Object Computer Aided Design) (Paradigm 2016) or Petrel (Petrel E&P Software Platform) (Schlumberger 2014). Two basic approaches, i.e. a surface based and a volume based approach, are applied to model the geometrical complexity of the subsurface. The surface based approach (Neave 2007) is commonly known as the pillar-gridding technology, which firstly models faults as pillars and horizons as smooth planes, and later creates geological layers by following defined topological relations. The volume based approach by Souche et al. (2013) models geological layers directly by using an unstructured mesh which is internally constrained by faults. Afterwards, the resulting geological models need to be discretized for simulation purpose, and the corner point grid (Ponting 1992) has been utilized in the above mentioned commercial software as an industrial standard (Aarnes et al. 2008). The corner point grid is represented by a set of hexahedral blocks with eight nodes and twelve edges. The length of vertical or inclined edges stands for the thickness of the formations, and the eight corner points represents the top and bottom horizon depths of geological formations. In complex subsurface structures, the thickness of the formations becomes smaller or even zero where the formations are partially or completely eroded and where pinch-outs exist. This leads to reduced or zero length of those vertical or inclined edges, and thus degenerated or even disappearing blocks.

To transfer a corner point grid based geological model to a workable dynamic reservoir model, a procedure of grid and property data conversion is required. Generally, two approaches exist to convert models to be used in grid based numerical schemes, as e.g. finite volume (FV), finite difference (FD) or finite element (FE) methods. In the first approach, the corner points of important entities, e.g. faults and horizons, are extracted from the geological model, and the numerical mesh is constructed using existing meshing tools (e.g. the 'MeshIt' tool developed by Cacace and Blöcher (2015)) or through a resampling procedure (e.g. the 'GO2OGS' developed by Fischer et al. (2015)). This approach is similar to the volume based approach in geological modelling methods, and it can have many freedoms in modeling subsurface geological complexity, e.g. faults and fractures, by a consistent unstructured mesh (e.g. Blöcher et al. 2010a; Zehner et al. 2015). In this approach, the parameters can be consistently transferred to the elements based on their geological group index, but within a geological group, the discrepancy will be introduced element-wise in transferring subsurface heterogeneity parameterized on an elemental level in the geological models to reservoir models, e.g. permeability and porosity, and thus the generated mesh is often parameterized after the conversion before being utilized in reservoir simulations. The approach also needs substantial technical steps and procedures, to arrive at a consistent simulation mesh. The second approach utilizes corner point grid based geological models, which are fully discretized and parameterized for simulation purpose. It directly converts individual blocks in the corner point grid by maintaining their individual polyhedral geometry, and transfers heterogeneous parameters from individual blocks to converted elements. Although the representation of geological complexities in

the converted mesh is restricted by their representation in the original corner point grid, this approach produces consistent reservoir models without reconstructing the mesh and reparametrizing it afterwards. This is thus a comparatively fast approach.

The direct conversion approach has been implemented by Ni and Chen (2014) for GOCAD SGrid models, and by Graupner et al. (2011) and Park et al. (2014) for Petrel grids. These implementations have the restriction that the corner point grid does not contain any degenerated blocks. However, in the presence of degenerated blocks, as they necessarily occur when more complex geological features are included, inconsistent elements arise and thus the conversion from blocks to only hexahedral elements fails. To resolve this, Aarnes et al. (2008) implemented a non-trivial scheme by partitioning each block into six or less tetrahedrons. Since a geological model often contains millions of blocks in a grid, this scheme will increase the number of corresponding elements by almost a factor of six after conversion, and thus lead to large computation times of the resulting reservoir simulation models. Accordingly, besides hexahedron and tetrahedron, the direct conversion of degenerated blocks of a corner point grid requires the implementation of other types of polyhedrons. During the conversion as well as in the FE code, only this partitioning approach allows for a geometrically consistent representation of the geological features in the numerical mesh and ensures a consistent computational mesh for the process simulation. As the elements can inherit parameters and data straightforwardly from the partitioned blocks, this direct conversion approach also guarantees a consistent parameter and data transfer between the corner point grid and the FE mesh. This assists to couple commercial reservoir simulators with FE based open source software (Graupner et al. 2011; Pfeiffer et al. 2016), e.g. the coupling between the Eclipse reservoir simulation software (Schlumberger 2016) with OpenGeoSys (Kolditz and Bauer 2004), and can be especially used to simulate induced geochemical reactions (e.g. Mitiku et al. (2013) and Li et al. (2014)).

In addition to a consistent numerical mesh representing subsurface features in reservoir models, wells are the main elements of an injection and extraction system. Open well screens describe the locations of interaction with the geological formations, e.g. locations for water and gas injection and extraction, and thus locations of largest pressure changes and highest occurring gas saturation (Benisch and Bauer 2013; Benisch et al. 2014). Besides, wellbores penetrating through geological formations are widely considered as the main possible leakage pathways, e.g. production or abandoned wells in geologic carbon sequestration (Pan et al. 2011). Due to the geometrical complexity and the scale of dynamic reservoir models, wells are often first designed in static geological models and later transferred to dynamic models. For instance, wells designed in Petrel can be exported as connection and completion data arrays to the Eclipse reservoir simulation software. Among the first-kind approaches of converting geological models to dynamic models, ‘MeshIt’ from Cacace and Blöcher (2015) is able to adapt well data as 1D polylines into an FE mesh. However, to the best of knowledge, none of the direct conversion approaches have the same feature.

Therefore, a new workflow is introduced in this chapter to convert a corner point grid based static model to a consistent finite element based dynamic model. This workflow avoids the problems of inconsistent data transfer or excessive increase in element number by an efficient and accurate grid block partitioning strategy, which honors the individual geometrical situations of each block. Geological parameters, such as permeability and porosity, are transferred from the corner point grid blocks to the FE mesh elements accounting for block partitioning. Additionally, well trajectories, open screen lengths and corresponding well data are transferred as nodes and polylines in the converted FE mesh. As a proof of concept, the new workflow is implemented into a mesh and parameter converter, and the software is tested by applying it to model a hypothetical geothermal reservoir operation at a real geological site in Schleswig-Holstein, northern Germany.

5.2 Corner point grid conversion workflow

5.2.1 Blocks and pre-processing

In a corner point grid, a set of hexahedral blocks with eight corner nodes and twelve edges is able to represent the subsurface complex geological structures, such as faults, pinch-outs and eroded layers, but not the subgrid fracture networks, which are often modeled as grid properties. In individual blocks, each set of four nodes at the top and bottom follows the spatial geometric shape of formation horizons, and the four vertical or inclined edges in between stand for the thickness of formation layers.

Fig. 5.1a shows a side view in the x-z plane of a corner point grid containing a fault structure. At the fault plane (see Fig. 5.1a closer view), the nodes of the blocks representing the formation layers adapt to the fault slip, which creates non-neighbor blocks at different sides of the fault plane. The length of vertical or inclined edges changes with the varying thickness of the formation layers close to the fault. Here, the formation layers are shifted and not eroded completely, so the formation thickness is not zero and thus the blocks remain as eight-node hexahedral blocks. Fig. 5.1b shows a side view in the *x-z* plane of a corner point grid representing a stack of geological formations containing anticlinal structures. In this side view, the thickness of the geological formations varies significantly due to erosion. Correspondingly, the length of those four edges in each block changes as well (see Fig. 5.1 closer view). When a formation becomes thinner, those four edges become shorter. When a geological formation is completely eroded, i.e. its thickness reduced to zero, those four edges in the blocks will also reduce to zero length. This can be clearly seen in Fig. 5.1, e.g. for the light green layer.

For a block, any number of those four edges can reduce to zero length, i.e. collapse, and thus a variety of degenerated block types exists. A 3D view of possible types of degenerated blocks in a corner point grid representing a typical eroded formation layer is shown in Fig. 5.2. The degenerated blocks often appear close to where erosion happened, e.g. close to the fold center of an anticline. The blocks marked with red lines represent the eroded part of the formation, i.e. blocks with four vertical edges of length zero and thus also zero volume. In the transition area, different

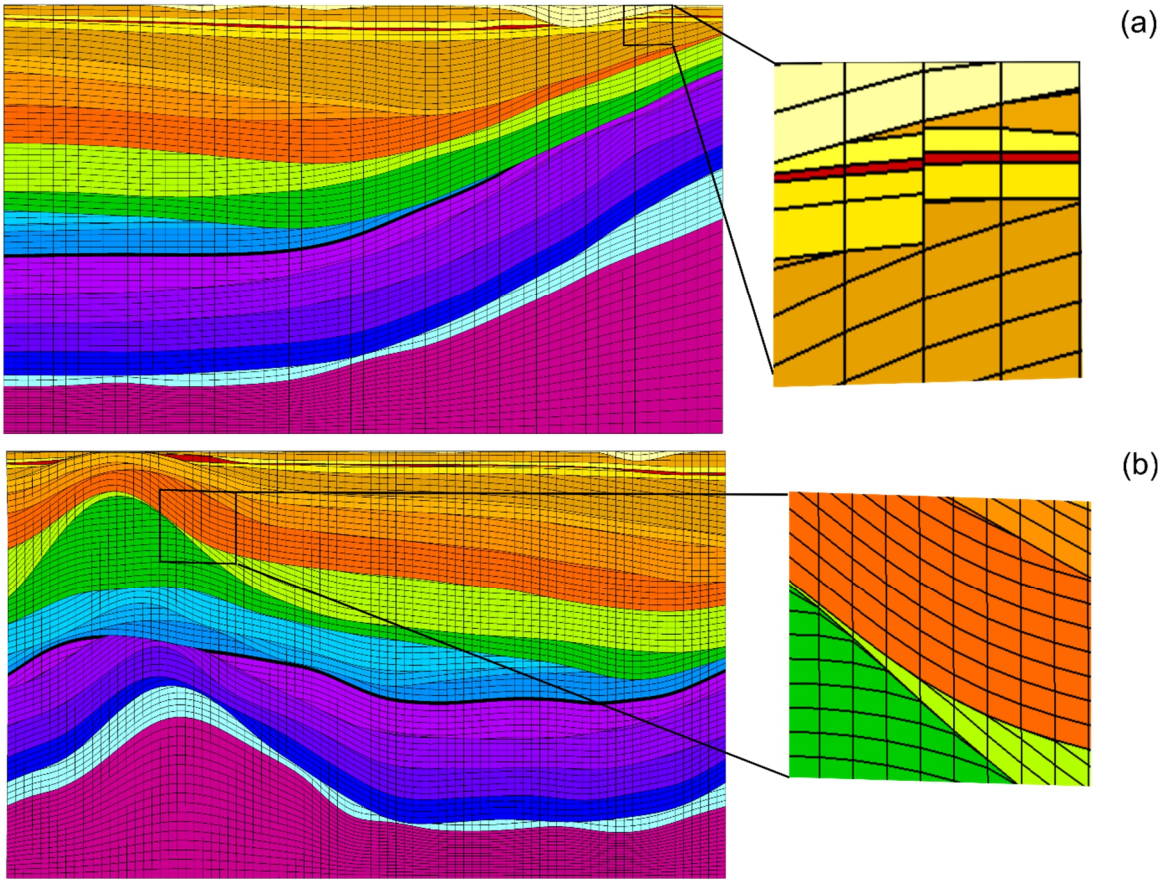

Figure 5.1 Side view of a corner point grid with vertical pillars including faults (a) and anticlinal structures (b). Different colors indicate different formations, designated by uniform material indices.

numbers of those four edges collapse and form degenerated five-node, six-node and seven-node blocks, respectively. The remaining part of the layer is conform and consists of eight-node hexahedral blocks.

Due to the problems caused by degenerated blocks, e.g. zero-volume blocks, double counting nodes and wrong neighboring information, a pre-processing on the block data structure is performed before executing the individual block partitioning procedure. In corner point grids, zero-volume blocks disappear and are marked as inactive blocks. While the grid is read into the mesh converter, those blocks are thus removed directly and only store active blocks with non-zero-volume ones as eight-node structure as they appear in corner point grids. Due to the existence of five-, six-, and seven-node blocks, more than one node appears at one position after the edges collapse and this leads to non-unique node numbering. Therefore, a procedure for numbering the nodes uniquely loops over all the blocks, compares the coordinates of each node and removes the repetitive ones. A node list consisting of individual unique indices and the node coordinates is constructed, and these unique indices are assigned back to the nodes of corresponding blocks in their eight-node structure. Connectivity information, e.g. faces and neighbors, is adapted to account for zero-volume and degenerated blocks. Some blocks have less than twelve edges, three-node faces and non-neighbor connections. On the basis of the unique node numbering, the faces of each block are reconstructed, and each face is a unique entry containing node indices, number of face nodes, face normal vector and block indices this face

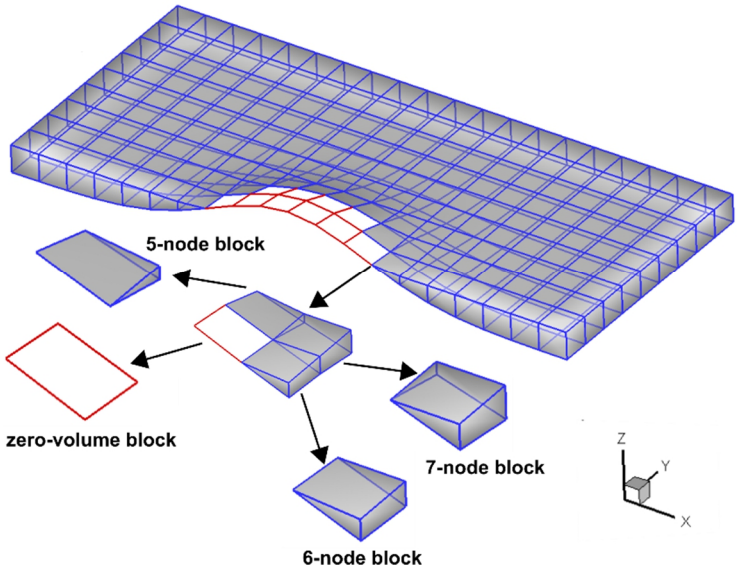

Figure 5.2 A 3D view of possible types of degenerated blocks. Blocks with red lines represent zero-volume blocks; blocks with blue lines represent degenerated blocks and hexahedron blocks.

belongs to. Similar to the node, the face indices are assigned back to each block and thus neighboring information between blocks can be determined by comparing their joint faces. Two blocks with zero-volume blocks in between are marked as non-neighbor connection in corner point grids, but in FE meshes, they are marked as neighbors because they share the same face. This is of great importance to the following partitioning conversion scheme because neighbor blocks have to maintain consistent joint faces in FE meshes.

5.2.2 Individual block conversion

As explained in section 5.2.1, the degeneration is caused by collapsed vertical or inclined edges in each block. To handle the degenerated blocks (see Fig. 5.2) and consistently convert them to finite elements, these blocks are partitioned according to the newly developed workflow. How each block is partitioned is determined by the specific type of degenerated block. According to the number of collapsed edges, five block types exist, and the conversion scheme of each type is schematically illustrated in Fig. 5.3. Only one representative case for each type is shown, but the converter accounts for all variations in each type due to changes in the positions of collapsed edges.

Type 1: None of the four vertical edges of this block has zero length. The block is converted to a hexahedron element. However, if in the same column the neighbor block above or below is partitioned, then this hexahedron element is also partitioned into two prism elements (red dashed lines) in order to maintain consistent joint faces between the elements.

Type 2: One of the four vertical edges of the block has zero length. The block is divided into one prism element and one pyramid element.

Type 3a: Two neighboring vertical edges at the same face of the block have zero length. The block is converted to a prism element. Similar to type 1, if in the same column the neighbor block above or below needs to be partitioned, then this prism element

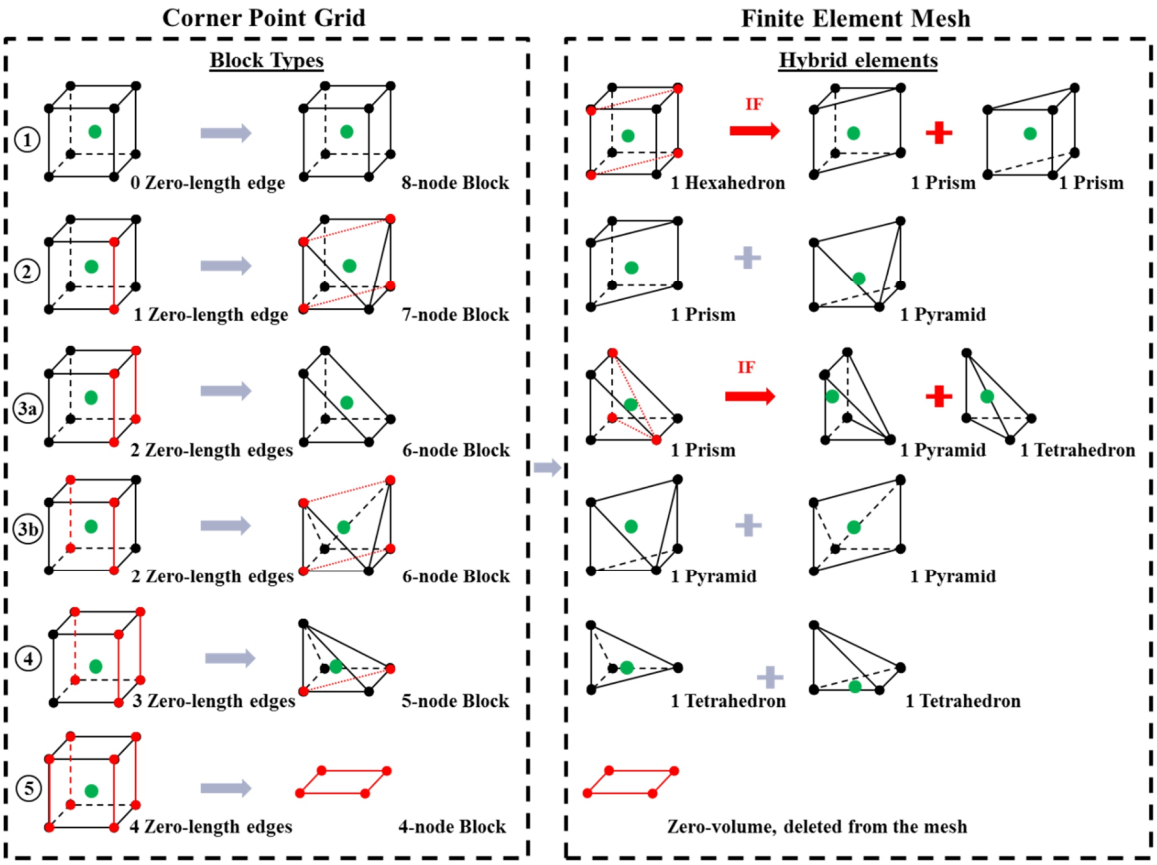

is further partitioned into one pyramid element and one tetrahedron element.

Type 3b: Two opposing vertical edges at opposite faces of the block have zero length. The block is converted to two pyramid elements.

Type 4: Three vertical edges of the block have zero length. The block is partitioned into two tetrahedron elements. If one of the tetrahedrons is formed from the three zero-length edges, it has a volume of zero and thus is removed from the mesh.

Type 5: Four vertical edges of the block have zero length. The block has a volume of zero and is removed from the mesh.

Through the above approach, a corner point grid will be consistently converted to a hybrid FE mesh with multi-type elements, i.e. tetrahedrons, prisms, pyramids and hexahedrons. In case of faulting, the blocks at two sides of a fault will be converted each to hexahedral elements following Type 1. The degenerated blocks at pinch-outs and erosional layers will be converted to tetrahedral, prism and pyramid elements following Type 2 to 5, depending on the exact geometrical setting for each block. The outlined scheme has been implemented into a stand-alone mesh converter, which can be operated under all operating systems. As an additional option, the converting scheme by Aarnes et al. (2008), i.e. partitioning each block into six or less tetrahedrons, has been included as well.

Figure 5.3 Converting schemes between a corner point grid and a FE mesh. Red solid lines represent collapsed edges (zero length) in degenerated blocks; red dashed lines represent partitioning schemes; green dots illustrate transferred property data. The partitioning marked "IF" is only performed if neighboring blocks are partitioned.

5.2.3 Parameter conversion

To parameterize a corner point grid using the property modeling approach (Schlumberger 2014), each geological formation can be considered as individual material and thus a uniform material index is assigned (see Fig. 5.1 where each color indicates a uniform material index). Additionally, based on geostatistical or stochastic methods, heterogeneous property data can be assigned to each block in each formation according to its sedimentation features. The parameter data is stored block-wise for the corner point grid, and therefore the data are transformed block-wise from corner point grids to FE meshes. As shown in Fig. 5.3, the green dots represent the data being transferred. Different parameters are stored as different entities in each individual block. Through block conversion, the elements will inherit the data directly from the blocks from which they are partitioned. The geological group index is always transferred from blocks to elements in order to identify the geological formation the elements belong to. Within a geological formation, i.e. geological group, if heterogeneously distributed parameters exist, they are also transferred from individual blocks to elements.

5.2.4 Well trajectory conversion

Generally, a well trajectory consists of well head, well path and well screen. A set of well head coordinates indicates where the well starts, and a list of block data shows where the well penetrates the grid. In an FE mesh, wells can be represented by a list of nodes (0D geometric feature) or a polyline (1D geometric feature) (Cacace and Blöcher 2015), which are used as locations for source points or boundary conditions for the injection or extraction sections. To make use of well trajectories defined within a corner point grid, a procedure of transferring blocks penetrated by well trajectories to nodes in the FE mesh is required. An approach to identify well nodes in the FE mesh by determining the closest node along the well trajectory is implemented. The well trajectory in Petrel lists the indices of penetrated blocks. It also includes the information on how the well penetrates blocks by listing the intersection points on two block faces, i.e. one entry face and one exit face for each block. On each face, therefore, the distances from the intersection point to the corner nodes attached to this face are evaluated and then apply the following approach to determine which node should be picked to represent the well position (Fig. 5.4). These cases are depicted in Fig. 5.4:

Case 1: On each face, the node with the smallest distance to the intersection point is identified and picked.

Case 2: On one face, the closest node to the intersection point is identified and picked. If, however, on the other face of the same element, more than one node has the same distance to the intersection point, then the distances between the already picked node on the first face and the nodes with identical distances to the intersection point on the other face are calculated, and the node with the closest distance is picked. This procedure ensures that the well path is mapped along vertical edges of blocks as often as possible.

Case 3: On both faces, more than one node has the same distance to the intersection point. This case happens only in geometrically simple settings of synthetic models. In this case, all

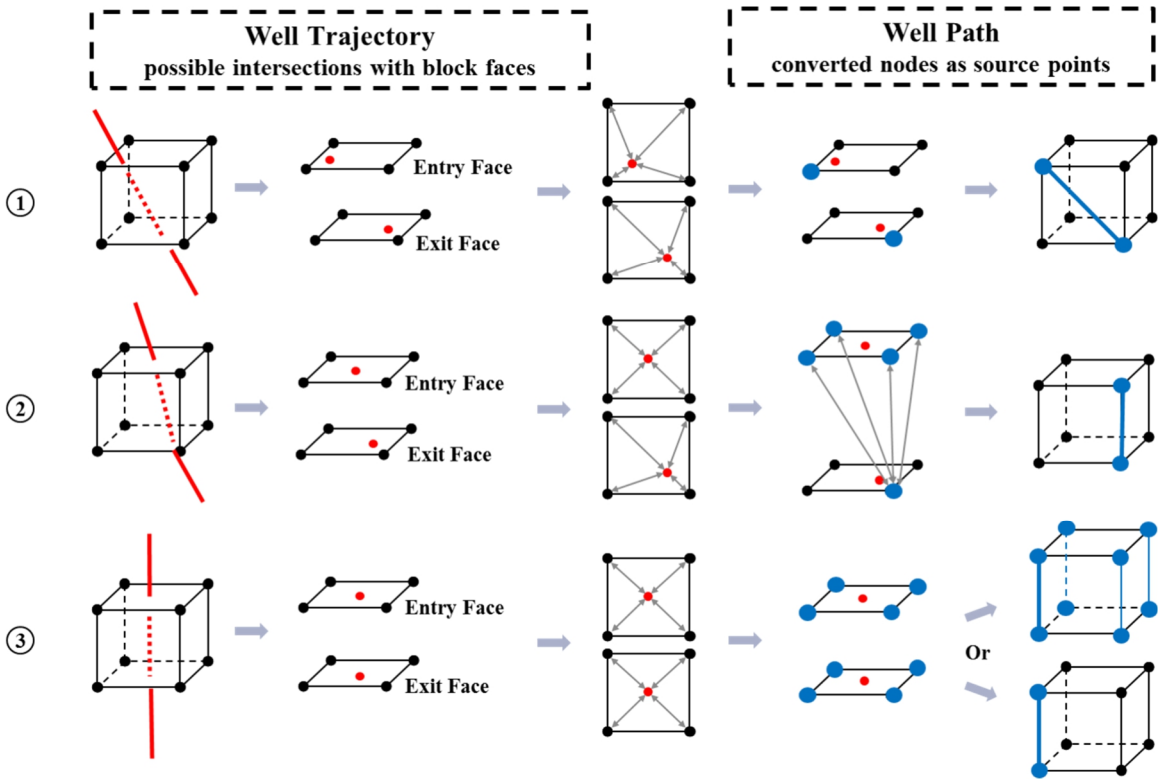

Figure 5.4 Converting schemes of well trajectory. Red lines: well trajectory penetrating blocks; Red dots: intersecting points on the entry and exit faces; Grey arrow lines: distance between the intersecting point to nodes or between two nodes; Blue dots: picked nodes; Blue lines: converted well path.

the nodes with the same distance on the face are picked and each set of two closest nodes between the two faces is considered as a well path. This yields more than one consistent well path for the FE mesh. Either one or more than one of them can be used to locate the well source terms of the dynamic model.

The open-hole section along a well trajectory needs to be modeled as grid property to indicate which penetrated blocks are connected to the open-hole section. The output file of the well trajectory lists this information for each penetrated block, and thus the nodes belonging to those blocks to represent the open-hole section of the designed well trajectory will be picked as described above.

After picking the nodes for the well path and the well open-hole section, the well trajectory is represented as a polyline, i.e. as 1D geometry. The geometrical features of the converted well path and the open-hole sections are written as output for the use of source term or boundary condition placement in the FE based simulators.

5.2.5 Used programs

Petrel

Petrel (version 2014.6) is a commercial software platform providing integrated workflow tools to build static geological reservoir models later used in dynamic reservoir modeling simulators as e.g. ECLIPSE (Schlumberger 2014, 2016). The corner point gridding approach is one of the methods in Petrel to construct geological structural models. The approach provides several output files regarding the corner point grid. The‘*.FGRID’ file contains formatted grid data, e.g. grid dimension, coordinates of corner points and non-

neighbor connections etc. The‘*.INC’ file contains block-wise parameter data. The well trajectory data can be extracted from the well connection file ‘*.WCND’.

OpenGeoSys

OpenGeoSys (OGS) is an open-source, multi-platform finite element based scientific modeling software which can simulate individual or coupled thermo-hydro-mechanical-chemical (THMC) processes in porous and fractured media (Kolditz and Bauer 2004). OpenGeoSys (www.opengeosys.org) has been successfully applied to reservoir simulations concerning geothermal heat extraction (Watanabe et al. 2009; Boockmeyer and Bauer 2014), CO_2 storage (Li et al. 2014; Park et al. 2014), and density driven flow. To perform those reservoir simulations, OGS needs usable FE meshes generated or transferred from other platforms (Kalbacher et al. 2005, 2007; Miles et al. 2007). OGS provides all finite element types utilized in the mesh converter, i.e. hexahedron, prism, pyramid and tetrahedron elements. The ‘*.msh’ file, i.e. FE mesh file, contains a list of nodes with coordinates and a list of elements indicating element type, geological group index and corresponding node topology. The ‘*.gli’ file contains source point nodes indicating well trajectories, and the ‘*.property’ file contains the element-wise property (one file for each property).

Mesh Converter

To transfer from static geological models to FE based dynamic models, the newly implemented mesh converter offers the workflow of converting a corner point grid, parameter data and well trajectories to an FE mesh, element properties and source points. The mesh converter is a stand-alone program, which is written in the object-oriented C++ programming language. As a proof of concept, all the read-in and write-out functions are developed referring to the format of Petrel (version 2014.6) output files and input files required by the OGS simulator. Although those functions are software related, only simple modifications are required to apply the mesh converter to other corner point grids based software and FE based simulators. Additionally, in order to support the coupling between OGS and the ECLIPSE reservoir simulator implemented by Graupner et al. (2011) and Pfeiffer et al. (2016), the mesh converter generates files to list block indices and connectivity information.

The mesh converter has been tested and verified by a series of artificial dedicated but very technical benchmarks and test cases, e.g. geological models containing degenerated blocks like the one shown in Fig. 5.2. The benchmarks and test cases are very technical in nature and therefore not reported here in detail, but the developed methods have proven robust in all these benchmarks and test cases. In the following, an application is presented to model a hypothetical geothermal reservoir operation at a real geological site in Schleswig-Holstein, northern Germany.

5.3 An application to a deep geothermal reservoir operation

To make use of and test the newly developed workflow, a hypothetic scenario of a deep geothermal reservoir operation is numerically simulated at a real geological site in Schleswig-Holstein, northern Germany. A well doublet is applied in a high-permeability saline formation of the middle Rhaetian at about 4000 m depth, in

which the saline water has a temperature of about 160 °C. The well doublet is assured to operate for 6 months a year, and reservoir behavior is simulated for 20 years. During the operation, hot water is extracted at the "warm" extraction well at a rate of 150 m^3/h, while the cooled water is re-injected at the "cold" well at the same pumping rate with a temperature of 40 °C. This scenario is a hypothetical geothermal operation, but the geological site used is real and represents the typical geological complexity encountered during such an operation. It is thus a good test case for the methods developed and presented above, and used here to test and validate the workflow.

The numerical simulation of the geothermal reservoir is carried out by the OGS simulator, which employs a fully coupled model of thermal and hydraulic processes in porous media (www.opengeosys.org). The mathematical models are referring to equations described in section 2.6 but applied for a single phase flow. The coupled thermal and hydraulic processes are solved by a sequential iterative approach in OGS, where the standard Galerkin method is used to spatially discretize the weak forms and an implicit time stepping scheme for time discretization (Wang et al. 2009).

5.3.1 Subsurface geological model

The study site is located near Hamburg, northern Germany, and has a dimension of 17 km × 17 km width and 7 km depth. Sediment ages range from the Rotliegend up to Quaternary, forming a total of 20 geological formations (Fig. 5.5a). Due to the halokinesis of Rotliegend and Zechstein groups, the upraised salt forms a salt dome and intrudes into the overlying sediments from lower Buntsandstein up to the Oligocene. Above the salt dome, there exists a fault system from the Miocene base to the Quaternary base (Baldschuhn et al. 2001).

A static geological model is constructed in Petrel based on geological information on the near surface layers (from Miocene base to Quaternary base) from Scheer et al. (2007), and information on the deep layers (from Zechstein base to Oligocene base) from Hese (2011, 2012), who based his work on the geotectonic atlas of northern Germany (Baldschuhn et al. 2001). Vertical key pillars are used in Petrel to model the geometry of the salt dome and thus form the fault planes around the salt dome. This is because the fault plane is the only geometrical plane which can be vertical or inclined in the pillar gridding approach to represent the geometry of the salt dome walls.

As recommended in Schlumberger (2013), faults are modeled as "zig-zag" type. This helps to maintain the block faces in x- and y- directions as orthogonal as possible. The geological layers intruded by the salt dome are then intersected by the faults and thus show discontinuities across the salt dome. As a result, the salt dome is modeled as a gap in the geological model (Fig. 5.5a). For hydraulic process simulation, this way of geological modelling represents the true nature of the salt dome, which has an extremely low permeability because of highly dense compaction and thus reacts as a barrier for fluids. For heat flow simulations, the salt dome should be modeled as a salt body with a given heat conductivity. Considering the geothermal reservoir in the application example, which is far away from the salt dome, this approximation is acceptable. For

this reason and in order to reduce the computational effort, only the western part of the model up to the salt dome is used for the simulation of the geothermal reservoir operation. According to Reinhold et al. (2011) and Doornenbal and Stevenson

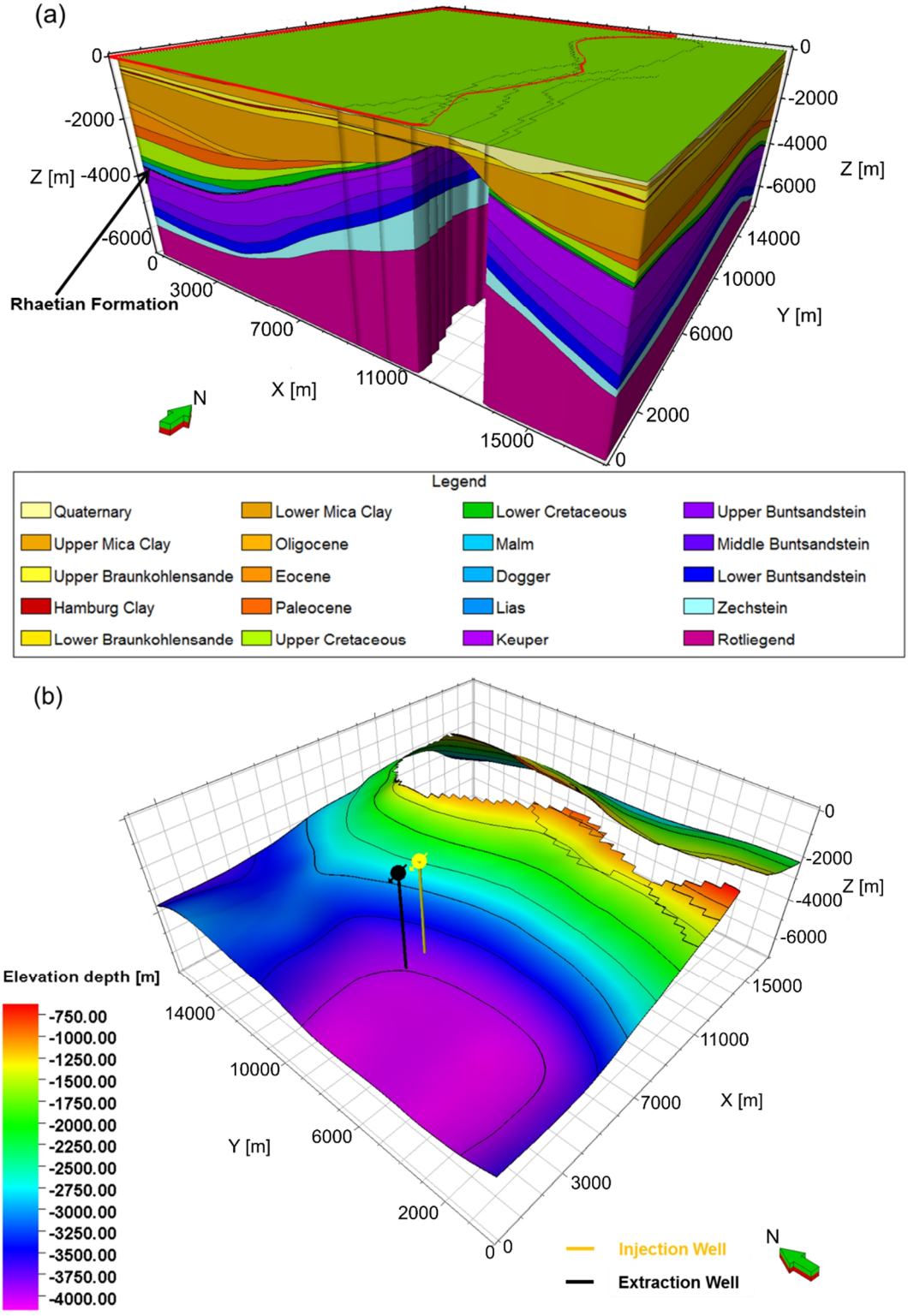

Figure 5.5 The subsurface static geological model. (a) Structural model including 20 geological formations with the red line indicating the extent of the numerical dynamic model region; (b) The Rhaetian formation layer and well doublet location. (Green arrows point north)

(2010), the Rhaetian formation at the upper Triassic in northern Germany is a potential reservoir formation with porous sandstone and barrier shale layers. At the study site, the Rhaetian formation has a depth of about 4000 m at the west flank, which is deep enough to provide a high geothermal potential. Similar to the work of Mottaghy et al. (2010) and Vogt et al. (2013), the west Rhaetian formation is chosen as target formation. Based on the facies description from Hese (2011, 2012), the formation is further subdivided into three layers. The middle Rhaetian is the main sandstone layer with an average thickness of 20 m, and the upper and the lower Rhaetian are hydraulic barrier layers with an average thickness of 15 m each.

At the west side of the geological model, two vertical wells forming a well doublet are placed (Fig. 5.5b). The intersection of the extraction well with the middle Rhaetian formation is from 3963 m to 3983 m depth. To minimize the possible temperature drop in the extraction well, the injection well is placed at 900 m distance, and with an intersection from 3803 m to 3823 m depth. The wells are defined in Petrel and converted to the computational mesh using the newly developed methods explained above. In OpenGeoSys, the wells are geometrically represented by picked nodes, on which point sources are defined.

5.3.2 Model discretization and conversion

For stability and accuracy of the numerical simulation, the geological model within the simulated area is further refined. Along the z-direction, the middle Rhaetian formation is divided into 10 layers with a thickness of 2 m each, and the upper and lower Rhaetian into 5 layers (2×5 m, 2×2 m and 1×1m thickness). Near the middle Rhaetian, the layers have a thickness of 1 m. The other formations are also refined to get an average cell thickness of 100 m in each layer. Horizontally, the area around the well doublet is gradually refined, which means that the model domain within a distance of 150 m from the wells and between the two wells has a resolution of 12.5 m × 12.5 m, from 300 m to 150 m distance the resolution is 25 m × 25 m, from 550 m to 300 m distance the resolution is 50 m × 50 m and from 1050 m to 550 m the resolution is 100 m × 100 m. Beyond this, the model domain maintains a horizontal resolution of 200 m × 200 m as in the original pillar grid.

As a result, the corner point grid of the geological model is discretized into 176 × 123 × 191 blocks (i.e. 4134768 blocks in total). Among them, 2587462 blocks (~ 62.6 %) are active. Each formation in the model is assigned a unique material group index (Table 5.1). For a corner point grid based simulator, e.g. ECLIPSE, which uses a finite difference scheme, the number of degrees of freedom is equivalent to the number of blocks. This corner point grid is then exported from Petrel and converted using the newly developed mesh converter. The conversion is performed successfully, as all occurring geological features are correctly accounted for (see below). The converted hybrid FE mesh (Fig. 5.6a) has 3340336 elements in total, which is about 56.8 % more than the active blocks in the corner point grid, and it has 2619309 nodes, which means the number of degrees of freedom is 1.2 % higher for the FE case. The FE mesh consists of 1818245 hexahedrons (~54.4 %), 1464905 prisms (~43.9 %), 24306 pyramids (~0.7 %) and 32880 tetrahedrons (~1.0 %). As a comparison, the conversion approach by

Table 5.1 Reservoir hydraulic and thermal properties (Mottaghy et al. 2010; Hese 2012; Stober and Bucher 2012).

Geological Formation	Material Group Index	Permeability [mD]	Porosity [-]	Heat capacity [KJ/(m^3·K)]	Heat conductivity [W/(m·K)]	Natural heat generation [μW/m^3]
Quaternary	0	5000	0.40	2100	2.5	0.9
Upper Mica Clay	1	0.1	0.30	2500	2.5	0.9
Upper Braunkohlensande	2	5000	0.35	2100	2.5	0.9
Hamburg Clay	3	0.1	0.30	2500	2.5	0.9
Lower Braunkohlensande	4	1000	0.35	2100	2.5	0.9
Lower Mica Clay	5	0.85	0.30	2500	2.5	0.9
Oligocene	6	0.1	0.20	2500	2.5	0.9
Eocene	7	0.1	0.20	2500	2.5	0.9
Paleocene	8	0.1	0.20	2500	2.5	0.9
Upper Cretaceous	9	1	0.20	2300	2.9	0.9
Lower Cretaceous	10	10	0.20	3000	2.0	0.9
Malm	11	0.1	0.15	2300	1.2	1.4
Dogger	12	500	0.15	2400	1.2	1.4
Lias	13	0.1	0.15	2000	1.5	1.4
Upper Rhaetian	14	0.1	0.15	2000	2.0	1.0
Middle Rhaetian	20	500	0.30	2200	2.2	0.5
Lower Rhaetian	14	0.1	0.15	2000	2.0	1.0
Keuper	14	0.1	0.15	2000	2.0	1.0
Upper Buntsandstein	15	0.1	0.15	1000	2.4	0.7
Middle Buntsandstein	16	10	0.15	2200	2.4	0.7
Lower Buntsandstein	17	0.1	0.10	1000	2.8	1.3
Zechstein	18	0.1	0.10	840	4.5	0.5
Rotliegend	19	0.1	0.10	1000	2.8	1.5

Aarnes et al. (2008) in total yields 12654461 tetrahedrons elements, which is almost four times more than the new approach. By the new approach, the converted elements are mainly hexahedrons and prisms, which helps to maintain a reasonably small number of elements. In FE models, the node number indicates the computational burden when solving the equation system, while the element number is the burden for constructing the equation system and assembling the system matrix. Thus, this reduced element number enables faster dynamic model simulations and also requires less computer storage. The converted Rhaetian formation layer in combination with the well path is shown in Fig. 5.6b.

A closer view of the corner point grid and the converted mesh is shown in Fig. 5.6c and Fig. 5.6d in order to illustrate how the implemented conversion schemes have been applied to the geological model. Here, the upper formation is intruded by the lower one and also eroded. Block A in Fig. 5.6c has only one zero-length edge in the lower right corner and is converted to prism A_1 and pyramid A_2. In block B, two edges have zero length and it is considered as a prism firstly. However, in order to keep consistent faces along the z-direction, it is further cut

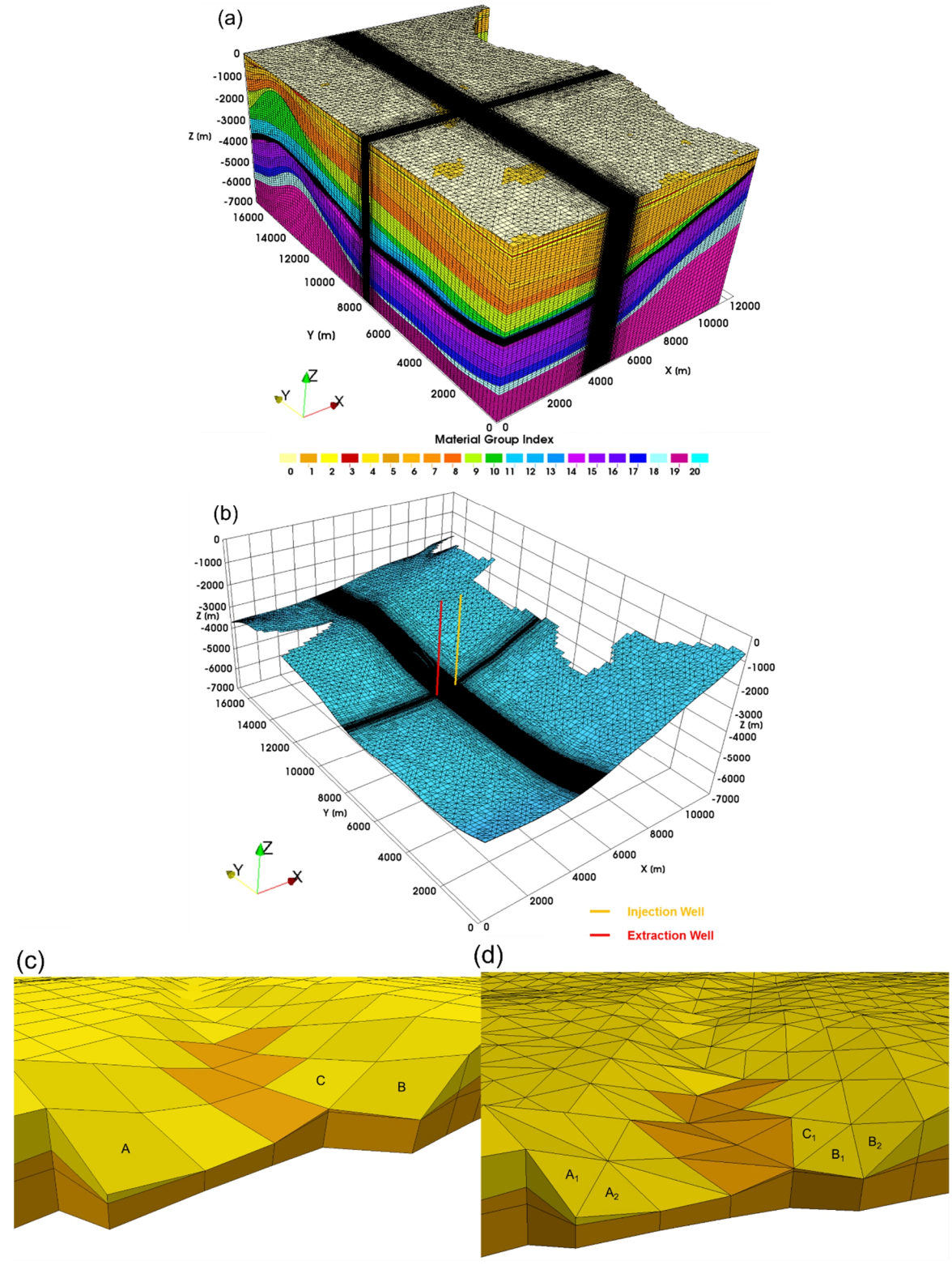

Figure 5.6 Mesh conversion result. (a) Converted mesh with 20 material groups; (b) Converted mesh of the middle Rhaetian formation with two wells; (c) and (d) a closer comparison between the corner point grid and the converted mesh.

to one tetrahedron B_1 and one pyramid B_2. Block C has three zero-length edges, and is converted to two tetrahedrons. Because one tetrahedron inherits the three zero-length edges, it has zero volume and is removed from the mesh. Thus, block C is converted

to only one tetrahedron C_1. As a summary, about 29.7 % of the blocks in the corner point grid are partitioned by the implemented scheme, due to either the existence of degenerations or inconsistencies in joint faces. Therefore, the implemented methods convert the grid with degenerated blocks into the FE mesh with consistent hybrid elements, so the FE mesh is numerically healthy compared with the non-consistent direct conversion approaches. The results (see section 5.3.4 below) from field application of 20 years' geothermal reservoir operation show, that there are not any numerical stability problems, which means that this conversion does not generate numerical instabilities.

5.3.3 Hydraulic and thermal properties

Non-isothermal flow is simulated in the model, and thus the water dynamic viscosity is considered temperature dependent following the simple empirical model presented by Yaws and Gomes (2009). Also, the water density is defined by a linear temperature dependent function according to Busch et al. (1993), in which the reference water density of 1000 kg/m^3 is set at reference temperature of 283.15 K. Salinity effects are not considered here, as salt content in the formation is assumed homogenous. The other hydraulic and thermal properties (Table 5.1) are assumed homogenous in each geological formation. Regarding the thermal properties, the volumetric heat capacity is taken from Stober and Bucher (2012), and the thermal conductivity and natural heat production rate are taken from Mottaghy et al. (2010). The intrinsic permeability and porosity are taken from Scheer (2001), Doornenbal and Stevenson (2010) and Hese (2012). The storage coefficient is estimated based on the empirical function (Freeze and Cherry 1979) related to the compressibility of porous medium and water, which are respectively assumed as 4.5×10^{-10} Pa^{-1} and 5×10^{-10} Pa^{-1}.

5.3.4 Simulation results

In preparation for simulating the geothermal production, the initial reservoir conditions (i.e. initial pressure and temperature fields) have to be determined by two model runs. First, a stationary heat transport model is initialized with a temperature gradient of 30 K/km, and at the top surface (z = 0 m), the temperature is set constant to 10 °C representing the mean annual air temperature. A constant heat flux of 70.5 mW/m^2 (Mottaghy et al. 2010) is applied at the bottom at z = -7000 m and natural heat generation is accounted for (Table 5.1). The resulting temperature field is taken as the initial temperature field for the stationary flow model in the second step. A pressure of one bar is set constant at the top as boundary condition, and the pressure field is initialized with a gradient of 9810 Pa/m. The resulting temperature versus depth profile corresponds well with the measured temperature profiles from Mottaghy et al. (2010), which are from the same area. This shows that the parametrization of the model is realistic, and temperatures correspond to real temperatures at respective depths (Fuchs and Förster 2010; Agemar et al. 2012; Suchi et al. 2014). The temperature in the reservoir formation at the extraction well in 3980 m depth is 162.4 °C, in 3000 m depth 116.2 °C. These temperatures show that a geothermal use could be feasible.

The pressure and temperature fields described above are used as the initial

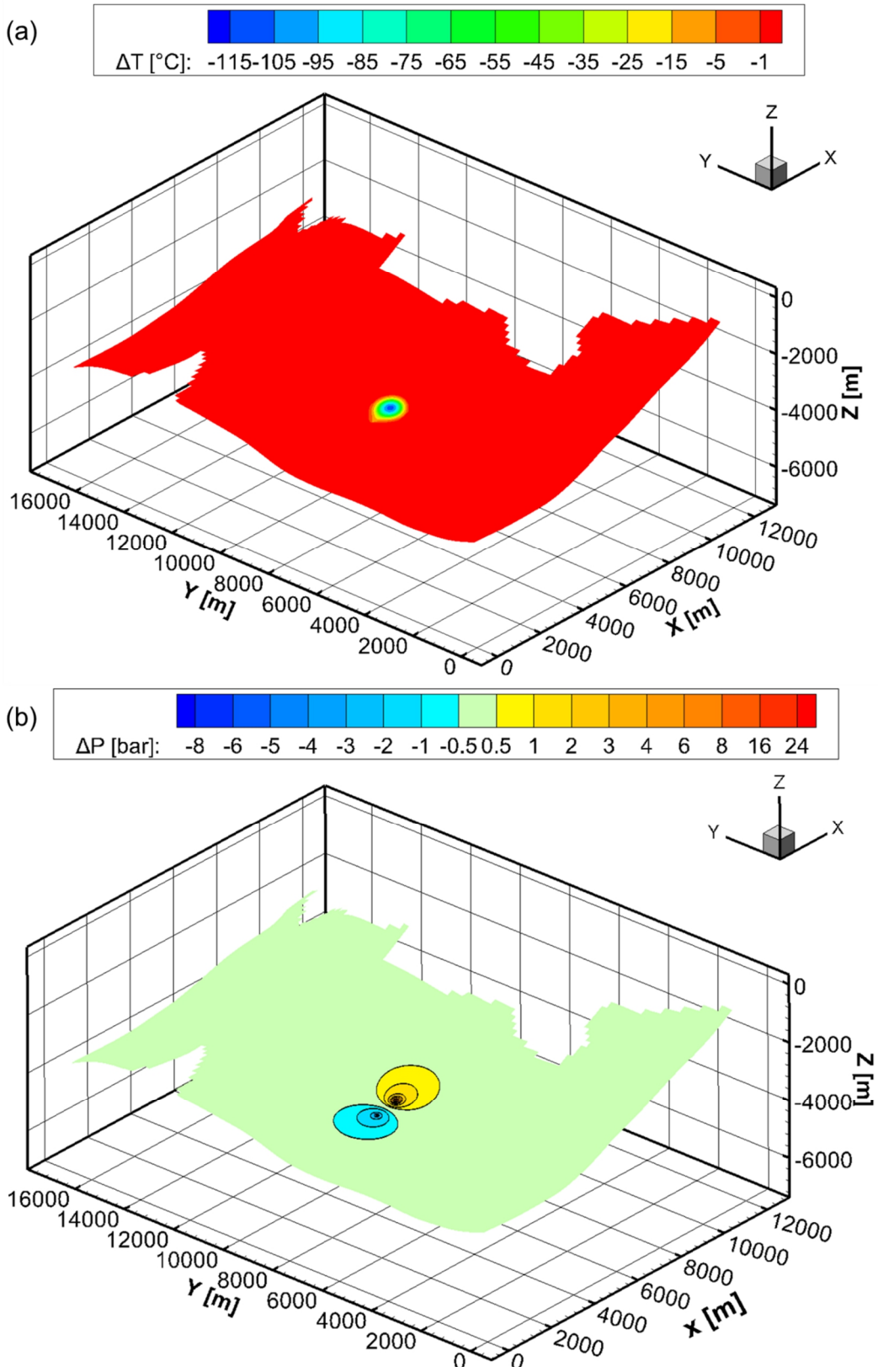

Figure 5.7(a) Temperature changes in the middle Rhaetian formation after 20 years; (b) Pressure changes after the injection in the last cycle.

conditions for the transient model. Another Dirichlet boundary condition is added for the heat transport process, which is a constant temperature of 40 °C along the

injection well in the Middle Rhaetian to represent the temperature of injected water. This boundary condition is only applied when water is injected. For simulating pressure, the model boundary at the side of the salt dome is considered a no flow boundary, and the other three sides are open boundaries which maintain the initial water pressure. Due to the low permeability in the upper and lower Rhaetian formations, these are barrier formations and can prevent the water being displaced to neighboring layers. Accordingly, water flow is simulated only for the middle Rhaetian formation, while heat transport is simulated in the whole model domain. For the injection well, an injection rate of 150 m^3/h is distributed to the nodes along the open section of the well path generated using the new converter and at the extraction well a rate of -150 m^3/h is assigned accordingly. The total simulation time is set to 20 years, and within each year, the well doublet operates only for six consecutive months.

The complete model is simulated as shown in Fig. 5.6a. Because the application interest, i.e. the geothermal reservoir, is the porous formation in the sandstone layer of the middle Rhaetian, the model results here only show the temperature and pressure changes in the Rhaetian formation. The temperature perturbation in the Rhaetian formation after 20 years is shown in Fig. 5.7a. A temperature decrease of 1 °C or larger is observed within 900 m of the injection well showing a radial transport of injected water and heat away from the injection well. At the injection well, temperature drops by 111 °C to 44 °C. Fig. 5.7b shows the pressure response at the end of the six-month operation period in the last year of the simulation. Pressure changes of up to 24 bar and 8 bar are observed at the bottom of the injection and the extraction wells, respectively. At roughly 1.5 km away from the center of both wells, pressure response is 1 bar. In contrast to the temperature distribution, the pressure has a larger region of impact and the pressure change caused by the injection is larger than the pressure change caused by the extraction. This is due to reservoir cooling near the injection well, as water viscosity is increased there and thus increases flow resistance, which leads to a larger pressure change.

A closer view of the temperature changes after 20 years at the well doublet is shown in Fig. 5.8. The cold-water front propagates away from the injection well (Fig. 5.8a) and preferentially moves towards the extraction well following the steepest hydrological gradient. At the injection well, temperature drops to 44 °C and leads to a temperature decrease of 111 °C. The temperature perturbation in the x-y plane (Fig. 5.8b) shows a temperature decrease of 1 °C at a distance of about 900 m away from the injection well. In the x-z plane (Fig. 5.8c), the temperature also changes above and below the reservoir formation due to heat conduction, and a decrease of 1°C is observed at a distance of roughly 90 m. The temperature profile at the bottom of the extraction well is recorded over 20 years (Fig. 5.8d). The overall temperature decrease is 1.5 °C, and a relatively faster drop of 1 °C is within the last eight years, indicating interference with the advancing cold water front. Overall, water with an average temperature of 161.7 °C at a rate of 150 m^3/h is produced for six months in each year. This corresponds to an energy production rate of 21.2 MW, considering a 40 °C reinjection temperature. Over

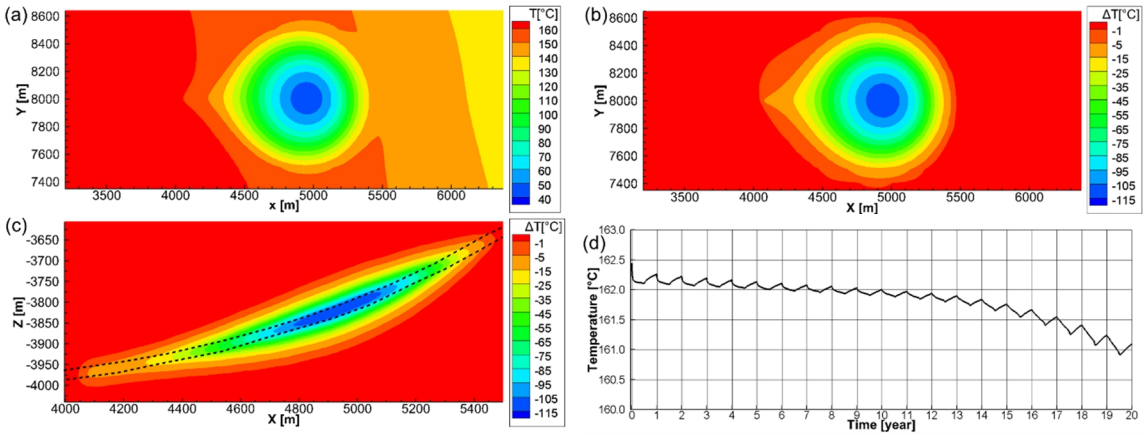

Figure 5.8 (a) Temperature distribution near the well doublet in the x-y plane; Temperature change near the well doublet in the x-y (b) and the x-z planes (c), where the black dashed line indicates the reservoir formation; (d) Temperature profile at the bottom of the extraction well.

20 years, this corresponds to 1854 GWh of produced thermal energy.

5.4 Summary and discussion

In order to investigate possible uses of the geological subsurface and their potential impacts, scenario simulations have to be conducted on the basis of complex static geological models representing the real geological system. A workflow is developed to transfer complex heterogeneous geological models to consistent FE models. Three functionalities have been implemented. First, a corner point grid is consistently converted accounting for the individual block situation, and providing a hybrid FE mesh containing elements of hexahedron, prism, pyramid and tetrahedron type. Secondly, the heterogeneous properties of the corner point grid are transferred from individual blocks to corresponding elements. Third, well trajectories can be mapped to the nodes or later formed as polylines in the FE mesh and used as source terms. The methods were tested extensively and verified in a series of technical test cases.

Instead of remeshing or reconstructing approaches (e.g. Blöcher et al. 2010a; Zehner et al. 2015), the implemented methods can be straightforwardly applied to convert existing corner point grids based on geological models to FE meshes for dynamic models. Besides, this direct conversion from blocks to elements allows for consistency when transferring spatially heterogeneous material properties, which avoids to reparametrize the converted FE models. This approach additionally provides the possibility to couple the commercial Eclipse simulator with OpenGeoSys (Pfeiffer et al. 2016) and especially to simulate induced geochemical impacts in the use of subsurface. Among the existing direct conversion approaches (e.g. Graupner et al. 2011; Ni and Chen 2014; Park et al. 2014), which handle only hexahedral blocks, the method presented here accounts for all kinds of degenerated blocks and allows to construct a consistent FE mesh. In order to reduce element numbers in converted FE mesh and achieve a higher efficiency in running time, all FE element types are used instead of only tetrahedrons (Aarnes et al. 2008).

Although the direct conversion methods presented here are comparatively fast, they come with some drawbacks because the

geological models cannot be changed or modified during the conversion. The discretization and parameterization of the geological model must be finalized before the conversion, already including all requirements from the process simulation like the grid refinement near the injection and extraction wells in the demonstrated application due to numerical reasons. If, for example, during process simulations it is found that a finer mesh is required due to numerical reasons, the mesh has to be changed in the geological model and the conversion process repeated. However, only the mesh has to be adapted, not the geological structure or parametrization. This repeated conversion is why an automated and fast conversion method is required. The quality of the converted mesh highly depends on the quality of the input corner point grid, which should be checked for, e.g. zero-volume elements, using functionality provided by the meshing tool Petrel after discretizing the geological models. Comparing this method to the remeshing or the reconstructing approach, the representation of geological complexities in the converted mesh is restricted by the possibilities of representation in the original corner point grid. For example, subgrid fracture networks cannot be modeled geometrically but only as grid properties, and can thus not be integrated explicitly in the converted mesh. Besides, although the non-neighbor blocks at two sides of the fault slip is consistently converted to the hexahedral elements, the fault slip appears inevitably as hanging nodes in the converted mesh, which might not be compatible with some FE simulators. If these features are of importance, the alternative methods have to be employed.

To demonstrate the application of the implemented workflow, a scenario study is performed on a geothermal reservoir operation in northern Germany. A static geological model was built for the study site using Petrel. The resulting model comprises 20 geological formations of different materials combined with one salt dome structure and several faults, which are discretized into 2587462 active blocks in its corner point grid. For the grid conversion to an FE mesh, about 29.7 % of the grid blocks needed to be partitioned due to the existence of degenerations. The conversion resulted in a hybrid FE mesh with 3340336 elements, including 54.4 % of hexahedrons, 43.9 % of prisms, 0.7 % of pyramids and 1.0 % of tetrahedrons. The mesh has roughly a quarter of the elements compared with the method of Aarnes et al. (2008), which is the only consistent method given in literature so far. This reduced element number enables faster dynamic model simulations and also requires less computer storage. In order to differentiate geological formations in the FE mesh, a material index has been transferred as property data. Also, the trajectories of a well doublet were mapped from Petrel to the nodes of the FE mesh. This allows for an accurate placement of the wells, consistent with the geological model. The converted FE model was then simulated by OGS in a coupled heat transport and water flow model. The simulation demonstrates that the converted FE mesh can be employed for the required dynamic simulation, allowing for stable numerical results. The dynamic model can be used to dimension the heat retrieval well doublet system and give estimates of induced effects.

Besides this application shown here, the presented methods can also be applied, for

instance, to investigate oil and gas recovery, underground storage of natural gas, hydrogen and compressed air, and brine disposal in deep saline porous formations. Although Petrel, for which the conversion methods were implemented in the work presented here, is a commercial tool, it is widely used and provides suitable functionality for representing subsurface structures, which can by this method be made use of for numerical process simulations. However, the presented methods are not restricted to operate only with this software for OGS, but, with straightforward modifications of the input and output functions, they can be generally employed for converting any type of corner point grid based geological models to any FE models format for other geological modeling and numerical simulation codes.

6 Conclusions

With the rapid growth of energy production from intermittent renewable sources like wind and solar power plants, large-scale energy storage options are required to compensate for fluctuating power generation on different time scales. Compressed air energy storage (CAES) in porous formations is seen as a promising underground storage option for balancing diurnal fluctuations. CAES is a power-to-power energy storage, in which electricity is converted to mechanical energy, i.e. highly pressurized air, and stored in the subsurface. Using scenario based numerical simulations, several aspects of a realistic large-scale CAES operation scenario using a typical anticline structure in the North German Basin are studied in this thesis, including an investigation of feasibility in terms of reservoir behavior, a dimensioning of storage rates and storage capacity, and an assessment of induced thermal, hydraulic and geochemical impacts. The major findings and conclusions of this thesis are:

- A realistic and representative scenario of large-scale CAES operation in porous formations is developed by defining and quantifying the four fundamental components required in such a storage facility, which are the specifics of gas turbine, storage formation, operating schedule, and well configuration. The minimum operation pressure and the air mass flow rate required at the gas turbine inlet determine the potential power output, and thus are the critical parameters defining the required depth of the porous formation and the minimum hydraulic permeability required. Therefore, depending on the operating schedule, individual requirements for the porous storage formation can be derived.
- Scenario based numerical simulations show that this CAES operation is technically feasible using a typical anticline structure from the North German Basin. The estimated storage capacity can support up to 9.6 hours of continuous power output of 321 MW. The maximum power output is higher at 484 MW within the first 30 minutes. A sensitivity analysis shows that the well number required to reach this storage capacity is strongly affected by the formation permeability, with low permeability requiring higher well numbers. However, due to well interference, this relationship is non-linear and depends on the detailed geometric set-up of the wells in the porous formation. For low-permeability reservoirs, besides, using horizontal wells can reduce the required well number because their longer well screen length. Therefore, a site-specific assessment of porous formation and well configuration is required for each CAES operation.
- During the initial fill of this large-scale CAES operation, an induced pressure build-up of more than one bar is found laterally to extend on the kilometer-scale, and depends on the lateral

geological boundary conditions. If open boundary conditions can be assumed, pressure can laterally dissipate over large distances leading to a continuous pressure decrease in the storage reservoir regardless of the cyclic operation after the initial fill. Since the cycled air volume during the storage operation is much smaller than the initially filled air volume, the induced pressure response by the cyclic operation is much smaller and will be typically observed within the gas reservoir.

- Assuming the injected air temperature being close to the average reservoir temperature, the induced thermal impact as temperature change in the storage formation is found to be only on the order of a few degrees centigrade. During the initial fill, the temperature change can only be observed in the vicinity of gas wells, but after several years of the cyclic storage operation, a cumulative temperature decrease of a few degrees centigrade is found further away from gas wells in the storage formation due to the Joule-Thompson effect.
- The loss of oxygen in the stored air is found to be very small during one storage cycle, i.e. twelve hours residence time in the storage formation. This minor loss does not affect the flammability of the stored air when mixed with natural gas and thus will not influence the cyclic operation of the CAES. For longer residence times, the oxygen mole fraction may be reduced by geochemical reactions. This slightly lowers the reservoir pressure, thus reducing the power output. For very long residence times on the order of years, the oxygen content may even drop below the minimum oxygen concentration required for flame propagation. This stored air cannot be used for burning natural gas directly, and the risk of operating failure without an intermediary refill occurs. Thus an adiabatic CAES may be a preferable option for porous formation CAES, as heat gained during air compression is stored and can be used to heat the extracted air during expansion, instead of burning natural gas.
- Due to induced geochemical reactions, it is found that the pH of the formation fluid may drop significantly near the gas wells, even to values below 1.0. The acidified fluid increases the risks of well corrosion and should be considered when selecting the casing material of the gas wells. The induced dissolution and precipitation of minerals results only in a minor increase of porosity and permeability, which will not affect the storage performance in terms of well deliverability. Sensitivity analysis show that the uncertainties in mineral assemblage, mineral reactive surface area and pyrite oxidation kinetic strongly affect the rate of oxygen reduction and fluid acidification. Analysis of these parameters of the reservoir mineral phases from the target location, especially for pyrite, are therefore required for a reliable estimate of possible induced geochemical reactions and impacts.
- As the dimensions of storage capacities and achievable storage rates require a detailed geometric representation of the formation geometry and the well configuration due to well interference, both static geological models representing the complex geological formations and dynamic models

simulating the subsurface flow and transport processes need to be combined for a site-specific evaluations. A workflow is thus developed for transferring complex static geological models to consistent finite element based models used for dynamic models, allowing the assessment of using the geologic subsurface in energy storage applications. The presented application demonstrates the robustness and applicability of the newly developed conversion workflow and the suitability of the converted mesh for dynamic finite element reservoir model simulations.

References

Aarnes JE, Krogstad S, Lie K-A (2008) Multiscale mixed/mimetic methods on corner-point grids. Computational Geosciences 12:297–315. doi: 10.1007/s10596-007-9072-8

Agemar T, Schellschmidt R, Schulz R (2012) Subsurface temperature distribution in Germany. Geothermics 44:65–77. doi: 10.1016/j.geothermics.2012.07.002

al Hagrey SA, Schäfer D, Köhn D, et al (2016) Monitoring gas leakages simulated in a near surface aquifer of the Ellerbek paleo-channel. Environmental Earth Sciences 75:1083. doi: 10.1007/s12665-016-5784-1

Altmaier M, Brendler V, Bube C, et al (2011) THEREDA. Thermodynamic Reference Database.Final Report, GRS-265.

André L, Azaroual M, Bernstone C, Wittek A (2015) Modeling the Geochemical Impact of an Injection of CO_2 and Associated Reactive Impurities (SO_2 and O_2) into a Saline Reservoir. Transport in Porous Media 108:185–205. doi: 10.1007/s11242-014-0359-7

ANR Storage Company (1990) Compressed-air energy storage: Pittsfield aquifer field test; Test data: engineering analysis and evaluation. Detroit, Michigan

Appelo C, Postma D (2005) Geochemistry, Groundwater and Pollution, Second Edition. Taylor & Francis

Baghooee H, Riazi M, Varzandeh F (2014) Optimized Gas Injection Rate for Underground Gas Storage; Sensitivity Analysis of Reservoir and Well Properties.

Baldschuhn R, Binot F, Fleig S, Kockel F (2001) Geotektonischer Atlas von Nordwest-Deutschland und dem-deutschen Nordsee-Sektor. Schweizerbart Science Publishers, Stuttgart, Germany

Ball DA, Fischer RD, Hodgett D (1983) Design methods for ground-source heat pumps.

Bary A, Crotogino F, Prevedel B, et al (2002) Storing Natural Gas Underground. Oilfield Review - Schlumberger 14:16.

Bauer S, Beyer C, Dethlefsen F, et al (2013) Impacts of the use of the geological subsurface for energy storage: an investigation concept. Environmental Earth Sciences 70:3935–3943. doi: 10.1007/s12665-013-2883-0

Bauer S, Class H, Ebert M, et al (2012) Modeling, parameterization and evaluation of monitoring methods for CO_2 storage in deep saline formations: the CO_2-MoPa project. Environ Earth Sci 67:351–367. doi: 10.1007/s12665-012-1707-y

Bauer S, Pfeiffer T, Boockmeyer A, et al (2015) Quantifying Induced Effects of Subsurface Renewable Energy Storage. Energy Procedia 76:633–641. doi: 10.1016/j.egypro.2015.07.885

Bear J (2013) Dynamics of fluids in porous media. Courier Corporation

Bear J, Bachmat Y (1990) Introduction to modeling of transport phenomena in porous media. Kluwer Academic Publishers, AA Dordrecht, The Netherlands

Beckingham LE, Mitnick EH, Steefel CI, et al (2016) Evaluation of mineral reactive surface area estimates for prediction of reactivity of a multi-mineral sediment. Geochimica et Cosmochimica Acta 188:310–329. doi: 10.1016/j.gca.2016.05.040

Benisch K (2018) Assessment and monitoring of hydraulic and geomechanical processes during deep geological CO_2 storage. PhD Thesis, University of Kiel, Germany

Benisch K, Bauer S (2013) Short- and long-term regional pressure build-up during CO_2 injection and its applicability for site monitoring. International Journal of Greenhouse Gas Control 19:220–233. doi: 10.1016/j.ijggc.2013.09.002

Benisch K, Köhn D, al Hagrey S, et al (2015) A combined seismic and geoelectrical monitoring approach for CO_2 storage using a synthetic field site. Environmental Earth Sciences 73:3077–3094. doi: 10.1007/s12665-014-3603-0

Berta M, Dethlefsen F, Ebert M, et al (2016) Surface passivation model explains pyrite oxidation kinetics in column experiments with up to 11 bars $p(O_2)$. Environmental Earth Sciences 75:1175. doi: 10.1007/s12665-016-5985-7

Beyer C, Li D, De Lucia M, et al (2012) Modelling CO2-induced fluid--rock interactions in the Altensalzwedel gas reservoir. Part II: coupled reactive transport simulation. Environmental Earth Sciences 67:573–588. doi: 10.1007/s12665-012-1684-1

Bigham JM, Schwertmann U, Traina SJ, et al (1996) Schwertmannite and the chemical modeling of iron in acid sulfate waters. Geochimica et Cosmochimica Acta 60:2111–2121. doi: 10.1016/0016-7037(96)00091-9

Blöcher MG, Cacace M, Lewerenz B, Zimmermann G (2010a) Three dimensional modelling of fractured and faulted reservoirs: Framework and implementation. Chemie der Erde - Geochemistry 70:145–153. doi: 10.1016/j.chemer.2010.05.014

Blöcher MG, Zimmermann G, Moeck I, et al (2010b) 3D numerical modeling of hydrothermal

processes during the lifetime of a deep geothermal reservoir. Geofluids 10:406–421. doi: 10.1111/j.1468-8123.2010.00284.x

BMWi - Federal Ministry for Economic Affairs and Energy (2015) Making a success of the energy transition. Berlin, Germany

Boockmeyer A, Bauer S (2014) High-temperature heat storage in geological media: high-resolution simulation of near-borehole processes. Géotechnique Letters 4:151–156. doi: 10.1680/geolett.13.00060

Boockmeyer A, Bauer S (2016) Efficient simulation of multiple borehole heat exchanger storage sites. Environmental Earth Sciences 75:1021. doi: 10.1007/s12665-016-5773-4

Bourg IC, Beckingham LE, DePaolo DJ (2015) The Nanoscale Basis of CO_2 Trapping for Geologic Storage. Environ Sci Technol Lett 49:10265–10284. doi: 10.1021/acs.est.5b03003

Bräutigam A, Rothacher T, Staubitz H, Trost R (2017) The Energy Storage Market in Germany Small-scale Battery Systems.

Brookfield AE, Blowes DW, Mayer KU (2006) Integration of field measurements and reactive transport modelling to evaluate contaminant transport at a sulfide mine tailings impoundment. Journal of Contaminant Hydrology 88:1–22. doi: 10.1016/j.jconhyd.2006.05.007

Brooks R, Corey A (1964) Hydraulic properties of porous media. Hydrology Papers, Colorado State University 3:37 pp.

Budt M, Wolf D, Span R, Yan J (2016) A review on compressed air energy storage: Basic principles, past milestones and recent developments. Applied Energy 170:250–268. doi: 10.1016/j.apenergy.2016.02.108

Bundesnetzagentur (Bundesnetzagentur für Elektrizität, Gas, Telekommunikation P und EB (2015) Monitoringbericht. Bonn, Deutschland

Busch K, Luckner L, Tiemer K (1993) Geohydraulik, Lehrbuch der Hydrogeologie. Gebrüder Borntraeger, Berlin, Germany

Buschbach TC, Bond DC (1974) Underground storage of natural gas in Illinois, 1973.

Cacace M, Blöcher G (2015) MeshIt-a software for three dimensional volumetric meshing of complex faulted reservoirs. Environmental Earth Sciences 74:5191–5209. doi: 10.1007/s12665-015-4537-x

Cacace M, Blöcher G, Watanabe N, et al (2013) Modelling of fractured carbonate reservoirs: outline of a novel technique via a case study from the Molasse Basin, southern Bavaria, Germany. Environmental Earth Sciences 70:3585–3602. doi: 10.1007/s12665-013-2402-3

Cantucci B, Montegrossi G, Vaselli O, et al (2009) Geochemical modeling of CO_2 storage in deep reservoirs: The Weyburn Project (Canada) case study. Chemical Geology 265:181–197. doi: 10.1016/j.chemgeo.2008.12.029

Carden PO, Paterson L (1979) Physical, chemical and energy aspects of underground hydrogen storage. International Journal of Hydrogen Energy 4:559–569.

Çengel YA, Boles MA (2011) Thermodynamics: an engineering approach (seventh edition), 7th edn. McGraw-Hill, Boston

Chandra AP, Gerson AR (2010) The mechanisms of pyrite oxidation and leaching: A fundamental perspective. Surface Science Reports 65:293–315. doi: 10.1016/j.surfrep.2010.08.003

Cheviakov AF (2007) GeM software package for computation of symmetries and conservation laws of differential equations. Computer physics communications 176:48–61.

China's National Development and Reform Commission (2016) 13th Five-Year-Plan of Renewable Energy Development in China. Beijing

Cihan A, Birkholzer JT, Zhou Q (2013) Pressure buildup and brine migration during CO_2 storage in multilayered aquifers. Groundwater 51:252–267.

Cohen MD, Flagan RC, Seinfeld JH (1987) Studies of concentrated electrolyte solutions using the electrodynamic balance. 1. Water activities for single-electrolyte solutions. The Journal of Physical Chemistry 91:4563–4574. doi: 10.1021/j100301a029

Cornell RM, Schwertmann U (2003) Formation. In: The Iron Oxides. Wiley-VCH Verlag GmbH & Co. KGaA, Weinheim, FRG, pp 345–364

Crotogino F, Mohmeyer K-U, Scharf R (2001) Huntorf CAES: More than 20 Years of Successful Operation. In: Solution Mining Research Institute (SMRI) Spring Meeting. Orlando, Florida, USA, pp 351–357

Delfs J-O, Nordbeck J, Bauer S (2016) Upward brine migration resulting from pressure increases in a layered subsurface system. Environmental Earth Sciences 75:1441. doi: 10.1007/s12665-016-6245-6

Dethlefsen F, Ebert M, Dahmke A (2014) A geological database for parameterization in numerical modeling of subsurface storage in northern Germany. Environmental Earth Sciences 71:2227–2244. doi: 10.1007/s12665-013-2627-1

Doornenbal H, Stevenson A (2010) Petroleum geological atlas of the Southern Permian Basin area. EAGE, Houten, the Netherlands

E.ON SE (2016) Kraftwerk Huntorf. http://www.eon.com/de/ueber-uns/struktur/asset-finder/huntorf-power-station.html. Accessed 17 Feb 2016

European Commission (2015) Renewable energy progress report. Brussels

Evans DJ, Chadwick RA (2009) Underground gas storage: Worldwide experiences and future development in the UK and Europe. Geological Society of London,

Fischer T, Naumov D, Sattler S, et al (2015) GO2OGS 1.0: a versatile workflow to integrate complex geological information with fault data into numerical simulation models. Geoscientific Model Development 8:3681–3694. doi: 10.5194/gmd-8-3681-2015

Flemisch B, Darcis M, Erbertseder K, et al (2011) DuMux: DUNE for multi-{phase, component, scale, physics,…} flow and transport in porous media. Advances in Water Resources 34:1102–1112.

Franco A, Vaccaro M (2014) Numerical simulation of geothermal reservoirs for the sustainable design of energy plants: A review. Renewable and Sustainable Energy Reviews 30:987–1002. doi: 10.1016/j.rser.2013.11.041

Freeze R, Cherry J (1979) Groundwater. Prentice-Hall, Inc., New Jersey

Fuchs S, Förster A (2010) Rock thermal conductivity of Mesozoic geothermal aquifers in the Northeast German Basin. Chemie der Erde - Geochemistry 70:13–22. doi: 10.1016/j.chemer.2010.05.010

Gaus I, Azaroual M, Czernichowski-Lauriol I (2005) Reactive transport modelling of the impact of CO_2 injection on the clayey cap rock at Sleipner (North Sea). Chemical Geology 217:319–337. doi: 10.1016/j.chemgeo.2004.12.016

Goudar C, Sonnad J (2008) Comparison of the iterative approximations of the Colebrook-White equation: Here's a review of other formulas and a mathematically exact formulation that.

Graupner BJ, Li D, Bauer S (2011) The coupled simulator ECLIPSE–OpenGeoSys for the simulation of CO_2 storage in saline formations. Energy Procedia 4:3794–3800. doi: 10.1016/j.egypro.2011.02.314

Guo C, Pan L, Zhang K, et al (2016) Comparison of compressed air energy storage process in aquifers and caverns based on the Huntorf CAES plant. Applied Energy 181:342–356. doi: 10.1016/j.apenergy.2016.08.105

Hagoort J (1988) Fundamentals of gas reservoir engineering. Elsevier Science Publishers B.V., Amserdam, The Netherlands

Hartmann N, Vöhringer O, Kruck C, Eltrop L (2012) Simulation and analysis of different adiabatic Compressed Air Energy Storage plant configurations. Applied Energy 93:541–548. doi: 10.1016/j.apenergy.2011.12.007

He W, Beyer C, Fleckenstein JH, et al (2015) A parallelization scheme to simulate reactive transport in the subsurface environment with OGS#IPhreeqc 5.5.7-3.1.2. Geoscientific Model Development 8:3333–3348. doi: 10.5194/gmd-8-3333-2015

Helmig R (1997) Multiphase Flow and Transport Processes in the Subsurface. Springer Berlin Heidelberg, Berlin, Heidelberg

Hese F (2011) Geologische 3D-Modelle des Untergrundes Schleswig-Holsteins – ein Beitrag für Potenzialstudien zur Nutzung von tiefen salinen Aquiferen. Zeitschrift der Deutschen Gesellschaft für Geowissenschaften 162:389–404. doi: 10.1127/1860-1804/2011/0162-0389

Hese F (2012) 3D Modellierungen und Visualisierung von Untergrundstrukturen für die Nutzung des unterirdischen Raumes in Schleswig-Holstein. PhD Thesis, University of Kiel, Germany

Heusermann S, Rolfs O, Schmidt U (2003) Nonlinear finite-element analysis of solution mined storage caverns in rock salt using the LUBBY2 constitutive model. Computers and Structures 81:629–638. doi: 10.1016/S0045-7949(02)00415-7

Hoffeins H (1994) Huntorf Air Storage Gas Turbine Power Plant. Energy Supply - Brown Boveri Mittelungen

Hoffeins H, Mohmeyer K-U (1986) Operating experience with the Huntorf air-storage gas turbine power station. Brown Boveri Mittelungen 73:297–305.

Huminicki DMC, Rimstidt JD (2009) Iron oxyhydroxide coating of pyrite for acid mine drainage control. Applied Geochemistry 24:1626–1634. doi: 10.1016/j.apgeochem.2009.04.032

Ibrahim H, Younès R, Ilinca A, et al (2010) Study and design of a hybrid wind-diesel-compressed air energy storage system for remote areas. Applied Energy 87:1749–1762. doi: 10.1016/j.apenergy.2009.10.017

IGU/WOC (2006) Underground storage of gas. Amserdam, The Netherlands

INAP (2012) Global Acid Rock Drainage Guide , INAP: The International Network for Acid Prevention.

Intergovernmental Panel on Climate Change (IPCC) (2014) Climate Change 2014 Mitigation of Climate Change. Cambridge University Press, Cambridge

Joule JP, Thomson W (1854) On the Thermal Effects of Fluids in Motion. Part II. Philosophical Transactions of the Royal Society of London 144:321–364. doi: 10.1098/rstl.1854.0016

Jung HB, Um W, Cantrell KJ (2013) Effect of oxygen co-injected with carbon dioxide on Gothic shale caprock-CO_2-brine interaction during geologic carbon sequestration. Chemical Geology 354:1–14. doi: 10.1016/j.chemgeo.2013.06.019

Kabuth A, Dahmke A, Beyer C, et al (2017) Energy

storage in the geological subsurface: dimensioning, risk analysis and spatial planning: the ANGUS+ project. Environmental Earth Sciences 76:23. doi: 10.1007/s12665-016-6319-5

Kadoya K, Matsunaga N, Nagashima A (1985) Viscosity and thermal conductivity of dry air in the gaseous phase. Phys Chem Ref Data 14:947–970.

Kalbacher T, Mettier R, McDermott C, et al (2007) Geometric modelling and object-oriented software concepts applied to a heterogeneous fractured network from the Grimsel rock laboratory. Computational Geosciences 11:9–26. doi: 10.1007/s10596-006-9032-8

Kalbacher T, Wang W, McDermott C, et al (2005) Development and application of a CAD interface for fractured rock. Environmental Geology 47:1017–1027. doi: 10.1007/s00254-005-1236-z

Katz D (1959) Handbook of natural gas engineering. McGraw-Hill

Kaye G, Laby T (2016) Tables of physical and chemical constants (16th edition). 3.5 Critical constants and second virial coefficients of gases, Kaye & Laby Online, v1.0. www.kayelaby.npl.co.uk. Accessed 28 Mar 2016

Kepplinger J, Crotogino F, Donadei S, Wohlers M (2011) Present trends in compressed air energy and hydrogen storage in Germany. In: SMRI Fall 2011 Technical Conference. York, United Kingdom, p 12

Khaledi K, Mahmoudi E, Datcheva M, et al (2016a) Sensitivity analysis and parameter identification of a time dependent constitutive model for rock salt. Journal of Computational and Applied Mathematics 293:128–138. doi: 10.1016/j.cam.2015.03.049

Khaledi K, Mahmoudi E, Datcheva M, Schanz T (2016b) Analysis of compressed air storage caverns in rock salt considering thermo-mechanical cyclic loading. Environmental Earth Sciences 75:1149. doi: 10.1007/s12665-016-5970-1

Kim YM, Lee JH, Kim SJ, Favrat D (2012) Potential and evolution of compressed air energy storage: Energy and exergy analyses. Entropy 14:1501–1521. doi: 10.3390/e14081501

Kim YM, Shin DG, Favrat D (2011) Operating characteristics of constant-pressure compressed air energy storage (CAES) system combined with pumped hydro storage based on energy and exergy analysis. Energy 36:6220–6233. doi: 10.1016/j.energy.2011.07.040

Klaus T, Vollmer C, Werner K, et al (2010) Energy target 2050: 100% renewable electricity supply. Umweltbundesamt, Dessau-Roßlau, Germany

Klein E, De Lucia M, Kempka T, Kühn M (2013) Evaluation of long-term mineral trapping at the Ketzin pilot site for CO_2 storage: An integrative approach using geochemical modelling and reservoir simulation. International Journal of Greenhouse Gas Control 19:720–730. doi: 10.1016/j.ijggc.2013.05.014

Klimchouk A (1996) The dissolution and conversion of gypsum and anhydrite. International Journal of Speleology 25:21–36. doi: 10.5038/1827-806X.25.3.2

Köhn D, De Nil D, al Hagrey SA, Rabbel W (2016) A combination of waveform inversion and reverse-time modelling for microseismic event characterization in complex salt structures. Environmental Earth Sciences 75:1235. doi: 10.1007/s12665-016-6032-4

Kolditz O, Bauer S (2004) A process-oriented approach to computing multi-field problems in porous media. Journal of Hydroinformatics 6:225–244.

Kolditz O, Bauer S, Bilke L, et al (2012) OpenGeoSys: an open-source initiative for numerical simulation of thermo-hydro-mechanical/chemical (THM/C) processes in porous media. Environmental Earth Sciences 67:589–599. doi: 10.1007/s12665-012-1546-x

Kushnir R, Dayan A, Ullmann A (2012a) Temperature and pressure variations within compressed air energy storage caverns. International Journal of Heat and Mass Transfer 55:5616–5630. doi: 10.1016/j.ijheatmasstransfer.2012.05.055

Kushnir R, Ullmann A, Dayan A (2010) Compressed air flow within aquifer reservoirs of CAES plants. Transport in Porous Media 81:219–240. doi: 10.1007/s11242-009-9397-y

Kushnir R, Ullmann A, Dayan A (2012b) Thermodynamic and hydrodynamic response of compressed air energy storage reservoirs: a review. Reviews in Chemical Engineering 28:123–148. doi: 10.1515/revce-2012-0006

Lasaga AC (1998) Kinetic Theory In the Earth Sciences. Princeton University Press, Princeton

LBEG (2015) Untertage-Gasspeicherung in Deutschland. Erdöl Erdgas Kohle 131(11) 398–406.

Leetaru HE, Frailey SM, Damico J, et al (2009) Understanding CO_2 plume behavior and basin-scale pressure changes during sequestration projects through the use of reservoir fluid modeling. Energy Procedia 1:1799–1806.

Lemmon EW, Jacobsen RT, Penoncello SG, Firend DG (2000) Thermodynamic properties of air and mixtures of nitrogen, argon, and oxygen from 60 to 2000 K at pressures to 2000 MPa. Journal of Physical and Chemical Reference Data 29:331–385.

Li D, Bauer S, Benisch K, et al (2014) OpenGeoSys-ChemApp: A coupled simulator for reactive transport in multiphase systems and application to CO_2 storage formation in Northern Germany. Acta Geotechnica 9:67–79. doi: 10.1007/s11440-013-0234-7

Li D, Beyer C, Bauer S (2018) A unified phase equilibrium model for hydrogen solubility and solution density. International Journal of Hydrogen Energy 43:512–529. doi: 10.1016/j.ijhydene.2017.07.228

Lowson RT (1982) Aqueous Oxidation of Pyrite by Molecular Oxygen. Chemical Reviews 82:461–497. doi: 10.1021/cr00051a001

Lu J, Mickler PJ, Nicot J-P, et al (2014) Geochemical impact of oxygen on siliciclastic carbon storage reservoirs. International Journal of Greenhouse Gas Control 21:214–231. doi: 10.1016/j.ijggc.2013.12.017

Luo X, Wang J, Dooner M, et al (2014) Overview of current development in compressed air energy storage technology. Energy Procedia 62:603–611. doi: 10.1016/j.egypro.2014.12.423

Luo X, Wang J, Krupke C, et al (2016) Modelling study, efficiency analysis and optimisation of large-scale Adiabatic Compressed Air Energy Storage systems with low-temperature thermal storage. Applied Energy 162:589–600. doi: 10.1016/j.apenergy.2015.10.091

MELUR (Ministerium für Energiewende, Landwirtschaft, Umwelt und ländliche Räume Schleswig-Holstein) S-HNA (2015) Abregelung von Strom aus Erneuerbaren Energien und daraus resultierende Entschädigungsansprüche in den Jahren 2010 bis 2014. MELUR, Kiel

Miles B, Kalbacher T, Kolditz O, et al (2007) Development and parameterisation of a complex hydrogeological model based on high-resolution direct-push data. Environmental Geology 52:1399–1412. doi: 10.1007/s00254-006-0582-9

Mitiku AB, Bauer S (2013) Optimal use of a dome-shaped anticline structure for CO_2 storage: a case study in the North German sedimentary basin. Environmental Earth Sciences 70:3661–3673. doi: 10.1007/s12665-013-2580-z

Mitiku AB, Li D, Bauer S, Beyer C (2013) Geochemical modelling of CO_2–water–rock interactions in a potential storage formation of the North German sedimentary basin. Applied Geochemistry 36:168–186. doi: 10.1016/j.apgeochem.2013.06.008

Molz FJ, Melville JG, Parr AD, et al (1983) Aquifer thermal energy storage : A well doublet experiment at increased temperatures. Water Resources Research 19:149–160. doi: 10.1029/WR019i001p00149

Moog HC, Hagemann S (2004) Thermodynamische Modellierung hochsalinarer Lösungen: Gewinnung von Daten für Fe(II), Fe(III) und S(-II) und Entwick - lung eines Programms zur Modellierung des reaktiven Stofftransports im Nahfeld eines Endlagers. Gesellschaft für Anlagen- und Reaktorsicherheit (GRS) mbH

Morris C, Pehnt M (2016) The German Energiewende Book. Berlin, Germany

Morris C, Pehnt M (2012) Energy Transition: The German Energiewende. Berlin, Germany

Mottaghy D, Pechnig R, Taugs R, et al (2010) Erstellung eines geothermischen Modells für Teile Hamburgs und anliegende Gebiete. BBR Jahresmagazin 52–59.

Nakhamkin M, Schainker RB, Chiruvolu M, et al (2009) Second Generation of CAES Technology - Performance, Operations, Economics, Renewable Load Management, Green Energy.

Nazary Moghadam S, Mirzabozorg H, Noorzad A (2013) Modeling time-dependent behavior of gas caverns in rock salt considering creep, dilatancy and failure. Tunnelling and Underground Space Technology 33:171–185. doi: 10.1016/j.tust.2012.10.001

Neave JW (2007) Analysis and characterization of fault networks. Google Patents

Ni XD, Chen K (2014) Study on the Conversion of GOCAD Models to FLAC3D Models. Applied Mechanics and Materials 501–504:2527–2531. doi: 10.4028/www.scientific.net/AMM.501-504.2527

Nordstrom DK (1982) Aqueous Pyrite Oxidation and the Consequent Formation of Secondary Iron Minerals. In: Acid Sulfate Weathering. Soil Science Society of America, Madison, WI, pp 37–56

Nordstrom DK, Blowes DW, Ptacek CJ (2015) Hydrogeochemistry and microbiology of mine drainage: An update. Applied Geochemistry 57:3–16. doi: 10.1016/j.apgeochem.2015.02.008

Oldenburg CM, Pan L (2013a) Porous Media Compressed-Air Energy Storage (PM-CAES): Theory and Simulation of the Coupled Wellbore-Reservoir System. Transport in Porous Media 97:201–221. doi: 10.1007/s11242-012-0118-6

Oldenburg CM, Pan L (2013b) Utilization of CO_2 as cushion gas for porous media compressed air energy storage. Greenhouse Gases: Science and Technology 3:124–135. doi: 10.1002/ghg.1332

Oldenburg CM, Pruess K (1999) Plume separation by transient thermohaline convection in porous media. Geophysical Research Letters 26:2997–3000. doi: 10.1029/1999GL002360

Oldenburg CM, Rinaldi AP (2011) Buoyancy effects on upward brine displacement caused by CO_2 injection. Transport in porous media 87:525–

540.

Palandri JL, Kharaka YK (2004) A compilation of rate parameters of water-mineral interaction kinetics for application to geochemical modeling. USGS Open File Report 2004–1068:71. doi: 10.1098/rspb.2004.2754

Pan L, Oldenburg CM, Pruess K, Wu Y-S (2011) Transient CO_2 leakage and injection in wellbore-reservoir systems for geologic carbon sequestration. Greenhouse Gases: Science and Technology 1:335--350. doi: 10.1002/ghg

Paradigm (2016) Paradigm GOCAD. http://www.pdgm.com/products/gocad/. Accessed 22 Feb 2016

Park CH, Shinn YJ, Park YC, et al (2014) PET2OGS: Algorithms to link the static model of Petrel with the dynamic model of OpenGeoSys. Computers and Geosciences 62:95–102. doi: 10.1016/j.cageo.2013.09.014

Parkhurst DL, Appelo CAJ (2013) Description of input and examples for PHREEQC version 3--A computer program for speciation, batch-reaction, one-dimensional transport, and inverse geochemical calculations. book 6:497.

Pearce JK, Dawson GKW, Law ACK, et al (2016a) Reactivity of micas and cap-rock in wet supercritical CO_2 with SO_2 and O_2 at CO_2 storage conditions. Applied Geochemistry 72:59–76. doi: 10.1016/j.apgeochem.2016.06.010

Pearce JK, Golab A, Dawson GKW, et al (2016b) Mineralogical controls on porosity and water chemistry during O_2-SO_2-CO_2 reaction of CO_2 storage reservoir and cap-rock core. Applied Geochemistry 75:152–168. doi: 10.1016/j.apgeochem.2016.11.002

Pei P, Korom SF, Ling K, et al (2015) Thermodynamic impact of aquifer permeability on the performance of a compressed air energy storage plant. Energy Conversion and Management 97:340–350. doi: 10.1016/j.enconman.2015.03.072

Peng D-Y, Robinson DB (1976) A New Two-Constant Equation of State. Industrial & Engineering Chemistry Fundamentals 15:59–64. doi: 10.1021/i160057a011

Pérez-López R, Cama J, Miguel Nieto J, et al (2009) Attenuation of pyrite oxidation with a fly ash pre-barrier: Reactive transport modelling of column experiments. Applied Geochemistry 24:1712–1723. doi: 10.1016/j.apgeochem.2009.05.001

Petersen S, Hack K (2007) The thermochemistry library ChemApp and its applications. International Journal of Materials Research 98:935–945. doi: 10.3139/146.101551

Pfeiffer WT, al Hagrey SA, Köhn D, et al (2016a) Porous media hydrogen storage at a synthetic, heterogeneous field site: numerical simulation of storage operation and geophysical monitoring. Environmental Earth Sciences 75:1177. doi: 10.1007/s12665-016-5958-x

Pfeiffer WT, Bauer S (2015) Subsurface Porous Media Hydrogen Storage – Scenario Development and Simulation. Energy Procedia 76:565–572. doi: 10.1016/j.egypro.2015.07.872

Pfeiffer WT, Beyer C, Bauer S (2017) Hydrogen storage in a heterogeneous sandstone formation: dimensioning and induced hydraulic effects. Petroleum Geoscience petgeo2016-050. doi: 10.1144/petgeo2016-050

Pfeiffer WT, Graupner B, Bauer S (2016b) The coupled non-isothermal, multiphase-multicomponent flow and reactive transport simulator OpenGeoSys–ECLIPSE for porous media gas storage. Environmental Earth Sciences 75:1347. doi: 10.1007/s12665-016-6168-2

Pitzer KS (1973) Thermodynamics of electrolytes. I. Theoretical basis and general equations. The Journal of Physical Chemistry 77:268–277. doi: 10.1021/j100621a026

Ponting DK (1992) Corner Point Geometry in Reservoir Simulation. The Mathematics of Oil Recovery, Institute of Mathematics and its Applications, 45–65. doi: 10.3997/2214-4609.201411305

Popp S, Beyer C, Dahmke A, et al (2016) Temperature-dependent dissolution of residual non-aqueous phase liquids: model development and verification. Environmental Earth Sciences 75:953. doi: 10.1007/s12665-016-5743-x

Pruess K (1991) TOUGH2: A general-purpose numerical simulator for multiphase fluid and heat flow. United States

Raju M, Khaitan SK (2012) Modeling and simulation of compressed air storage in caverns: A case study of the Huntorf plant. Applied Energy 89:474–481. doi: 10.1016/j.apenergy.2011.08.019

Reinhold K, Müller C, Riesenberg C (2011) Informationssystem Speichergesteine für den Standort Deutschland - Synthese -. Berlin/Hannover, Bundesanstalt für Geowissenschaften und Rohstoffe (BGR)

Reitenbach V, Ganzer L, Albrecht D, Hagemann B (2015) Influence of added hydrogen on underground gas storage: a review of key issues. Environmental Earth Sciences 6927–6937. doi: 10.1007/s12665-015-4176-2

Rutqvist J (2012) The Geomechanics of CO_2 Storage in Deep Sedimentary Formations. Geotechnical and Geological Engineering 30:525–551. doi: 10.1007/s10706-011-9491-0

RWE Power (2010) Adele–Adiabatic Compressed-Air Energy Storage for Electricity Supply.

http://www.rwe.com/web/cms/mediablob/en/391748/data/364260/1/rwe-power-ag/innovations/Brochure-ADELE.pdf.

Sa H, Kohn D, Ce W, et al (2014) Feasibility Study for Geophysical Monitoring Renewable Gas Energy Compressed in Pore Storages. Journal of Geology & Geosciences. doi: 10.4172/2329-6755.1000169

Scheer W (2001) Untersuchungsprogramm zur Ermittlung des nutzbaren Grundwasserdargebotes im schleswig-holsteinischen Nachbarraum zu Hamburg, Südost-Holstein.Abschlußbericht.Landesamt für Natur und Umwelt des Landes Schleswig-Holstein. Flintbek. 52 S.

Scheer W, Kröger J, Reinhard K (2007) Geologische 3-D-Modellierung des Untergrundes – Ergebnisse aus dem INTERREG IIIB-Projekt BurVal. Jahresbericht LANU, Schleswig-Holstein, Flintbek

Schlumberger (2014) Petrel E&P Software Platform version 2014.6.

Schlumberger (2016) Eclipse reservoir simulation software v2016.1 – Technical Description Manual. Schlumberger Ltd

Schlumberger (2013) Petrel Structual Modeling - Training and Exercise Guide. Sclumberger

Schulte RH, Critelli N, Holst K, Huff G (2012) Lessons from Iowa: development of a 270 megawatt compressed air energy storage project in Midwest independent system operator. Albuquerque, New Mexico and Livermore, California

Shiers DW, Blight KR, Ralph DE (2005) Sodium sulphate and sodium chloride effects on batch culture of iron oxidising bacteria. Hydrometallurgy 80:75–82. doi: 10.1016/j.hydromet.2005.07.001

Singer PC, Stumm W (1970) Acidic Mine Drainage: The Rate-Determining Step. Science 167:1121–1123. doi: 10.1126/science.167.3921.1121

Sorknæs P, Mæng H, Weiss T, Andersen AN (2013) stoRE Project - Facilitating energy storage to allow high penetration of intermittent renewable energy: Overview of current status and future development scenarios of the electricity system in Denmark – allowing integration of large quantities of wind pow.

Souche L, Lepage F, Iskenova G (2013) Volume Based Modeling - Automated Construction of Complex Structural Models. 75th EAGE Conference & Exhibition incorporating SPE EUROPEC 2013 London, UK, 10-13 June 2013 10–13. doi: 10.3997/2214-4609.20130037

Spaar H (2016) Modellierung von geochemischen Prozessen in Folge einer H_2-Speicherung. Master Thesis. University of Kiel

Sternberg A, Bardow A (2015) Power-to-What? ? Environmental assessment of energy storage systems. Energy Environ Sci 8:389–400. doi: 10.1039/C4EE03051F

Sterner M, Stadler I (2014) Energiespeicher - Bedarf, Technologien, Integration. Springer Berlin Heidelberg, Berlin, Heidelberg

Stober I, Bucher K (2012) Geothermie. Springer Verlag, Berlin Heidelberg

Stocker T (2014) Climate change 2013: the physical science basis: Working Group I contribution to the Fifth assessment report of the Intergovernmental Panel on Climate Change. Cambridge University Press

Succar S, Williams R (2008) Compressed Air Energy Storage : Theory , Resources , And Applications For Wind Power. Princeton University, Energy Analysis Group

Suchi E, Dittmann J, Knopf S, et al (2014) Geothermie-Atlas zur Darstellung möglicher Nutzungskonkurrenzen zwischen CCS und Tiefer Geothermie in Deutschland. Zeitschrift der Deutschen Gesellschaft für Geowissenschaften 165:439–453. doi: 10.1127/1860-1804/2014/0070

Taylor P, Evangelou VPB, Zhang YL (2009) Critical Reviews in Environmental Science and Technology A review : Pyrite oxidation mechanisms and acid mine drainage prevention A Review : Pyrite Oxidation Mechanisms and Acid Mine Drainage Prevention. Critical Reviews in Environmental Science and Technology 37–41.

Tek MR (2012) Underground storage of natural gas: theory and practice. Springer Science & Business Media

The HYDROdynamics Group LCC (2005) Iowa Stored Energy Plant Agency Compressed-Air Energy Storage Project : COMPRESSED-AIR ENERGY STORAGE HIGH LEVEL RESERVOIR SCREENING EVALUATION IN IOWA prepared for : Electricity and Air Storage Enterprises Houston, Texas.

The HYDROdynamics Group LCC (2011) Iowa Stored Energy Plant Agency Compressed-Air Energy Storage Project : FINAL PROJECT REPORT- DALLAS CENTER MT . SIMON STRUCTURE CAES SYSTEM PERFORMANCE ANALYSIS prepared for : Iowa Storage Energy Plant Agency.

Vogt C, Iwanowski-Strahser K, Marquart G, et al (2013) Modeling contribution to risk assessment of thermal production power for geothermal reservoirs. Renewable Energy 53:230–241. doi: 10.1016/j.renene.2012.11.026

Wang W, Kosakowski G, Kolditz O (2009) A parallel finite element scheme for thermo-hydro-mechanical (THM) coupled problems in porous media. Computers and Geosciences 35:1631–1641. doi:

10.1016/j.cageo.2008.07.007

Watanabe N, Wang W, McDermott CI, et al (2009) Uncertainty analysis of thermo-hydro-mechanical coupled processes in heterogeneous porous media. Computational Mechanics 45:263–280. doi: 10.1007/s00466-009-0445-9

Weber R, Beck H-P, Krüge U (2018) Huntorf2020. https://www.ievb.tu-clausthal.de/en/research/research-projects/huntorf2020/. Accessed 4 Oct 2018

Wei N, Li X, Wang Y, et al (2015) Geochemical impact of aquifer storage for impure CO_2 containing O_2 and N_2: Tongliao field experiment. Applied Energy 145:198–210. doi: 10.1016/j.apenergy.2015.01.017

Weiß T, Schulz D (2013) Germany Overview of the electricity supply system and an estimation of future energy storage needs. 1–63.

White AF, Peterson ML (1990) Chemical Modeling of Aqueous Systems II. American Chemical Society, Washington, DC

Wiles LE, Mccann RA (1981) Water Coning in Porous Media Reservoirs for Compressed Air Energy Storage. Richland, Washington

Williamson MA, Rimstidt JD (1994) The kinetics and electrochemical rate-determining step of aqueous pyrite oxidation. Geochimica et Cosmochimica Acta 58:5443–5454. doi: 10.1016/0016-7037(94)90241-0

Xie M, Bauer S, Kolditz O, et al (2006) Numerical simulation of reactive processes in an experiment with partially saturated bentonite. Journal of Contaminant Hydrology 83:122–147. doi: https://doi.org/10.1016/j.jconhyd.2005.11.003

Xu T, Kharaka YK, Doughty C, et al (2010) Reactive transport modeling to study changes in water chemistry induced by CO_2 injection at the Frio-I Brine Pilot. Chemical Geology 271:153–164. doi: 10.1016/j.chemgeo.2010.01.006

Yaws CL, Gomes J. (2009) Transport Properties of Chemicals and Hydrocarbons. William Andrew, New York

Zabetakis MG (1964) Flammability characteristics of combustible gases and vapors. doi: 10.2172/7328370

Zehner B, Börner JH, Görz I, Spitzer K (2015) Workflows for generating tetrahedral meshes for finite element simulations on complex geological structures. Computers & Geosciences 79:105–117. doi: 10.1016/j.cageo.2015.02.009

Zerai B, Saylor BZ, Matisoff G (2006) Computer simulation of CO_2 trapped through mineral precipitation in the Rose Run Sandstone, Ohio. Applied Geochemistry 21:223–240. doi: 10.1016/j.apgeochem.2005.11.002

Zhang W, Li Y, Xu T, et al (2009) Long-term variations of CO_2 trapped in different mechanisms in deep saline formations: A case study of the Songliao Basin, China. International Journal of Greenhouse Gas Control 3:161–180. doi: 10.1016/j.ijggc.2008.07.007

Zhou Q, Birkholzer JT (2011) On scale and magnitude of pressure build-up induced by large-scale geologic storage of CO_2. Greenhouse Gases: Science and Technology 1:11–20.

Zolotov MY, Shock EL (2005) Formation of jarosite-bearing deposits through aqueous oxidation of pyrite at Meridiani Planum, Mars. Geophysical Research Letters 32:1–5. doi: 10.1029/2005GL024253